UNIVERSITÀ
DEGLI STUDI
DI BRESCIA

DOTTORATO DI RICERCA IN INGEGNERIA MECCANICA E INDUSTRIALE (DRIMI)

Settore scientifico disciplinare (SSD): ING-IND/16 – ING/IND/21

CICLO XXXVI

Production process optimization and characterization of 3D printed metal products

dottorando
Francesco Cantaboni

Supervisori
Dott.ssa Paola Serena Ginestra
Dott.ssa Marialaura Tocci

Index

Abstract

Additive Manufacturing (AM) technology allows the production of complex geometries such as lattice and foam structures, finding diverse applications in the automotive, biomedical, and aerospace industries. Metal Additive Manufacturing (MAM) is a technology capable of producing metallic components layer by layer. One of the most used technologies is Powder Bed Fusion (PBF), where metal powder is melted using a source of energy, either Laser or Electron Beam. It can be further classified into Laser Powder Bed Fusion (L-PBF) and Electron Beam Powder Bed Fusion (EB-PBF). The alloys processed and studied in the literature through AM are still somewhat limited. The most commonly used alloys are stainless steel and ferrous alloys, titanium alloys, nickel-based alloys, aluminum alloys, and cobalt alloys.

Lattice structures produced through AM were extensively explored in the literature due to their beneficial characteristics. The manufacturing process introduces defects typically categorized as geometry and dimension, surface quality, and porosity defects. As these defects significantly impact the behavior of lattice structures, the manufactured components may not exhibit the expected properties.

The focus of this doctoral research thesis is to fill the gaps in the literature concerning the effective mechanical behavior and the design of lattice structures manufactured with L-PBF and EB-PBF technologies, utilizing Co-Cr-Mo alloy, Ti-6Al-4V alloy, and 17-4 PH SS metal powders. Specifically, the main objective was centered on the production and characterization of metallic lattice structures with varying unit cell orientations, building angles, and connections with the solid part.

The present thesis is organized as follows. In the first Chapter, a brief introduction illustrates the main PBF processes, with particular attention to PBF processes. Microstructural features typical of products obtained with these technologies are discussed, together with the typical defects. The most used alloys to produce complex structures, such as lattice or metallic foam are presented. Finally, a FEM analysis of the process and the mechanical behavior of the products are introduced.

This discussion of experimental activities and results is divided into three main experimental parts, based on the metallic alloy used.

Therefore, the second Chapter is dedicated to the study of Co-Cr-Mo lattice structures. The L-PBF technique was employed to manufacture lattice structures with defined building angles relative to the build platform, using a biocompatible Co-Cr-Mo alloy. Three different types of elementary cell geometries were selected: Face Centered Cubic, Diagonal, and Diamond. These cells were applied to radially oriented lattice structures to assess the influence of their orientation in relation to the sample and the build platform.

A separated Chapter covers the activities regarding the Ti-6Al-4V lattice. The L-PBF technique was also adopted evaluating and optimizing the single contour strategy for the production of Ti-6Al-4V lattices. The optimal process parameters were identified for producing a spinal cage as a case study. Additionally, Ti-6Al-4V lattices with Body Centered Cubic unit cell with and without an external solid shell were designed and produced with EB-PBF to investigate the mechanical behavior and metallurgical features, especially at the interface between

the solid and lattice parts. The study of the role of the shell under compression load, and the identification of potential critical issues due to the connection with the lattice part were the innovative focal point of this chapter. Finally, in Chapter 4, the discussion is focused on 17-4PH stainless steel lattice structures. L-PBF was also employed to manufacture 17-4 PH stainless steel square-based lattice structures with a solid shell. The Face Centered Cubic unit cell was chosen as the lattice cell geometry. The primary aim of this work was to study the role of the shell in the mechanical behavior under compression load and to identify any critical issues due to the connection of the shell with the lattice part. This is a crucial aspect as lattice structures are often integrated with solid walls, and studying their relative behavior can enhance the understanding of the performance of complex components. Lattices without the solid shell were produced and studied to understand the role of the solid part. For each alloy studied, the mechanical and microstructural characterizations were conducted. Compression tests were performed on the lattices to understand the influence of cell orientation, building angle, and the influence of the connection with the solid part. Microhardness measurements were taken, and the fracture mechanisms of these structures were analyzed. Moreover, heat treatment was carried out, in particular on 17-4 PH SS lattice, to study its influence on microstructural and mechanical properties.

In conclusion, this thesis was dedicated to the production and characterization of innovative metallic lattice structures using L-PBF and EB-PBF. Each studied alloy exhibited different features, issues, and applications.

Sommario

La tecnologia di Additive Manufacturing (AM) consente la produzione di geometrie complesse come strutture lattice e schiume metalliche, trovando diverse applicazioni nei settori automobilistico, biomedicale e aerospaziale. Il Metal Additive Manufacturing (MAM) è una tecnologia in grado di produrre componenti metallici strato dopo strato. Una delle tecnologie più utilizzate è la Powder Bed Fusion (PBF), in cui la polvere metallica viene fusa utilizzando una sorgente di energia, laser o fascio di elettroni. Può essere ulteriormente classificata in Laser Powder Bed Fusion (L-PBF) e Electron Beam Powder Bed Fusion (EB-PBF). Le leghe processate e studiate nella letteratura attraverso l'AM sono ancora in qualche modo limitate. Le leghe più comunemente utilizzate sono l'acciaio inossidabile, le leghe ferrose, le leghe di titanio, le leghe a base di nichel, le leghe di alluminio e le leghe di cobalto.

Le strutture lattice prodotte attraverso l'AM sono state ampiamente esplorate nella letteratura a causa delle loro caratteristiche vantaggiose. Il processo di produzione introduce difetti generalmente categorizzati come difetti di geometria e dimensione, qualità della superficie e difetti di porosità. Poiché questi difetti influenzano significativamente il comportamento delle strutture lattice, i componenti prodotti potrebbero non mostrare le proprietà attese.

L'obiettivo di questa tesi di ricerca di dottorato, è colmare le lacune nella letteratura riguardanti il comportamento meccanico efficace e il design di strutture lattice prodotte con le tecnologie L-PBF ed EB-PBF, utilizzando polveri metalliche di lega Co-Cr-Mo, lega Ti-6Al-4V e acciaio inossidabile 17-4 PH. In particolare, l'obiettivo principale era centrato sulla produzione e caratterizzazione di strutture lattice metalliche con orientamenti variabili delle celle, angoli di costruzione differenti e connessioni con una parte solida.

La tesi è organizzata come segue. Nel primo capitolo, viene fornita una breve introduzione illustrando i principali processi PBF, con particolare attenzione ai processi stessi. Sono discusse le caratteristiche microstrutturali tipiche dei prodotti ottenuti con queste tecnologie, insieme ai difetti tipici. Vengono presentate le leghe più utilizzate per produrre strutture complesse, come lattice o schiume metalliche. Infine, viene introdotta un'analisi FEM del processo e del comportamento meccanico dei prodotti.

La discussione sulle attività sperimentali e sui risultati è divisa in tre parti sperimentali principali, basate sulla lega metallica utilizzata.

Pertanto, il secondo capitolo è dedicato allo studio delle strutture lattice in Co-Cr-Mo. La tecnica L-PBF è stata utilizzata per produrre strutture lattice con angoli di costruzione definiti rispetto al piatto di stampa, utilizzando una lega biocompatibile Co-Cr-Mo. Sono stati selezionati tre tipi di geometrie di celle elementari: Cubica a Facce Centrate, Diagonale e Diamante. Queste celle sono state applicate a strutture lattice orientate radialmente per valutare l'influenza del loro orientamento rispetto al campione e al piatto di stampa.

Un capitolo separato copre le attività riguardanti le strutture lattice in Ti-6Al-4V. La tecnica L-PBF è stata adottata anche per valutare e ottimizzare la strategia di scansione per la produzione di lattice in Ti-6Al-4V. Sono

stati identificati i parametri di processo ottimali per la produzione di una gabbia spinale come caso studio. Inoltre, sono stati progettati e prodotti lattice in Ti-6Al-4V con una cella Cubica a Corpo Centrato, con e senza un guscio solido esterno, utilizzando EB-PBF per investigare il comportamento meccanico e le caratteristiche metallurgiche, specialmente all'interfaccia tra la parte solida e la struttura lattice. Lo studio del ruolo del guscio sotto carico di compressione e l'identificazione di eventuali problemi critici dovuti alla connessione solido-lattice sono stati i punti focali e innovativi di questo capitolo.

Infine, nel capitolo 4, la discussione è incentrata sulle strutture lattice in acciaio inossidabile 17-4PH. La tecnica L-PBF è stata impiegata per produrre strutture lattice a base quadrata in acciaio inossidabile 17-4 PH con un guscio solido. La cella Cubica a Facce Centrate è stata scelta e applicata alla struttura lattice. L'obiettivo principale di questo lavoro era studiare il ruolo del guscio nel comportamento meccanico sotto carico di compressione e identificare eventuali problemi critici dovuti alla connessione del guscio con la struttura lattice. Questo è un aspetto cruciale poiché le strutture lattice sono spesso integrate con pareti solide, e lo studio del loro comportamento relativo può migliorare la comprensione delle prestazioni di componenti complessi. Strutture lattice senza guscio solido sono state prodotte e studiate per comprendere meglio il ruolo della parte solida.

Per ciascuna lega studiata, sono state condotte caratterizzazioni meccaniche e microstrutturali. Sono stati eseguiti test di compressione sulle strutture lattice per comprendere l'influenza dell'orientamento delle celle, dell'angolo di costruzione e della connessione con la parte solida. Sono state effettuate misurazioni di micro-durezza e sono stati analizzati i meccanismi di rottura di queste strutture. Inoltre, è stato effettuato un trattamento termico, in particolare sulle strutture lattice in 17-4 PH SS, per studiare la sua influenza sulle proprietà microstrutturali e meccaniche.

In conclusione, questa tesi è stata dedicata alla produzione e caratterizzazione di innovative strutture lattice metalliche, utilizzando le tecnologie L-PBF ed EB-PBF. Ogni lega studiata ha mostrato caratteristiche, problematiche e applicazioni differenti.

Chapter 1

In the first chapter, an introduction to Powder Bed Fusion (PBF) technology is provided. PBF enables the processing of metallic alloys to produce intricate metallic components. The initial section discusses the distinctions between the Laser and Electron beam as energy sources in PBF-based technology. Following this, commonly utilized metal alloys and lattice structures are outlined. The typical microstructural features and defects of components manufactured with these technologies were discussed. Finally, the Finite Element Model (FEM) is examined, with a focus on their application to the PBF process and to the study of mechanical behavior of the produced components.

Introduction

1.1 Additive Manufacturing: Powder Bed Fusion

Additive manufacturing (AM), commonly known as 3D printing, is a well-established technology with the capability to produce porous structures and complex geometries layer-by-layer using various materials. In contrast to traditional subtractive methods, AM is based on the principle of material addition, as defined by the ASTM (American Society for Testing and Materials International) 52900 standard.

Starting with a CAD model, it becomes possible to fabricate objects with complex shapes, providing to the specific requirements of industries such as automotive, biomedical, and aerospace. The additive manufacturing process is also referred to as additive layer manufacturing, layer manufacturing, and freeform fabrication [1]. AM technology encompasses various production processes, primarily applied to plastic and metallic materials. Several additive manufacturing (AM) methods are detailed in ISO/ASTM 52900. Metal AM (MAM) methods have been widely explained in the literature, and they generally share significant similarities [2]. The material, introduced into the machine as wire or powder, undergoes processing through a laser, electron beam, or arc wire as the energy source. Metal AM can be classified into three main groups: Powder Bed System (PBF), Directed Energy Deposition (DED) and wire arc additive manufacturing (WAAM) [3]. Due to different deposition principles and technical parameters, each of these three technologies has its own metallurgical characteristics, advantages, and scope of applications [4].

The PBF technique is a manufacturing method where the laser or electron beam scans the powder already spread on the plate, locally melting it in an inert or vacuum environment (see Figure 1). Rapid solidification occurs immediately afterward. After completing a layer, the building plate piston descends, and the powder chamber piston ascends by a defined height, corresponding to the layer thickness. Another layer of powder is spread on the building chamber by a roller, which is then melted and solidified. This layer-by-layer process continues until the job is complete. PBF-based processes require supports where needed to prevent distortions and collapse of molten materials due to overhanging surfaces. These supports can be generated during the 3D part design phase but require mechanical removal. Additionally, post-processing treatments such as polishing, machining, or heat treatment are necessary to enhance the features of the samples based on the required characteristics. In some cases, Hot Isostatic Pressing (HIP) treatment is also necessary to ensure part density [5].

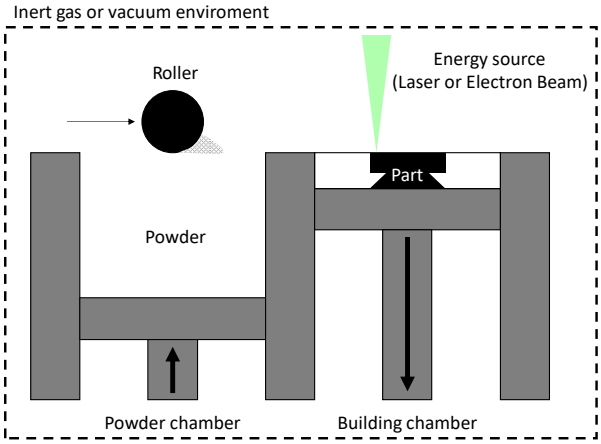

Figure 1. Powder Bed Fusion process.

Based on the applied energy source, PBF-based technology is divided into Laser Powder Bed Fusion (L-PBF) and Electron Beam Powder Bed Fusion (EB-PBF) technologies.

1.2 Laser - Powder Bed Fusion

L-PBF is one of the most common Additive Manufacturing (AM) processes, known for its capability to manufacture complex metallic parts, thereby reducing costs, time, and labor. Developed by Fockele and Schwarze in collaboration with the Fraunhofer Institute in 1999 [6], the L-PBF system (shown in Figure 2) typically includes a chamber containing virgin or recycled metal powder (1), a building plate where the powder is spread to create a powder bed until the finished part is produced (2), a roller or scraper (3) to deliver and

spread the metal powder, and a laser source to melt the powder (4). The system operates automatically to deliver and maintain a uniform powder bed throughout the process.

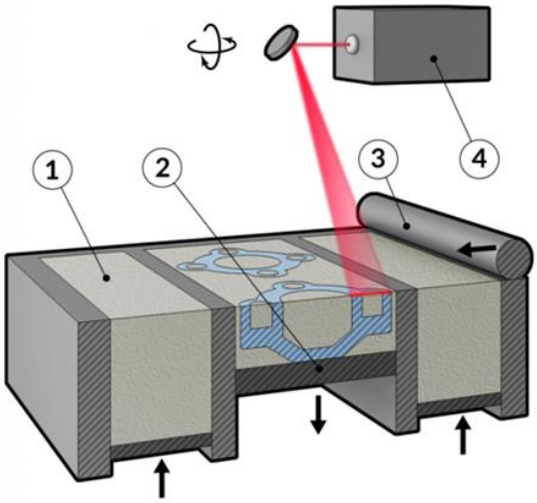

Figure 2. Laser Powder Bed Fusion process [7].

Specifically, the laser is monitored and focused by a beam deflection system comprising Galvano mirrors and a flat field focusing lens. In general, the .STL file is generated from a 3D CAD part and input into the machine. The powder bed is spread on the building plate by the roller with a specific layer thickness, and the laser scans the powder bed, locally melting the powder alloy, followed by rapid solidification. After solidification, another layer is spread over the previously processed layer. These spreading and scanning steps are repeated until the completion of the final part. The building process occurs in a protective atmosphere, of Nitrogen or Argon gas, to prevent oxidation of the part.

Several process parameters can influence the results of the final part manufactured with L-PBF technology. The most commonly considered parameters include laser power, scanning speed, hatch distance (distance between successive laser passes), and layer thickness [8]. During the melting phase, overlapped melt pools are generated, which are typical for this process and take on a semi-circular shape due to the heat energy of the laser [9].

In the L-PBF process, the laser interacts with the metallic powder, leading to various physical phenomena, such as solidification, reflection, chemical reactions, absorption, heat transfer, phase transformation, transportation of molten metal or the flow of molten metal within the molten pool and Marangoni effect which drives the molten liquid metal from the hotter laser spot to the cold rear [10]. The primary objective of the L-PBF method is to fabricate fully dense parts, although achieving this result can be challenging. Steep thermal gradients and non-uniform expansion/contraction of the material induced by rapid melting and solidification impact the microstructure and can result in the presence of defects and residual stresses on the metallic part. Defects such as porosity, lack of fusion, and partially or unmelted powder sticking to the surface can occur on the final parts [11–13].

1.3 Electron Beam - Powder Bed Fusion

Electron Beam Powder Bed Fusion (EB-PBF) is another PBF-based AM process in which an electron beam is employed to selectively melt the powder bed layer within a building chamber. The process is similar to L-PBF, with the main distinction of the use of an electron beam as the energy source for melting the powder bed, rather than a laser. In EB-PBF, a heated tungsten filament emits electrons at high speed, which are then controlled by two magnetic fields: the focus coil and the deflection coil. As illustrated in Figure 3, metallic parts are produced in a vacuum chamber (1) at elevated temperature in a range of 700°C - 1000°C, resulting in stress-relieved parts exhibiting material, mechanical, and chemical properties superior to those achieved through casting and forging. The process utilizes the energy from an electron beam (2) to melt metal powder (3). The powder is ejected from a powder hopper and spread on a building platform (4) using a rake (5), as discussed for the L-PBF process.

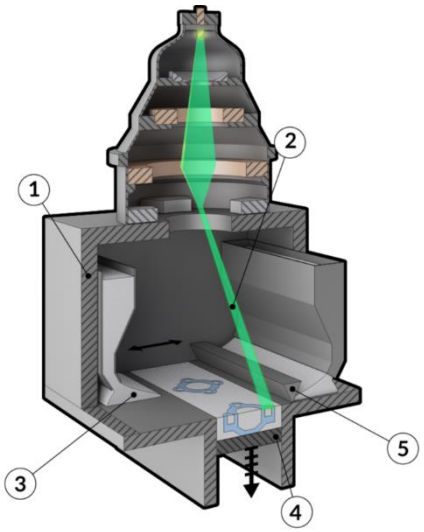

Figure 3. Electron Beam Powder Bed Fusion process [7].

To mitigate potential collisions between the fast-moving electrons and air molecules, the process occurs under vacuum or controlled vacuum conditions [14]. The kinetic energy generated is converted into thermal energy upon the high-speed electrons striking the powder bed, causing the powder to melt. Each layer is preheated by scanning it with an electron beam at high current and high scanning speed, followed by melting with low current and low scanning speed. Once the layer is completed, the building platform descends, and another powder layer is spread. This process is repeated until the metallic part is fully formed [15].

The differences between these two powder bed technologies have already been investigated. For instance, Gruber S. et al. [16] compared the geometrical accuracy within and between the PBF-based process. They found that the distinctions between L-PBF and EB-PBF were mainly attributed to the optimized parameters set, smaller powder particle size, laser beam spot diameter, and layer thickness. L-PBF excelled in representing inner structures, while EB-PBF showed sintered powder remnants in cooling channels. L-PBF had lower form deviations, but did not reach tolerance class "H," whereas EB-PBF values were mostly higher than tolerance class "L." Results for perpendicularity and position favored L-PBF, highlighting its overall advantage in

accuracy for dimensions, form, perpendicularity, and position tolerance. EB-PBF, currently, is deemed unsuitable for complex internal structures due to sintered powder issues.

1.4 Microstructural features

In PBF, the formation of grains is a crucial aspect of the microstructure, significantly influencing the mechanical properties and performance of 3D-printed metal parts. The melt pools are formed during the PBF process and acts as a fundamental unit in additive manufacturing. The cohesion of these overlapped melt pools, achieved through the partial remelting of adjacent tracks, forms a bond building the final 3D object.

PBF process is characterized by rapid melting followed by rapid solidification which influence the microstructure of 3D metal component. Rapid solidification results in a fine-grained microstructure, with grains smaller than those in conventionally processed materials. The high cooling rates contribute to the formation of grains with a more refined structure. Consequently, the primary microstructural feature in printed metallic materials is the formation of columnar grains through the epitaxial growth of crystals from the melt pool boundary. These columnar grains, originating in the initial solidification stage, serve as the primary solidification structure.

According to classical solidification theory, the primary grain microstructure is primarily governed by local solidification conditions within the melt pool for a given alloy. These conditions include factors such as temperature gradient and solidification rate. Solidification proceeds directionally from the previously deposited substrate to the molten liquid, dissipating heat to the solid substrate. As a result, grain growth phenomena predominantly determine the final microstructures [17].

As shown in Figure 4 the microstructural attributes of L-PBF are delineated by distinctive features, that can be highlighted at different levels: (i) at an intermediate level, a layered configuration in which each layer is composed of adjacent and partially overlapped melt pools, (ii) at a higher level, we can observe epitaxial columnar grains traversing more layers, and (iii) at smaller scale, cellular fine substructures within the melt pools. These features, that can be highlighted at different magnifications, make the L-PBF microstructure hierarchical. Solidified melt pools are usually observed by conventional light microscopy, while the other microstructural features often need advanced metallographic techniques [18]. The hierarchical microstructure of EB-PBF process present the same features [19].

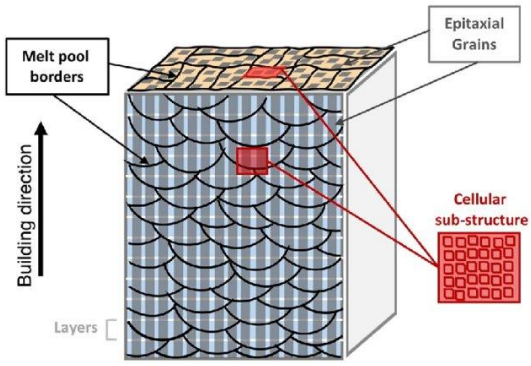

Figure 4. Schematic representation of the typical hierarchical L-PBF microstructure [18].

1.5 PBF process defects

In recent years, researchers have been examining the mechanisms responsible for the formation of defects in AM. Numerous publications have delved into different categories of defects in metal AM and provided explanations for the mechanisms driving their formation.

Metal powders often exhibit contaminations, largely due to moisture, presence of organic compounds, adsorbed gases, or formation of oxide and nitride films on the surface. This predisposition is primarily attributed to the high ratio of surface area to volume, which is much greater compared to bulk components produced through casting or forging. Contaminants not only have a negative impact on the mechanical properties and geometry of the consolidated component but also significantly reduce the wettability between the layer of molten metal and the underlying solidified layer. This wettability is a crucial characteristic for achieving a strong bond between the various layers and, consequently, optimal densification of the fused powders [74].

In general, the most commonly encountered defects are [75]:

Porosity: Porosity defects in L-PBF refer to the presence of voids or gas-filled pockets within the manufactured metal part (Figure 5). These defects can have implications for the structural integrity and mechanical properties of the final product. Several factors contribute to the formation of porosity defects in L-PBF:

- **Gas Entrapment:** During the melting and solidification process in L-PBF, gases may be released from the metal powder or other sources. If these gases are not able to escape, they can become trapped within the molten metal, leading to the formation of voids. The presence of trapped gases can be due to the turbulent motion on the melting pool surface. These gas pores are spherical and can persist in the as-fabricated parts, even after conventional heat treatment. Possible sources of gas that can be entrapped in the liquid metal are building atmosphere, humidity on surface of powder particles, evaporation of elements with low evaporation temperature, gas entrapped in the powder feedstock during the powder atomization process. In addition, when an excessive energy density is present in the melt pool, typically caused by high laser power and low scanning velocity, the resulting melt pool deepens, and a depression zone of vaporized material emerges, indicating the initiation of keyhole mode. Keyhole porosity arises due to the instability of the keyhole or the depression zone in the process. Excessive laser power can result in excessive heating, leading to the vaporization of the metal and the formation of gas bubbles. If these bubbles are trapped in the solidifying material, porosity can occur.

  Moreover, the presence of gases, such as oxygen or nitrogen, in the build chamber can lead to the entrapment of these gases into the molten metal, causing porosity defects.

- **Lack of Fusion:** In L-PBF, the laser selectively melts and fuses the metal powder to form each layer of the object. If there is insufficient energy, improper laser parameters, inadequate powder distribution, or issues with the material properties, incomplete fusion between adjacent powder particles may occur, creating voids often filled with unmelted particles. Lack-of-fusion porosities are characterized by an

irregular and often elongated morphology. Addressing and minimizing the lack of fusion is crucial in ensuring the reliability and performance of components produced through L-PBF. This incomplete fusion can lead to structural weaknesses, reduced material integrity, and compromised overall quality of the printed object.

- **Shrinkage porosity**: Occurs when the material undergoes cooling and solidification, leading to a reduction in volume. If the cooling is uneven or too rapid, voids or pores may form in the material due to inadequate filling of the melted space. To mitigate shrinkage porosity, careful control of process parameters, such as laser power, scanning speed, and layer thickness, is necessary. Additionally, optimizing the material properties and preheating strategies can help minimize the risk of shrinkage-related defects in L-PBF-manufactured parts.

Reducing or eliminating porosity defects is crucial for achieving high-quality parts through L-PBF. Process optimization, control of laser parameters, proper chamber atmosphere, and powder quality control are among the strategies employed to mitigate porosity and enhance the overall performance of the manufactured components.

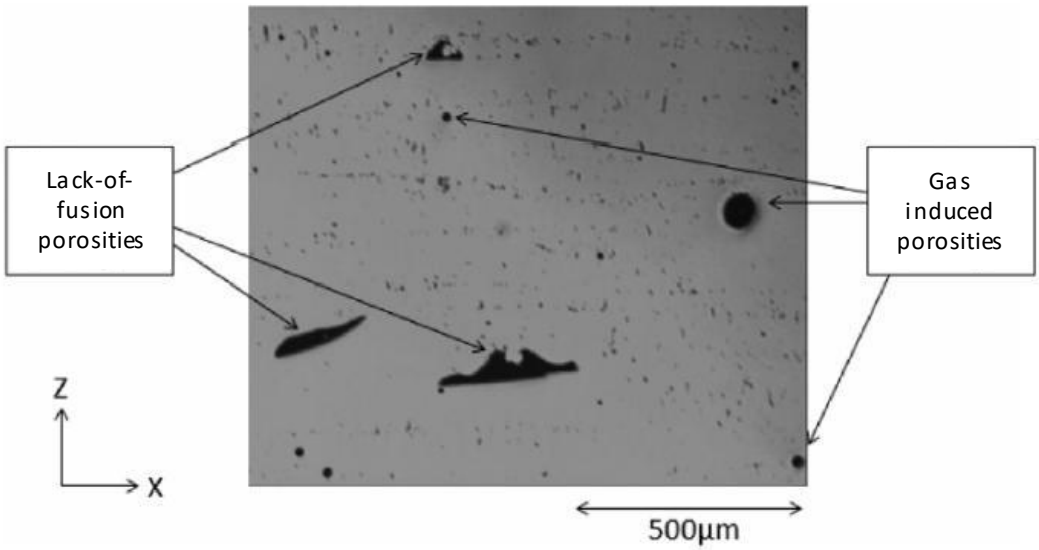

Figure 5. Light optical microscopy showing comparison of process-induced, lack of fusion porosity to intrapped, gas porosity transferred from the powder feedstock [78].

Residual stresses: Owing to the recurrent melting and solidification processes inherent in PBF, characterized by rapid heating and cooling cycles, the resulting printed parts undergo substantial high-temperature gradients. These gradients can give rise to significant residual stresses, ultimately leading to distortions or various macroscopic defects such as cracking, and delamination from the build plate. These issues collectively contribute to a reduction in the print consistency of PBF machines. Various strategies have been investigated to reduce residual stresses and mitigate part distortion in metal Additive Manufacturing. The predominant method involves

reducing the temperature gradient by preheating either the feedstock material or the substrate or performing stress relieving treatments before removing the components from the building platform.

A model of residual stress formation during heating and cooling phases is reported in Figure 6 as proposed in [79]. The residual stress field in AM process is significantly complicated due to the intricate nature of heat source paths and heat transfer patterns, involving a multitude of variables.

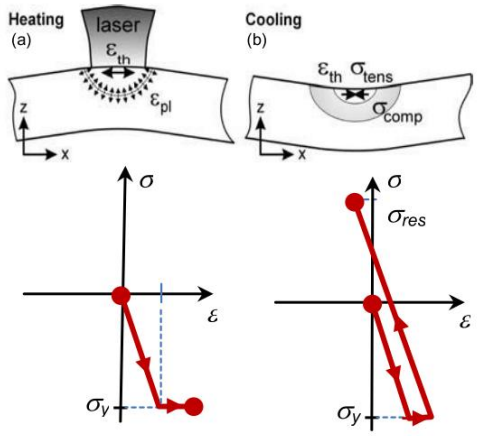

Figure 6. Residual stress formation model: (a) heating-phase, (b) cooling-phase.

Cracks: Solidification cracking and grain boundary cracking are phenomena occurring within the microstructure. Solidification cracks are a phenomenon that particularly affects alloys characterized by a wide range of solidification temperature, high coefficient of thermal expansion, and significant shrinkage during solidification. Usually, the presence of cracks is one of the main features which makes the alloy not processable. The phenomena observed in the mushy zone significantly influence the development of hot cracking, and the associated mechanism is illustrated in Figure 7.

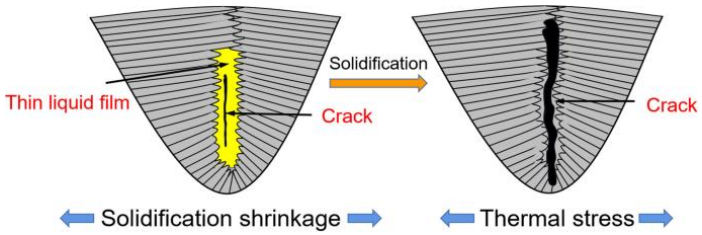

Figure 7. A universal schematic image of the solidification crack of the 6XXX series Al alloy [80].

Oxide Inclusions: The presence of oxide films on the top of melt pools inhibits densification mechanisms, promoting balling phenomena and limiting the wettability of fused particles, thus hindering their coalescence into a dense layer. Oxides may be present in the starting powders or form later due to the interaction of the liquid with the atmosphere if it is not adequately controlled.

It was observed that the oxide layer on the top of the melt pool undergoes vaporization upon exposure to the laser, producing a fume of oxide particles. Simultaneously, the stirring of the melt pool, likely influenced by Marangoni forces, contributes to the disruption of the oxide at the base of the melt pool. Nevertheless, the oxides situated at the sides of the melt pool remaines undisturbed, resulting in the creation of zones characterized by

weakness and porosity. This occurred because the melt pool failed to adequately wet the surrounding material in those areas [81].

Loss of alloying elements: The high energy density used in laser processes can cause selective evaporation of certain alloying elements, especially those with a low melting temperature (and low evaporation temperature), as they tend to have a higher equilibrium vapor pressure than the main component of the alloy.

Balling: A characteristic defect of the L-PBF process that is formed due to inadequate wetting of the molten metal with the underlying layer (Figure 8). These defects prevent the formation of a continuous and homogeneous layer, resulting in a rough surface (sometimes characterized by emerging spherical features). In severe cases, the phenomenon intensifies with the addition of successive layers and can be so pronounced as to block the powder distribution mechanism and can create porosities. Balling is favored by the presence of oxides because they are not effectively wetted by the molten metal and, in combination with thermal stress and poor adhesion between layers, can lead to delamination of the piece.

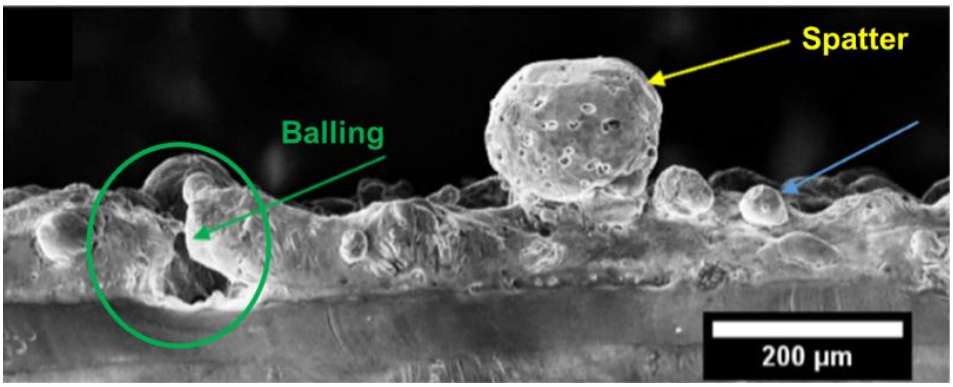

Figure 8. Balling effect caused by high laser power. Yellow arrows represent spatters, green arrow represents balling and blue arrows correspond to partially melted metal powder [82].

Spatter: At elevated power densities, there is a possibility of powder particles or molten droplets being expelled from the molten pool, leading to the formation of spatter. The molten pool undergoes noticeable recoil pressure, primarily caused by the local vaporization of alloying elements. Molten droplets may be discharged when the recoil pressure surpasses the surface tension force at the liquid pool periphery. In the EB-PBF process, powder particles may also be expelled as a result of the strong repulsive electrostatic force. Figure 9 illustrates three distinct categories of spatter. The I type of spatter is formed by the rapid heating of the shield gas, generating a metallic jet directed upward toward the laser beam. The II-type spatter involves droplets created through recoil pressure and the Marangoni effect. The III-type spatter results from the recoil pressure and snowplow effect, generating powder spatter originating from the front line [83].

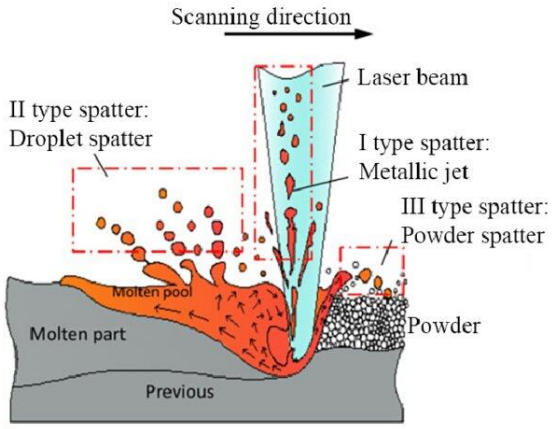

Figure 9. Three different spatter types in powder bed fusion processes [83].

1.6 Materials

The most common materials processed with PBF-based technologies include stainless steel, titanium (Ti), nichel (Ni), aluminum (Al), copper (Cu), and cobalt (Co) alloys [20]. The main metals used in this work are:

I. **Co-Cr-Mo**: This alloy possesses good versatility and durability, along with biocompatibility [21].

II. **Ti-6Al-4V:** one of the most used alloys in AM PBF-based technology. Known for its biocompatibility and high strength-to-density ratio, this alloy finds application in various fields due to its relevant mechanical properties, high corrosion resistance, and good processability, even at high temperatures [22][23].

III. **17-4 PH stainless steel**: This material is chosen for its excellent mechanical properties and corrosion resistance, making it particularly suitable for applications in the aerospace and automotive industries. Additionally, its wear resistance, manufacturability, and biocompatibility make it optimal for the production of medical tools and devices [24,25].

1.2.1 Cobalt alloys

The Cobalt-Chromium (Co–Cr) alloys represent an important category of metallic biomaterials with different applications. A prevalent composition within this series is Co–xCr–yMo–zW, where x ranges from 19 to 30% and y from 5 to 10%. Typically, Co–Cr alloys incorporate 25 to 30 wt% of Cr, providing proper corrosion resistance and making them highly suitable for implant applications. Besides Cr, Mo is a common alloying element, often added up to approximately 6 wt% for solid-solution strengthening [26]. Some alloys may also include trace amounts of W and other elements such as Mn, C, and N. The substantial wear resistance exhibited by Co–Cr alloys results from the formation of precipitates, predominantly Cr-rich carbides and intermetallic phases (σ) [27,28]. Co-Cr alloys find extensive applications in biomedical [29], automotive, and aerospace fields [30]. Co–28Cr–6Mo alloy designated as F75 by ASTM is a standard alloy used in orthopedic implants [31].

In the realm of dental device fabrication, Co-Cr alloys are favored due to their corrosion resistance, ductility, and strength, all of which are well-suited for this specific purpose [32]. Due to the challenges posed by the high

hardness and melting point of these alloys, making conventional processing difficult in dental laboratories, the L-PBF process has emerged as a promising technology for manufacturing Co-Cr alloys. Notably, Co-Cr alloys pose no allergic or carcinogenic hazards [33].

According to Averyanova et al. [34], the L-PBF technique proves to be a suitable method for constructing dental crowns and bridges, offering good geometrical accuracy and adequate mechanical properties. Further affirming this, Revilla Leon et al. [35] successfully printed and implanted a CoCr maxilla framework in an edentulous patient.

The microstructures of Co–Cr alloys produced through additive manufacturing (AM) notably differ from their counterparts in casting and wrought forms due to the accelerated solidification inherent in the AM process [36,37]. Additionally, the unique microstructure of Co–Cr alloys results from the repetitive heating and cooling cycles during layer-by-layer manufacturing and directional solidification along the build orientation. Typical feature of the AM Co–Cr microstructures is the presence of melt pool boundaries (Figure 10). Similar to weld pool boundaries, these boundaries are observable on the longitudinal cross-section and typically exhibit a semi-circular shape (Fig. 10A and 10B). Along the transversal cross-section, the elongated scan tracks are visible, revealing the pattern followed by the laser during the manufacturing process (Fig. 10C). In contrast to the dendritic microstructure of cast structures and the equiaxed microstructure of wrought alloys, the grain structure of AM Co–Cr alloys is columnar, with grain growth occurring along the build direction. However, the precise morphology of the grains is determined by the temperature gradient across the solidification front and the growth velocity of the solidification front [38]. The direction of grain growth is influenced by the energy density and scanning strategy [39].

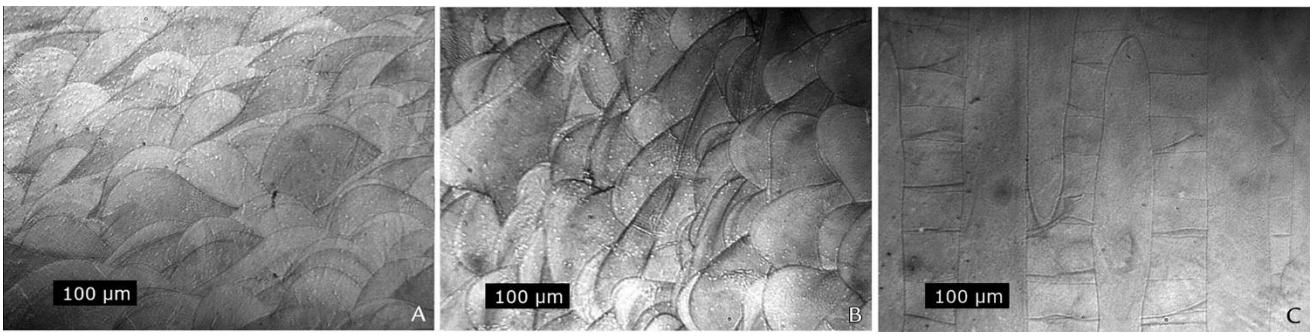

Figure 10. Micrographs (original magnification ×10) showing layered construction in different angulations. A, 0-degree build angle. B, 45-degree build angle. C, 90-degree build angle [40].

For orthopedic applications, the mechanical properties of additively manufactured Co–Cr alloys must meet or exceed those of conventionally processed Co–Cr alloys, as the latter exhibit properties suitable for orthopedic implants in their cast or wrought forms. Studies on the mechanical behavior of Co–Cr alloys prepared by L-PBF and EB-PBF primarily concentrate on microstructural changes resulting from variations in processing parameters or post-processing treatments.

1.2.2 Titanium alloys

Ti6Al4V stands as the predominant α-β Titanium alloy extensively applied in the medical, automotive, and aerospace sectors. Renowned for its exceptional strength, corrosion resistance, and maximal operating temperature of approximately 420 °C, it has become a standard alloy in additive manufacturing processes. These alloys contribute to weight savings in crucial aerospace applications and find use in high-performance sectors like medicine, and automotive industries [41]. Notably, its commendable weldability in a shield atmosphere makes it particularly suitable for L-PBF and EB-PBF technologies [42].

Titanium exhibits two distinct crystal structures, namely hexagonal close-packed (α-phase) and body-centered cubic structure (β-phase). These structural variations are pivotal in the extensive development of titanium alloys tailored for specific characteristics [43–45]. Among these alloys, Ti-6Al-4V stands out as one of the most widely utilized, holding a significant market share in titanium products. Classified as an α-β titanium alloy, Ti-6Al-4V owes its unique properties to the presence of vanadium, which stabilizes the β phase and prevents its transformation at room temperature, resulting in a combination of both α and β phases. Swift cooling from the elevated temperature of β-transus leads to the conversion of the β phase into the unstable α′-martensite phase, forming fine colonies of laths [46]. Renowned for its high strength, low density, excellent corrosion resistance, and superior biocompatibility, Ti-6Al-4 V finds applications in diverse fields, including jet engines, gas turbines, medical implants, and various airframe components [47,48]. Traditional methods like extrusion and forging are employed for the production of titanium parts.

In the context of EB-PBF, the fabricated samples predominantly exhibit acicular α and related β phases, as indicated by microstructural analysis. The thermal gradient in the manufacturing direction promotes the epitaxial formation of prior β grains, extending across multiple layers [49]. Conversely, samples fabricated through L-PBF for Ti–6Al–4V alloys showcase a dominance of columnar β grains and α′ martensitic phases. This is attributed to the rapid cooling of laser-melted powders during the manufacturing process [50–52]. Hence, the distinct corrosion responses observed in L-PBF- and EB-PBF-fabricated samples can be ascribed to variations in the α and β phase contents, as well as differences in the density of α and β phases and lengths of grain boundaries within a specific area [53,54].

The main microstructure of Ti-6Al-4V produced with L-PBF and EB-PBF were reported in Figure 11.

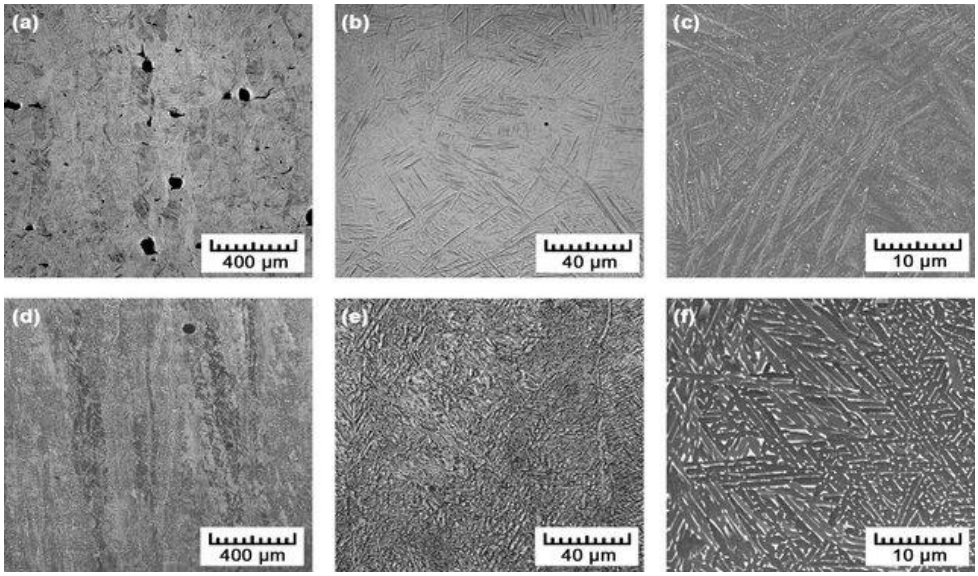

Figure 11. Microstructures of Ti-6Al-4V prepared by a-c) L-PBF, d-f) EB-PBF [55].

Titanium alloys are widely studied in the literature. For example, Fojt et al. [56] examined the corrosion behavior of Ti-6Al-4V alloys produced through EB-PBF and L-PBF techniques in a physiological solution. Their findings suggested that the corrosion resistance of samples fabricated using L-PBF is superior. Liu et al. [57] successfully enhanced both the tensile strength and ductility of L-PBF-processed Ti-6Al-4V by adjusting the process parameters to restrict the formation of α′ martensite. The titanium alloy is used also in EB-PBF process. Haize Galarraga et al. [58] conducted a research investigation into the heat treatment of Ti–6A1–4V alloy processed through EB-PBF. The primary objective of their study was to assess the behavior and mechanical characteristics of EB-PBF-produced Ti–6A1–4V ELI (Extra Low Interstitial) under various heat treatment conditions.

Ti-6Al-4V scaffolds are applied for the treatment of bone disorders. Fogel et al. [59] utilized in vitro testing to clarify the proportional contributions of a porous design to both stiffness and subsidence performance in intervertebral devices. Four sets of titanium cages were generated, incorporating combinations of a porous endplate and/or an internal lattice architecture. The internal lattice architecture reduced cage stiffness by 16.7%, and the porous endplates decreased it by 16.6%. The cage featuring both porous elements exhibited the lowest stiffness, measuring 40.4 kN/mm, with a motion segment stiffness of 1976.8 N/mm for subsidence. The internal lattice architecture did not significantly impact the motion segment stiffness, while the porous endplates notably reduced this value.

1.2.3 17-4 PH stainless steel

Martensitic precipitation-hardening stainless steel has been extensively investigated in the field of AM [60]. One such stainless steel variant is 17–4 PH, recognized for its combination of good corrosion resistance, high strength, and toughness. Post-process heat treatment is often necessary for 17–4 PH stainless steel to meet specific mechanical properties and corrosion resistance requirements. Optimal hardness and strength are typically reached with aging treatment in the temperature range of 480–620 °C, promoting uniform precipitation

of nanometric copper-rich precipitates. The duration of aging depends on the temperature, varying from a few minutes to hours [61]. While commercially wrought 17–4 PH stainless steel shows a martensitic structure, a wide range of contradictory microstructures has been reported in this steel produced through AM, varying with process parameters.

In L-PBF processing under argon (Ar) atmosphere, a dominant martensitic structure with small amounts of retained austenite (RA) has been reported, whereas under an N_2 processing atmosphere, a mixture of martensite and austenite phases (50–75% austenite at different cross-sections) is formed. The formation of these non-equilibrium phases is attributed to high cooling rates, the chemical composition of the original powder, and the thermal history of the specimens [62]. In Figure 12, an optical micrograph of the cross-section parallel to the building direction of an L-PBF as-built 17-4 PH stainless steel sample, processed in N_2 atmosphere, is shown. The partially overlapped melt pools, formed due to the melting of metal powders under the laser action, are clearly shown.

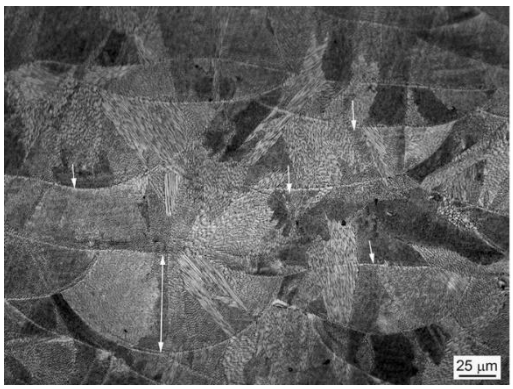

Figure 12. Optical image of longitudinal cross-section (plane B) of L-PBF PH steel sample processed in N2 atmosphere showing distinct melt pools. Short arrows indicate the melt pool boundaries and double-headed arrows show the depth of the melt pool [63].

Mahmoudi et al. [64] investigated the influence of laser additive manufacturing process parameters and heat treatment parameters on both the mechanical properties and microstructures of 17-4PH stainless steel. The study revealed that optimizing the process can enhance the mechanical properties of the material. However, they found that the tensile and fatigue properties of 17-4 PH stainless steel produced through AM are inferior to those of the alloy obtained with conventional technologies [64]. This is explained by the presence of residual austenite and the formation of defects during the manufacturing process, such as gas porosities and balling phenomena, leading to layers folding onto themselves (which occurs when wetting is poor, and the molten liquid does not wet the previous layer due to the formation of an oxide film on the preceding layer, hindering metallurgical bonding between layers [65]).

Post-process heat treatments (e.g., stress relief, solution annealing, and hot isostatic pressing (HIP)) have been shown to enhance the performance, especially in terms of fatigue resistance, of AM-produced parts by eliminating residual stresses, modifying the microstructure, and reducing the size and shape of pores [66]. Rafi et al. [63] explored the impact of various post-fabrication heat treatments on both the mechanical properties and microstructural characteristics of selectively L-PBF17-4 PH stainless steel.

In general, 17-4 PH exhibits superior strength after the H900 treatment (According to the standard ASTM A564, the aging condition of H900 requires a pre-heating of the chamber furnace up to 480 °C, a holding time of 1 h, and after a cooling in air [67]) due to the formation of nanoscale spherical Cu-rich precipitates. Consequently, most studies have applied this heat treatment procedure to 17-4 PH AM products to improve their mechanical properties [68]. For instance, Murr et al. [69] assessed the hardness values of H900 components by comparing Ar and N_2 atomized powders and varying printing shielding atmospheres (Ar and N_2). However, it has recently been demonstrated that while the H900 treatment can significantly enhance the yield strength and ultimate tensile strength of L-PBF-produced 17-4 PH steel pieces, the same treatment can have a detrimental effect on long-term fatigue strength (high cycle fatigue): this is caused by a more severe influence of fusion defects in the material on crack initiation.

Li et al. [70] studied the hardness evolution by conducting various homogenization heat treatments, followed by identical aging processes at 482ºC for 1 h, with the help of thermodynamic and kinetic simulations. The results showed that the wire-based LC coating has a small Heat-affected zone, excellent tensile strength and fracture toughness.

A few works were conducted on the analysis and characterization of L-PBF 17-4PH SS parts. Gu et al. [71] explored the impact of energy density on the microstructure and porosity of 17-4 PH stainless steel components produced through L-PBF. Through the estimation of porosity and examination of microstructure using optical microscopy (OM) and scanning electron microscopy (SEM) images, the researchers concluded that energy density might serve as a limited indicator of porosity levels within L-PBF parts. Notably, coupons manufactured at the same optimal energy density level exhibited significantly divergent levels of porosity. Rafi et al. [72] detailed the impact of powder chemistry, processing environment, and grain size on the mechanical properties and phase content of L-PBF parts. They demonstrated the essential role of heat treatment in achieving the desired tensile properties. Additionally, the researchers observed a higher presence of retained austenite in parts constructed under nitrogen as opposed to those built under argon.

Some examples of optical micrographs of the cross-section parallel to the build direction of microstructures of L-PBF heat-treated 17-4PH samples are shown in Figure 13.

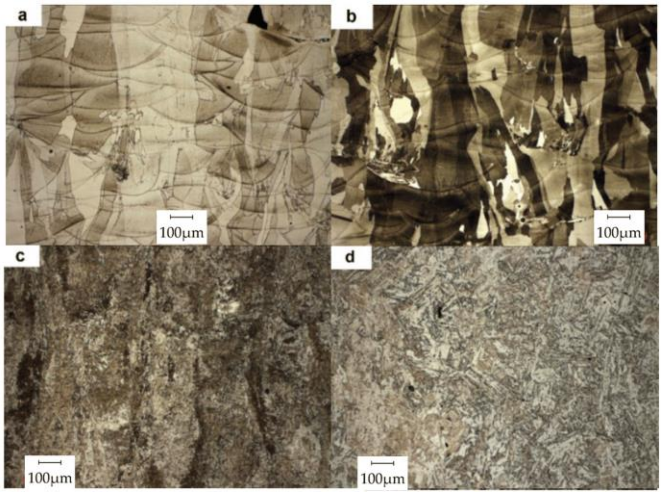

Figure 13. OM cross-section observation of L-PBF 17-4 PH sample after heat treatment: (a) tempered at 480 ◦C/1 h; (b) tempered at 550 ◦C/4 h; (c) solution heat-treated (1040 ◦C/1.5 h), quenched and tempered at 480 ◦C/1 h; (d) homogenized (1190 ◦C/2 h), solution heat-treated (1040 ◦C/1.5 h) and tempered at 480 ◦C/1 h [73].

1.7 Lattice structures

Cellular materials offer unique functional characteristics allowing design freedom beyond the capability of solid materials. These characteristics include the following: high specific strength and stiffness, enhanced absorption of mechanical energy and heat transfer control. Cellular materials are formed by periodic or stochastic arrangements of open or closed cell types (Figure 14), with either two-dimensional cell configurations (such as honey-comb) or three-dimensional polyhedral layouts (such as lattice structures).

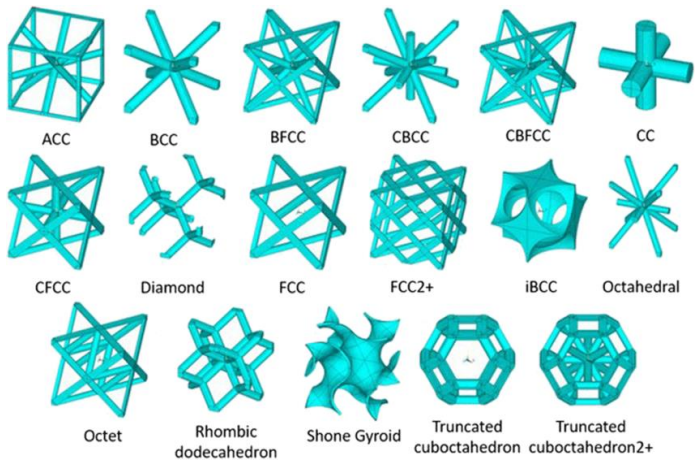

Figure 14. Examples of lattice structure unit cells [84].

In order to identify the type of cellular structures, Dhruv Bhate [85] and Tao and Leu [86] classified the cellular structures in foams (open-cell and closed-cell), honeycombs and lattice structures. Queheillalt et al. [87] and Clough et al. [88] have demonstrated that lattice structures, designed to suppress buckling, exhibit enhanced compressive and shear strength compared to foams and honeycomb structures. Moreover, lattice structures have many superior properties than foams and honeycombs. Specifically, each unit cell and even each strut within the lattice structure can be treated as a design variable, allowing for optimization to meet specific customized

functional requirements. This flexibility in design, implies that the mechanical properties of lattice structures can be more effectively controlled than those of foams and honeycombs. In conclusion, lattice structures typically have better mechanical performance than foam and honeycomb structures [89].

In brief, lattice structures are repetitive patterns that either occupy a volume or conform to a surface. In the realm of engineering design, these structures, inspired often by natural formations, consist of interconnected beams, surfaces, or plates arranged in an ordered or stochastic manner (Figure 15) [90].

The aim of such materials is to enable the possibility to integrate different or relative better mechanical properties [91]. The lattice structures can be analyzed with classical methods of mechanics, taking into account their properties, allowing direct comparison with fully dense materials [92]. The purpose is to create a material with a higher specific stiffness or strength, meaning it can be light and with high strength, or to tailor the mechanical response for the specific application, like being compliant and absorbing impact. The mechanical performance of cellular structures is dependent on cell topology, number of cells, geometric parameters (including strut diameter and cell size), material and manufacturing process characteristics, as well as structural boundary and loading conditions. Adjustment of the cell topology and size allows for the manipulation of the characteristic properties of the cellular material for the desired application requirements.

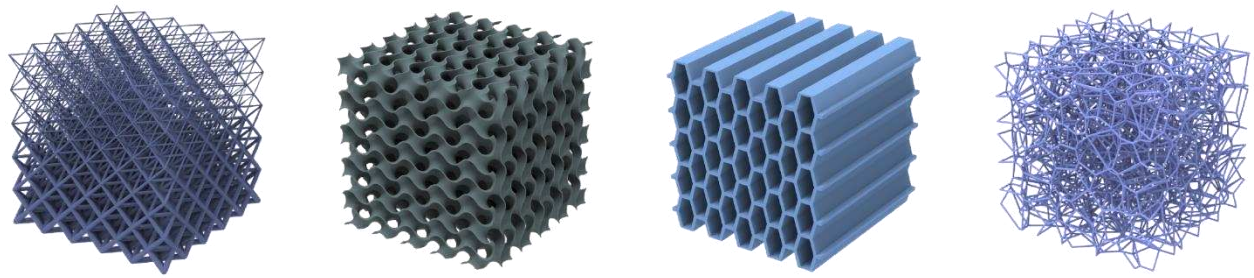

Figure 15. Four types of lattice structures; a beam lattice, a TPMS lattice (gyroid), a honeycomb lattice, and a stochastic lattice (Voronoi) [90].

Metal lattice material can reach excellent mechanical properties: ultralightweight, high specific strength, high specific rigidity, high durability, relatively low mass, and high energy absorption rate. This material class also has excellent functional properties, such as shock absorption, heat dissipation, low thermal conductivity, acoustic absorption, and electromagnetic shielding [93–95]. Mechanical properties such as compressive strength and stiffness are particularly dependent on whether the cell exhibits bending-dominated or stretch-dominated behavior during loading, with stretch-dominated structures showing superior strength and bending-dominated structures showing superior compliance [96].

AM techniques provide an exceptional opportunity to manufacture cellular materials such as lattice structures tailored to dedicated applications. PBF-based processes can produce geometrically complex periodic cellular structures with robust control over uniformity and repeatability. In comparison, traditional metal cellular structure manufacturing processes are limited to stochastic foam production with comparatively low uniformity, or wire mesh lattice with high cost and comparatively lower manufacturable geometric complexity. However, PBF technique is characterized by specific process limits such as minimum manufacturable feature size and

inclination angle for a given build material. These process limits impose constraints on manufacturable geometries and require experimentation to quantify manufacturable lattice design configurations. Furthermore, the application of lattice structures requires that their mechanical properties and failure modes be quantified for varying geometric conditions [97].

Literature has primarily concentrated on examining the feasibility of producing such structures and assessing their mechanical characteristics [98]. An investigation was conducted by Brenne et al. [99], who experimentally explored the compressive behavior of titanium BCC lattice structures fabricated through AM. The authors observed shear failures along diagonal specimen planes. Numerous other studies have highlighted the notable impact of powder bed fusion parameters, including laser speed, power, and layer thickness, on the mechanical properties of the constructed lattice structures.

While the Ti-6Al-4V alloy remains the most studied material for lattice structures due to its high mechanical properties and excellent biocompatibility, other materials such as 316L stainless steel, CoCr, and Al-10Si-Mg have also been explored.

Mines et al. [100] examined the mechanical characteristics of sandwich lattice panels functioning as impact absorbers and load bearers. Morlock et al. [101] explored the mechanical characteristics of an open-cell Co-Cr-Mo structure with a pore size of 0.5 mm. They noted that the structure exhibited mechanical properties comparable to commercially manufactured components using alternative composites. Moreover, their recent discoveries indicate that Co-Cr-Mo cell structures with square pores, fabricated using L-PBF, demonstrate compressive properties similar to those of human bone [12].

In the biomedical field, lattice structures are of particular interest for bone scaffold production [102,103]. Numerous researchers have investigated the feasibility and mechanical properties of porous femoral, hip, and knee implants. Limmahakhun et al. [104] examined a graded femoral stem designed to manage micromotions within an acceptable range for bone ingrowth, featuring a flexural stiffness comparable to that of human bone. Min et al. [105] conducted pressure weakness testing on titanium composite cell structures and observed that the fatigue strength increased with a higher relative thickness and cyclic tightening of the struts within the cell structure, leading to eventual failure. Moreover, Wauthle et al. [106] noted the absence of cytotoxicity and observed favorable bone ingrowth in an in vivo experiment involving a lattice tantalum implant on a rat femur.

The structural accuracy of lattices fabricated through L-PBF can be characterized by considering both the strut size and structural porosity and comparing them with the intended design. Two factors, influenced by process parameters, contribute to deviations between the target design and the geometry produced by L-PBF. Firstly, residual partially melted powders on the struts lead to an increased strut diameter and higher nominal density. Arabnejad et al. [107] noted that the lattice's pore size is typically smaller than designed, causing a significant difference in structural porosity. Additionally, the inclined struts often end up larger than the target design due to the staircase effect associated with building inclined geometries. The second factor involves the impact of the laser thermal footprint, resulting in a laser track width (LTW) larger than the laser spot size.

Among the different challenges in the design, production and characterization of components containing a lattice structure, the interaction between the lattice itself and a solid surface or a bulk part, represents a crucial topic. In fact, purely lattice components are rarely produced, more often the lattice is surrounded by or connected to solid walls, which can influence the mechanical behavior of the component.

In this regard, Güden et al. [108] investigated the effect of the number of cells, strut diameter and rigid-face sheets on the compression behavior of EB-PBF-Ti-6Al-4V Body Centered Cubic lattices. The addition of a dense layer that covered the lattice core altered the behavior of the structure compared with the lattice without a solid shell. The solid layer constrained the edge of the lattice and the fracture mode changed with and without the solid face sheets. Moreover, the mechanical properties of foam-filled tubes were investigated by Novak et al [16]. In this study, thin-walled tubes were filled with various metal lattices. The interaction between tube and lattice structures gave a positive contribution to the energy absorption increasing the impact properties. This application results useful not only for the biomedical application but also for the automotive, marine aerospace and railway industries. Furthermore, Xiong et al. [109] studied porous metallic scaffolds with dense core structure with different diameters for testing the effectiveness in enhancing the strength of the scaffold. The tested lattice structures with dense core exhibited the mechanical features and a level of porosity favorable for biomedical applications. Finally, Fu et al. [110] focused on the mechanical properties of triply periodic minimal surface shell lattices produced by micro laser powder bed fusion. The lightweight design was analyzed, and the deformation mechanisms and mechanical properties of the shell lattices were correlated to the relative density. The deformation mechanism was highly dependent on the relative density, and the discrepancy between the design and measured values of the shell thickness was a crucial point, especially for the low-density structures. These studies revealed that the addition of the solid part resulted in an increase of mechanical properties due to the higher load support than the lattice without shell. Moreover, enhanced compression strength and energy absorption were also detected maintaining a good level of porosity of the samples.

Nowadays, lattice structures are widely studied. However, challenges and limitations exist in exploiting their potential. One of the most important point is the choice of materials for lattice structures which can significantly impact their mechanical performance. Limited material options with suitable properties for certain applications can be a constraint.

Achieve precise and uniform lattice structures during fabrication can be also challenging. The complexity of lattice designs must be taken into account. Designing optimal lattice structures tailored to specific functional features require the use of sophisticated computational tools and methods. A standardized guide for the production of lattice structure has not yet been realized but is still the subject of research.

Moreover, another key point of lattice structures is the interaction with a solid component. The relevance of the interface between the lattice and solid part is based on how strong the connection is and how it influences the mechanical behavior of the whole structure. The abrupt change in density (from struts to the solid part), and the

presence of defects in the interface have to be considered to investigate the strength and reliability of the connection.

Addressing these challenges through continued research and development will contribute to the broader acceptance and application of lattice structures in various scientific and engineering domains.

1.8 Finite Element Analysis

Finite Element Analysis (FEA) is a powerful tool in the engineering world for the study of many complex physical problems. The Finite Element Method (FEM) allows engineer to simulate and analyze physical problems including mechanical or thermal aspects, as well as fluid dynamic and so on. The FEA is widely use in mechanical engineering during the development and design phase, to help evaluating if the product will perform as planned or if it will be suitable for the expected operation environment for the desired application. FEA methods are also used to reduce the number of physical prototypes and can be used to run virtual simulation to optimize the design.

1.2.4 Process simulation

The conventional approach of utilizing trial and error to attain optimal part quality is typically both time-consuming and expensive. Recently, there has been a focus on employing simulations for Additive Manufacturing (AM) processes. These simulations aim to optimize process parameters and forecast the occurrence of defects within or near the melt pool. The aim is to identify strategies to prevent the formation of defects, thereby enabling process optimization without in-line production trials. This approach offers significant economic benefits and time savings.

Numerous studies have delved into simulating the formation of defects like balling and spattering. Khairallah et al. [111] examined the occurrence of keyhole-induced defects with respect to variations in laser power. Tang et al. [112] simulated the lack of fusion porosity, determining at which values of process parameters, such as layer thickness and hatch spacing, the porosity increases. Furthermore, Vastola et al. [113] developed the model and numerical simulations offering a convenient and precise means of predicting porosity in the laser powder-bed fusion process. These tools can be utilized to enhance comprehension, regulation, and mitigation of porosity in metal additive manufacturing components.

In the literature, the simulation of powder bed and the prediction of porosity formations are widely studied. In this regard, the macroscopical process simulation, based on the variation of process parameters, such as scanning speed and laser power, is investigated with Deform 3D. The main aim was to simulate the L-PBF process varying the process parameters, comparing the residual stresses of final parts with the experimental ones, in order to achieve the optimal parameters needed to print the samples saving time and money.

1.2.5 Mechanical simulations

As already mentioned, FEA analysis is widely used to predict the behavior of components during the design phase and represent a powerful tool to reduce the number of prototypes. When considering lattice structures,

FEA can be of extreme importance in the prediction of their behavior. In literature, a number of studies are reported concerning how to implement and study these materials. Sadeghi et. al [114] tested additively manufactured stainless steel lattice cylinders and their equivalent hollow cylinders. Lattice cylinders exhibit lower transmitted force in Split Hopkinson bar experiments with a stiffness reduction. Additional energy absorption mechanisms in lattice cylinders transform the transmitted force into lateral deformation. FE simulations qualitatively capture specimen behavior, aiding understanding of dynamic lattice structure behavior and studying effects of strain rate hardening, thermal softening, and friction. Three distinct force-displacement regimes are observed: elastic, plastic (hardening), and post-buckling (softening). Increasing the loading rate by five orders of magnitude results in a up to 36% peak force increase, attributed to strain rate hardening in the stainless-steel material. Li et al. [115] conducted compression tests on lattice structures of stainless steel 316L manufactured through L-PBF with a body-centered cubic (BCC) unit cell topology. To evaluate the experimental compression tests, a dynamic explicit finite element (FE) model was generated, incorporating a material model derived from the elastoplastic behavior of the fabricated struts. Ahmadi et al. [116] provided analytical solutions and explicit relationships to predict the elastic modulus, Poisson ratio, critical buckling load, and yield stress of cellular structures employing the diamond lattice unit cell. The analytical findings were juxtaposed with results derived from finite element simulations and experimental measurements conducted on Ti6Al4V specimens fabricated through selective laser melting.

However, there is still no an established method and, as far as the author knows, the choice of many parameters and configuration of the analysis still relies on several idealizations and assumptions dictated mostly by the uncertainty on the effective properties that these materials possess.

References

[1] Bahnini I, Rivette M, Rechia A, Siadat A, Elmesbahi A. Additive manufacturing technology: the status, applications, and prospects. International Journal of Advanced Manufacturing Technology 2018;97:147–61. https://doi.org/10.1007/s00170-018-1932-y.

[2] Frazier WE. Metal additive manufacturing: A review. J Mater Eng Perform 2014;23:1917–28. https://doi.org/10.1007/s11665-014-0958-z.

[3] Kladovasilakis N, Charalampous P, Kostavelis I, Tzetzis D, Tzovaras D. Impact of metal additive manufacturing parameters on the powder bed fusion and direct energy deposition processes: a comprehensive review. Progress in Additive Manufacturing 2021;6:349–65. https://doi.org/10.1007/s40964-021-00180-8.

[4] Tan C, Li R, Su J, Du D, Du Y, Attard B, et al. Review on field assisted metal additive manufacturing. Int J Mach Tools Manuf 2023;189. https://doi.org/10.1016/j.ijmachtools.2023.104032.

[5] Al-Maharma AY, Patil SP, Markert B. Effects of porosity on the mechanical properties of additively manufactured components: a critical review. Mater Res Express 2020;7. https://doi.org/10.1088/2053-1591/abcc5d.

[6] Shellabear M, Nyrhilä O. DMLS-DEVELOPMENT HISTORY AND STATE OF THE ART. n.d.

[7] From the Printer into the Body - Metal 3D Printing in Medicine. Https://WwwProtolabsCom/En-Gb/Resources/White-Papers/from-the-Printer-into-the-Body-Metal-3d-Printing-in-Medicine/#1 n.d.

[8] Oliveira JP, LaLonde AD, Ma J. Processing parameters in laser powder bed fusion metal additive manufacturing. Mater Des 2020;193. https://doi.org/10.1016/j.matdes.2020.108762.

[9] Fotovvati B, Wayne SF, Lewis G, Asadi E. A Review on Melt-Pool Characteristics in Laser Welding of Metals. Advances in Materials Science and Engineering 2018;2018. https://doi.org/10.1155/2018/4920718.

[10] Chowdhury S, Yadaiah N, Prakash C, Ramakrishna S, Dixit S, Gupta LR, et al. Laser powder bed fusion: a state-of-the-art review of the technology, materials, properties & defects, and numerical modelling. Journal of Materials Research and Technology 2022;20:2109–72. https://doi.org/10.1016/j.jmrt.2022.07.121.

[11] Vukkum VB, Gupta RK. Review on corrosion performance of laser powder-bed fusion printed 316L stainless steel: Effect of processing parameters, manufacturing defects, post-processing,

feedstock, and microstructure. Mater Des 2022;221. https://doi.org/10.1016/j.matdes.2022.110874.

[12] Stopyra W, Gruber K, Smolina I, Kurzynowski T, Kuźnicka B. Laser powder bed fusion of AA7075 alloy: Influence of process parameters on porosity and hot cracking. Addit Manuf 2020;35. https://doi.org/10.1016/j.addma.2020.101270.

[13] Esmaeilizadeh R, Ali U, Keshavarzkermani A, Mahmoodkhani Y, Marzbanrad E, Toyserkani E. On the effect of spatter particles distribution on the quality of Hastelloy X parts made by laser powder-bed fusion additive manufacturing. J Manuf Process 2019;37:11–20. https://doi.org/10.1016/j.jmapro.2018.11.012.

[14] Fu Z, Körner C. Actual state-of-the-art of electron beam powder bed fusion. European Journal of Materials 2022;2:54–116. https://doi.org/10.1080/26889277.2022.2040342.

[15] Milberg J, Sigl M. Electron beam sintering of metal powder. Production Engineering 2008;2:117–22. https://doi.org/10.1007/s11740-008-0088-2.

[16] Gruber S, Grunert C, Riede M, López E, Marquardt A, Brueckner F, et al. Comparison of dimensional accuracy and tolerances of powder bed based and nozzle based additive manufacturing processes. J Laser Appl 2020;32. https://doi.org/10.2351/7.0000115.

[17] Liu Z, Zhao D, Wang P, Yan M, Yang C, Chen Z, et al. Additive manufacturing of metals: Microstructure evolution and multistage control. J Mater Sci Technol 2022;100:224–36. https://doi.org/10.1016/j.jmst.2021.06.011.

[18] Tonelli L. Revealing the Hierarchical Microstructure of Innovative Additively Manufactured Metal Parts with Conventional Light Microscopy. Metallography, Microstructure, and Analysis 2021;10:278–82. https://doi.org/10.1007/s13632-021-00721-1.

[19] Zhong Y, Rännar LE, Liu L, Koptyug A, Wikman S, Olsen J, et al. Additive manufacturing of 316L stainless steel by electron beam melting for nuclear fusion applications. Journal of Nuclear Materials 2017;486:234–45. https://doi.org/10.1016/j.jnucmat.2016.12.042.

[20] Cantaboni F, Ginestra P, Tocci M, Ceretti E, De Sio G, Cao X, et al. Selective Laser Melting of Ti-6Al-4V Lattices: Case Study on a Spinal Cage Prosthesis. Key Eng Mater, vol. 926 KEM, Trans Tech Publications Ltd; 2022, p. 147–58. https://doi.org/10.4028/p-g7ip54.

[21] Wang JH, Ren J, Liu W, Wu XY, Gao MX, Bai PK. Effect of selective laser melting process parameters on microstructure and properties of co-cr alloy. Materials 2018;11. https://doi.org/10.3390/ma11091546.

[22] Sing SL, An J, Yeong WY, Wiria FE. Laser and electron-beam powder-bed additive manufacturing of metallic implants: A review on processes, materials and designs. Journal of Orthopaedic Research 2016;34:369–85. https://doi.org/10.1002/jor.23075.

[23] Onuike B, Bandyopadhyay A. Additive manufacturing of Inconel 718 – Ti6Al4V bimetallic structures. Addit Manuf 2018;22:844–51. https://doi.org/10.1016/j.addma.2018.06.025.

[24] Giganto S, Martínez-Pellitero S, Barreiro J, Zapico P. Influence of 17-4 PH stainless steel powder recycling on properties of SLM additive manufactured parts. Journal of Materials Research and Technology 2022;16:1647–58. https://doi.org/10.1016/j.jmrt.2021.12.089.

[25] Ariza-Galván E, Montealegre-Meléndez I, Pérez-Soriano EM, Neubauer E, Kitzmantel M, Arévalo C. Influence of Processing Conditions on the Mechanical Properties of 17-4PH Specimens Produced by Additive Manufacturing. Machines 2022;10. https://doi.org/10.3390/machines10110976.

[26] Acharya S, Soni R, Suwas S, Chatterjee K. Additive manufacturing of Co–Cr alloys for biomedical applications: A concise review. J Mater Res 2021;36:3746–60. https://doi.org/10.1557/s43578-021-00244-z.

[27] Al Jabbari YS. Physico-mechanical properties and prosthodontic applications of Co-Cr dental alloys: A review of the literature. Journal of Advanced Prosthodontics 2014;6:138–45. https://doi.org/10.4047/jap.2014.6.2.138.

[28] Narushima T, Ueda K, Alfirano. Co-Cr Alloys as Effective Metallic Biomaterials, 2015, p. 157–78. https://doi.org/10.1007/978-3-662-46836-4_7.

[29] Allegri G, Colpani A, Ginestra PS, Attanasio A. An experimental study on micro-milling of a medical grade Co-Cr-Mo alloy produced by selective laser melting. Materials 2019;12. https://doi.org/10.3390/ma12132208.

[30] Mergulhão MV, Podestá CE, das Neves MDM. Mechanical properties and microstructural characterization of cobalt-chromium (CoCr) obtained by casting and selective laser melting (SLM). Materials Science Forum, vol. 899 MSF, Trans Tech Publications Ltd; 2017, p. 534–9. https://doi.org/10.4028/www.scientific.net/MSF.899.534.

[31] Chen Q, Thouas GA. Metallic implant biomaterials. Materials Science and Engineering R: Reports 2015;87:1–57. https://doi.org/10.1016/j.mser.2014.10.001.

[32] Ren L, Memarzadeh K, Zhang S, Sun Z, Yang C, Ren G, et al. A novel coping metal material CoCrCu alloy fabricated by selective laser melting with antimicrobial and antibiofilm properties. Materials Science and Engineering C 2016;67:461–7. https://doi.org/10.1016/j.msec.2016.05.069.

[33] Kim HR, Jang SH, Kim YK, Son JS, Min BK, Kim KH, et al. Microstructures and mechanical properties of Co-Cr dental alloys fabricated by three CAD/CAM-based processing techniques. Materials 2016;9. https://doi.org/10.3390/MA9070596.

[34] Averyanova M, Bertrand P, Verquin B. Manufacture of Co-Cr dental crowns and bridges by selective laser Melting technology: This paper presents the successful application of the selective laser melting technology in dental frameworks manufacturing from Co-Cr alloy using Phenix PM 100T dental machine over a production period of 14 months. Virtual Phys Prototyp 2011;6:179–85. https://doi.org/10.1080/17452759.2011.619083.

[35] Revilla León M, Klemm IM, García-Arranz J, Özcan M. 3D Metal Printing - Additive Manufacturing Technologies for Frameworks of Implant-Borne Fixed Dental Prosthesis. Eur J Prosthodont Restor Dent 2017;25:143–7. https://doi.org/10.1922/EJPRD_RevillaLeon05.

[36] Mengucci P, Barucca G, Gatto A, Bassoli E, Denti L, Fiori F, et al. Effects of thermal treatments on microstructure and mechanical properties of a Co-Cr-Mo-W biomedical alloy produced by laser sintering. J Mech Behav Biomed Mater 2016;60:106–17. https://doi.org/10.1016/j.jmbbm.2015.12.045.

[37] Lu Y, Wu S, Gan Y, Li J, Zhao C, Zhuo D, et al. Investigation on the microstructure, mechanical property and corrosion behavior of the selective laser melted CoCrW alloy for dental application. Materials Science and Engineering C 2015;49:517–25. https://doi.org/10.1016/j.msec.2015.01.023.

[38] DebRoy T, Wei HL, Zuback JS, Mukherjee T, Elmer JW, Milewski JO, et al. Additive manufacturing of metallic components – Process, structure and properties. Prog Mater Sci 2018;92:112–224. https://doi.org/10.1016/j.pmatsci.2017.10.001.

[39] Zhou X, Li K, Zhang D, Liu X, Ma J, Liu W, et al. Textures formed in a CoCrMo alloy by selective laser melting. J Alloys Compd 2015;631:153–64. https://doi.org/10.1016/j.jallcom.2015.01.096.

[40] Alexandrino LD, Henrique L, Antunes M, Luiz A, Munhoz J, Pedro A, et al. Mechanical and surface properties of CoeCr alloy produced by additive manufacturing for removable partial denture frameworks. n.d.

[41] Siengchin S. A review on lightweight materials for defence applications: Present and future developments. Defence Technology 2023;24:1–17. https://doi.org/10.1016/j.dt.2023.02.025.

[42] Meier B, Warchomicka F, Petrusa J, Kaindl R, Waldhauser W, Sommitsch C. High Temperature Tensile Strength of TI6AL4V Processed by L-PBF—Influence of Microstructure

and Heat Treatment. BHM Berg- Und Hüttenmännische Monatshefte 2023;168:247–53. https://doi.org/10.1007/s00501-023-01346-3.

[43] Yadroitsev I, Krakhmalev P, Yadroitsava I. Selective laser melting of Ti6Al4V alloy for biomedical applications: Temperature monitoring and microstructural evolution. J Alloys Compd 2014;583:404–9. https://doi.org/10.1016/j.jallcom.2013.08.183.

[44] Atapour M, Pilchak AL, Frankel GS, Williams JC. Corrosion behavior of β titanium alloys for biomedical applications. Materials Science and Engineering C 2011;31:885–91. https://doi.org/10.1016/j.msec.2011.02.005.

[45] Azarniya A, Colera XG, Mirzaali MJ, Sovizi S, Bartolomeu F, St Weglowski M k., et al. Additive manufacturing of Ti–6Al–4V parts through laser metal deposition (LMD): Process, microstructure, and mechanical properties. J Alloys Compd 2019;804:163–91. https://doi.org/10.1016/j.jallcom.2019.04.255.

[46] De Baere D, Mohanty S, Hattel JH. Microstructural modelling of above β-transus heat treatment of additively manufactured Ti-6Al-4V using cellular automata. Mater Today Commun 2020;24. https://doi.org/10.1016/j.mtcomm.2020.101031.

[47] Cremasco A, Messias AD, Esposito AR, Duek EADR, Caram R. Effects of alloying elements on the cytotoxic response of titanium alloys. Materials Science and Engineering C 2011;31:833–9. https://doi.org/10.1016/j.msec.2010.12.013.

[48] Cheng D, Zhang J, Shi T, Li G, Shi J, Lu L, et al. Microstructure and mechanical properties of additive manufactured Ti-6Al-4V components by annular laser metal deposition in a semi-open environment. Opt Laser Technol 2021;135. https://doi.org/10.1016/j.optlastec.2020.106640.

[49] Shahali H, Jaggessar A, Yarlagadda PKDV. Recent Advances in Manufacturing and Surface Modification of Titanium Orthopaedic Applications. Procedia Eng, vol. 174, Elsevier Ltd; 2017, p. 1067–76. https://doi.org/10.1016/j.proeng.2017.01.259.

[50] Jamshidinia M, Atabaki MM, Zahiri M, Kelly S, Sadek A, Kovacevic R. Microstructural modification of Ti-6Al-4V by using an in-situ printed heat sink in Electron Beam Melting® (EBM). J Mater Process Technol 2015;226:264–71. https://doi.org/10.1016/j.jmatprotec.2015.07.006.

[51] Tan XP, Tan YJ, Chow CSL, Tor SB, Yeong WY. Metallic powder-bed based 3D printing of cellular scaffolds for orthopaedic implants: A state-of-the-art review on manufacturing, topological design, mechanical properties and biocompatibility. Materials Science and Engineering C 2017;76:1328–43. https://doi.org/10.1016/j.msec.2017.02.094.

[52] Shahali H, Jaggessar A, Yarlagadda PKDV. Recent Advances in Manufacturing and Surface Modification of Titanium Orthopaedic Applications. Procedia Eng, vol. 174, Elsevier Ltd; 2017, p. 1067–76. https://doi.org/10.1016/j.proeng.2017.01.259.

[53] Qiu W, Wei Y, Chen A, Deng H, Zhou L, Zuo H, et al. Corrosion behavior of additive manufactured Ti-6Al-4V in sulfamic acid cleaning solution. New Journal of Chemistry 2021;45:2967–73. https://doi.org/10.1039/d0nj05731b.

[54] Chiu TM, Mahmoudi M, Dai W, Elwany A, Liang H, Castaneda H. Corrosion assessment of Ti-6Al-4V fabricated using laser powder-bed fusion additive manufacturing. Electrochim Acta 2018;279:143–51. https://doi.org/10.1016/j.electacta.2018.04.189.

[55] Roudnicka M, Misurak M, Vojtech D. Differences in the Response of Additively Manufactured Titanium Alloy to Heat Treatment-Comparison between SLM and EBM. MANUFACTURING TECHNOLOGY 2019;19.

[56] Fojt J, Fousova M, Jablonska E, Joska L, Hybasek V, Pruchova E, et al. Corrosion behaviour and cell interaction of Ti-6Al-4V alloy prepared by two techniques of 3D printing. Materials Science and Engineering C 2018;93:911–20. https://doi.org/10.1016/j.msec.2018.08.066.

[57] Liu J, Sun Q, Zhou C, Wang X, Li H, Guo K, et al. Achieving Ti6Al4V alloys with both high strength and ductility via selective laser melting. Materials Science and Engineering: A 2019;766. https://doi.org/10.1016/j.msea.2019.138319.

[58] Galarraga H, Warren RJ, Lados DA, Dehoff RR, Kirka MM, Nandwana P. Effects of heat treatments on microstructure and properties of Ti-6Al-4V ELI alloy fabricated by electron beam melting (EBM). Materials Science and Engineering: A 2017;685:417–28. https://doi.org/10.1016/j.msea.2017.01.019.

[59] Fogel G, Martin N, Lynch K, Pelletier MH, Wills D, Wang T, et al. Subsidence and fusion performance of a 3D-printed porous interbody cage with stress-optimized body lattice and microporous endplates - a comprehensive mechanical and biological analysis. Spine Journal 2022;22:1028–37. https://doi.org/10.1016/j.spinee.2022.01.003.

[60] Haghdadi N, Laleh M, Moyle M, Primig S. Additive manufacturing of steels: a review of achievements and challenges. J Mater Sci 2021;56:64–107. https://doi.org/10.1007/s10853-020-05109-0.

[61] Wang Z, Fang X, Li H, Liu W. Atom Probe Tomographic Characterization of Nanoscale Cu-Rich Precipitates in 17-4 Precipitate Hardened Stainless Steel Tempered at Different Temperatures. Microscopy and Microanalysis, vol. 23, Cambridge University Press; 2017, p. 340–9. https://doi.org/10.1017/S1431927616012629.

[62] Sabooni S, Chabok A, Feng SC, Blaauw H, Pijper TC, Yang HJ, et al. Laser powder bed fusion of 17–4 PH stainless steel: A comparative study on the effect of heat treatment on the microstructure evolution and mechanical properties. Addit Manuf 2021;46. https://doi.org/10.1016/j.addma.2021.102176.

[63] Rafi HK, Pal D, Patil N, Starr TL, Stucker BE. Microstructure and Mechanical Behavior of 17-4 Precipitation Hardenable Steel Processed by Selective Laser Melting. J Mater Eng Perform 2014;23:4421–8. https://doi.org/10.1007/s11665-014-1226-y.

[64] Mahmoudi M, Elwany A, Yadollahi A, Thompson SM, Bian L, Shamsaei N. Mechanical properties and microstructural characterization of selective laser melted 17-4 PH stainless steel. Rapid Prototyp J 2017;23:280–94. https://doi.org/10.1108/RPJ-12-2015-0192.

[65] Yap CY, Chua CK, Dong ZL, Liu ZH, Zhang DQ, Loh LE, et al. Review of selective laser melting: Materials and applications. Appl Phys Rev 2015;2. https://doi.org/10.1063/1.4935926.

[66] Sarkar S, Siva Kumar C, Kumar Nath A. Effect of mean stresses on mode of failures and fatigue life of selective laser melted stainless steel. Materials Science and Engineering: A 2017;700:92–106. https://doi.org/10.1016/j.msea.2017.05.118.

[67] Pellegrini A, Lavecchia F, Guerra MG, Galantucci LM. Influence of aging treatments on 17–4 PH stainless steel parts realized using material extrusion additive manufacturing technologies. International Journal of Advanced Manufacturing Technology 2023;126:163–78. https://doi.org/10.1007/s00170-023-11136-3.

[68] Yadollahi A, Shamsaei N, Thompson SM, Elwany A, Bian L. Effects of building orientation and heat treatment on fatigue behavior of selective laser melted 17-4 PH stainless steel. Int J Fatigue 2017;94:218–35. https://doi.org/10.1016/j.ijfatigue.2016.03.014.

[69] 17-4PH intro_11 n.d.

[70] Li K, Zhan J, Yang T, To AC, Tan S, Tang Q, et al. Homogenization timing effect on microstructure and precipitation strengthening of 17–4PH stainless steel fabricated by laser powder bed fusion. Addit Manuf 2022;52. https://doi.org/10.1016/j.addma.2022.102672.

[71] Gu H, Rafi HK. Influences of Energy Density on Porosity and Microstructure of Selective Laser Melted 17-4PH Stainless Steel. 2013.

[72] Rafi HK, Pal D, Patil N, Starr TL, Stucker BE. Microstructure and Mechanical Behavior of 17-4 Precipitation Hardenable Steel Processed by Selective Laser Melting. J Mater Eng Perform 2014;23:4421–8. https://doi.org/10.1007/s11665-014-1226-y.

[73] Zitelli C, Folgarait P, Di Schino A. Laser powder bed fusion of stainless steel grades: A review. Metals (Basel) 2019;9. https://doi.org/10.3390/met9070731.

[74] Olakanmi EO, Cochrane RF, Dalgarno KW. A review on selective laser sintering/melting (SLS/SLM) of aluminium alloy powders: Processing, microstructure, and properties. Prog Mater Sci 2015;74:401–77. https://doi.org/10.1016/j.pmatsci.2015.03.002.

[75] Xue L, Atli KC, Zhang C, Hite N, Srivastava A, Leff AC, et al. Laser Powder Bed Fusion of Defect-Free NiTi Shape Memory Alloy Parts with Superior Tensile Superelasticity. Acta Mater 2022;229. https://doi.org/10.1016/j.actamat.2022.117781.

[76] Agarwala M, Bourell D, Beaman J, Marcus H, Barlow J, Haase P, et al. Post-processing of selective laser sintered metal parts. Rapid Prototyp J 1995;1:36–44.

[77] Aboulkhair NT, Everitt NM, Ashcroft I, Tuck C. Reducing porosity in AlSi10Mg parts processed by selective laser melting. Addit Manuf 2014;1:77–86. https://doi.org/10.1016/j.addma.2014.08.001.

[78] Sames WJ, List FA, Pannala S, Dehoff RR, Babu SS. The metallurgy and processing science of metal additive manufacturing. International Materials Reviews 2016;61:315–60. https://doi.org/10.1080/09506608.2015.1116649.

[79] Li C, Liu ZY, Fang XY, Guo YB. Residual Stress in Metal Additive Manufacturing. Procedia CIRP, vol. 71, Elsevier B.V.; 2018, p. 348–53. https://doi.org/10.1016/j.procir.2018.05.039.

[80] Li F, Zhang T, Wu Y, Chen C, Zhou K. Microstructure, mechanical properties, and crack formation of aluminum alloy 6063 produced via laser powder bed fusion. J Mater Sci 2022;57:9631–45. https://doi.org/10.1007/s10853-022-06993-4.

[81] Louvis E, Fox P, Sutcliffe CJ. Selective laser melting of aluminium components. J Mater Process Technol 2011;211:275–84. https://doi.org/10.1016/j.jmatprotec.2010.09.019.

[82] Nasab MH, Gastaldi D, Lecis NF, Vedani M. On morphological surface features of the parts printed by selective laser melting (SLM). Addit Manuf 2018;24:373–7. https://doi.org/10.1016/j.addma.2018.10.011.

[83] Kivirasi E, Piili H, Minet-Lallemand K, Kotila J. Detecting spattering phenomena by using high speed imaging in L-PBD of 316 L. Procedia CIRP, vol. 94, Elsevier B.V.; 2020, p. 398–403. https://doi.org/10.1016/j.procir.2020.09.153.

[84] Refai K, Montemurro M, Brugger C, Saintier N. Determination of the effective elastic properties of titanium lattice structures. Mechanics of Advanced Materials and Structures 2020;27:1966–82. https://doi.org/10.1080/15376494.2018.1536816.

[85] Case Western Reserve University, IEEE Instrumentation and Measurement Society, Institute of Systems Control and Instrumentation Engineers, Institute of Electrical and Electronics Engineers. ISFA 2016 : International Symposium on Flexible Automation : August 1-3, 2016, Cleveland, Ohio. n.d.

[86] Bhate D. Four questions in cellular material design. Materials 2019;12. https://doi.org/10.3390/ma12071060.

[87] Queheillalt DT, Wadley HNG. Cellular metal lattices with hollow trusses. Acta Mater 2005;53:303–13. https://doi.org/10.1016/j.actamat.2004.09.024.

[88] Clough EC, Ensberg J, Eckel ZC, Ro CJ, Schaedler TA. Mechanical performance of hollow tetrahedral truss cores. Int J Solids Struct 2016;91:115–26. https://doi.org/10.1016/j.ijsolstr.2016.04.006.

[89] Pan C, Han Y, Lu J. Design and optimization of lattice structures: A review. Applied Sciences (Switzerland) 2020;10:1–36. https://doi.org/10.3390/APP10186374.

[90] Guide to lattice structures in additive manufacturing. Https://WwwNtopCom/Resources/Blog/Guide-to-Lattice-Structures-in-Additive-Manufacturing/ n.d.

[91] Barthelat F. Architectured materials in engineering and biology: Fabrication, structure, mechanics and performance. International Materials Reviews 2015;60:413–30. https://doi.org/10.1179/1743280415Y.0000000008.

[92] Ashby MF. The properties of foams and lattices. Philosophical Transactions of the Royal Society A: Mathematical, Physical and Engineering Sciences 2006;364:15–30. https://doi.org/10.1098/rsta.2005.1678.

[93] Salem H, Carter LN, Attallah MM, Salem HG. Influence of processing parameters on internal porosity and types of defects formed in Ti6Al4V lattice structure fabricated by selective laser melting. Materials Science and Engineering: A 2019;767. https://doi.org/10.1016/j.msea.2019.138387.

[94] Yan C, Hao L, Hussein A, Young P, Raymont D. Advanced lightweight 316L stainless steel cellular lattice structures fabricated via selective laser melting. Mater Des 2014;55:533–41. https://doi.org/10.1016/j.matdes.2013.10.027.

[95] Xiao Z, Yang Y, Xiao R, Bai Y, Song C, Wang D. Evaluation of topology-optimized lattice structures manufactured via selective laser melting. Mater Des 2018;143:27–37. https://doi.org/10.1016/j.matdes.2018.01.023.

[96] Maconachie T, Leary M, Lozanovski B, Zhang X, Qian M, Faruque O, et al. SLM lattice structures: Properties, performance, applications and challenges. Mater Des 2019;183:108137. https://doi.org/10.1016/j.matdes.2019.108137.

[97] du Plessis A, Razavi N, Benedetti M, Murchio S, Leary M, Watson M, et al. Properties and applications of additively manufactured metallic cellular materials: A review. Prog Mater Sci 2022;125. https://doi.org/10.1016/j.pmatsci.2021.100918.

[98] Sing SL, Yeong WY, Wiria FE, Tay BY. Characterization of Titanium Lattice Structures Fabricated by Selective Laser Melting Using an Adapted Compressive Test Method. Exp Mech 2016;56:735–48. https://doi.org/10.1007/s11340-015-0117-y.

[99] Brenne F, Niendorf T, Maier HJ. Additively manufactured cellular structures: Impact of microstructure and local strains on the monotonic and cyclic behavior under uniaxial and bending load. J Mater Process Technol 2013;213:1558–64. https://doi.org/10.1016/j.jmatprotec.2013.03.013.

[100] Mines RAW, Tsopanos S, Shen Y, Hasan R, McKown ST. Drop weight impact behaviour of sandwich panels with metallic micro lattice cores. Int J Impact Eng 2013;60:120–32. https://doi.org/10.1016/j.ijimpeng.2013.04.007.

[101] Morlock M, Schneider E, Bluhm A, Vollmer M, Bergmann G, Uller D VM, et al. Duration and frequency of every day activities in total hip patients. vol. 34. 2001.

[102] Fiorentino A, Zarattini G, Pazzaglia U, Ceretti E. Hip prosthesis design. Market analysis, new perspectives and an innovative solution. Procedia CIRP, vol. 5, Elsevier B.V.; 2013, p. 310–4. https://doi.org/10.1016/j.procir.2013.01.061.

[103] Ginestra PS, Ceretti E, Fiorentino A. Potential of modeling and simulations of bioengineered devices: Endoprostheses, prostheses and orthoses. Proc Inst Mech Eng H 2016;230:607–38. https://doi.org/10.1177/0954411916643343.

[104] Limmahakhun S, Oloyede A, Chantarapanich N, Jiamwatthanachai P, Sitthiseripratip K, Xiao Y, et al. Alternative designs of load−sharing cobalt chromium graded femoral stems. Mater Today Commun 2017;12:1–10. https://doi.org/10.1016/j.mtcomm.2017.05.002.

[105] Min BM, Lee G, Kim SH, Nam YS, Lee TS, Park WH. Electrospinning of silk fibroin nanofibers and its effect on the adhesion and spreading of normal human keratinocytes and fibroblasts in vitro. Biomaterials 2004;25:1289–97. https://doi.org/10.1016/j.biomaterials.2003.08.045.

[106] Wauthle R, Van Der Stok J, Yavari SA, Van Humbeeck J, Kruth JP, Zadpoor AA, et al. Additively manufactured porous tantalum implants. Acta Biomater 2015;14:217–25. https://doi.org/10.1016/j.actbio.2014.12.003.

[107] Arabnejad S, Burnett Johnston R, Pura JA, Singh B, Tanzer M, Pasini D. High-strength porous biomaterials for bone replacement: A strategy to assess the interplay between cell morphology, mechanical properties, bone ingrowth and manufacturing constraints. Acta Biomater 2016;30:345–56. https://doi.org/10.1016/j.actbio.2015.10.048.

[108] Güden M, Alpkaya AT, Hamat BA, Hızlı B, Taşdemirci A, Tanrıkulu AA, et al. The quasi-static crush response of electron-beam-melt Ti6Al4V body-centred-cubic lattices: The effect of the number of cells, strut diameter and face sheet. Strain 2022;58:1–20. https://doi.org/10.1111/str.12411.

[109] Xiong Y, Wang W, Gao R, Zhang H, Dong L, Qin J, et al. Fatigue behavior and osseointegration of porous Ti-6Al-4V scaffolds with dense core for dental application. Mater Des 2020;195:108994. https://doi.org/10.1016/j.matdes.2020.108994.

[110] Fu J, Ding J, Qu S, Zhang L, Wang MY, Fu MW, et al. Improved light-weighting potential of SS316L triply periodic minimal surface shell lattices by micro laser powder bed fusion. Mater Des 2022;222. https://doi.org/10.1016/j.matdes.2022.111018.

[111] Khairallah SA, Martin AA, Lee JRI, Guss G, Calta NP, Hammons JA, et al. Controlling interdependent meso-nanosecond dynamics and defect generation in metal 3D printing. vol. 368. 2020.

[112] Tang M, Pistorius PC, Beuth JL. Prediction of lack-of-fusion porosity for powder bed fusion. Addit Manuf 2017;14:39–48. https://doi.org/10.1016/j.addma.2016.12.001.

[113] Vastola G, Pei QX, Zhang YW. Predictive model for porosity in powder-bed fusion additive manufacturing at high beam energy regime. Addit Manuf 2018;22:817–22. https://doi.org/10.1016/j.addma.2018.05.042.

[114] Sadeghi H, Bhate D, Abraham J, Magallanes J. QUASI-STATIC AND DYNAMIC BEHAVIOR OF ADDITIVELY MANUFACTURED METALLIC LATTICE CYLINDERS *. n.d.

[115] Li P, Wang Z, Petrinic N, Siviour CR. Deformation behaviour of stainless steel microlattice structures by selective laser melting. Materials Science and Engineering: A 2014;614:116–21. https://doi.org/10.1016/j.msea.2014.07.015.

[116] Ahmadi SM, Campoli G, Amin Yavari S, Sajadi B, Wauthle R, Schrooten J, et al. Mechanical behavior of regular open-cell porous biomaterials made of diamond lattice unit cells. J Mech Behav Biomed Mater 2014;34:106–15. https://doi.org/10.1016/j.jmbbm.2014.02.003.

Chapter 2
Co-Cr-Mo

In this chapter a biocompatible Co-Cr-Mo alloy was used. Three different types of elementary cell geometry were selected: Face Centered Cubic, Diagonal, and Diamond. These cells were applied to the radially graded porous lattice structures to evaluate the influence of their orientation in relation to the sample and the build platform. Moreover, heat treatment was carried out to study its influence on microstructural properties and mechanical behavior. Subsequently, modelling and FE simulations were carried out to predict their mechanical response. The results of numerical simulations were compared with experimental data.

The published papers related to the Co-Cr-Mo alloy are listed below:

- Cantaboni F, Ginestra PS, Tocci M, Avanzini A, Ceretti E, Pola A. Compressive behavior of Co-Cr-Mo radially graded porous structures under as-built and heat-treated conditions. Frattura Ed Integrita Strutturale 2022;16:490–504. https://doi.org/10.3221/IGF-ESIS.62.33.

- Cantaboni, F., Ginestra, P., Tocci, M., Colpani, A., Avanzini, A., Pola, A., & Ceretti, E. (2022). Modelling and FE simulation of 3D printed Co-Cr Lattice Structures for biomedical applications. Procedia CIRP, 110(C), 374–379. https://doi.org/10.1016/j.procir.2022.06.066.

2.1 Compressive behavior of Co-Cr-Mo radially graded porous structures under as-built and heat-treated conditions

2.1.1 Introduction

AM technologies have an important impact on the biomedical industry due to the enhanced possibilities of customizations for the production of bespoke implants [1–6]. Of particular interest for the metallic materials are the powder bed fusion (PBF) processes, which can be split into categories based on the utilized energy source or the binding mechanism, e.g. selective laser sintering (SLS) and selective laser melting (SLM) [4,7–11].

Various alloys can be processed using Laser Powder Bed Fusion (L-PBF) processes, such as stainless steel, titanium, and cobalt alloys [12–14]. Among these, Co-Cr alloys have good versatility and durability, together with biocompatibility [15]. In general, these alloys are used to produce surgical tools and prostheses such as hip and knee replacements due to their excellent wear and corrosion resistance [16,17]. For this application, the stress-shielding effect can occur, since the prostheses should have a similar stiffness to the bone, otherwise osteoporosis issues can arise [18]. While this could be a limitation for metallic alloys with high elastic modulus, such as Co-Cr, with additive manufacturing, the use of cellular configurations can help to overcome this problem.

AM process can manufacture complex structures, taking advantage of layer-by-layer production. In comparison with other processing routes, it has more flexibility, together with the possibility to manufacture near-net-shape components without the need of expensive molds [19]. The lattice structures can be printed, that are topologically ordered and organized in 3D space with repeating open cells [20]. These structures are defined by node and strut dimensions (usually in the order of micrometres), and cell 3D dimensions. The stiffness of lattice structures can be tailored to be comparable with the physiological tissue while keeping the strength and biocompatibility of the Co-Cr alloys [21].

Lattice structures are composed of strut-based cell topologies, the most common are Body-Centered Cubic (BCC) and Face Centered Cubic (FCC) [22]. Moreover, other types of strut-based topologies exist, such as octet-truss, cubic, diagonal, and diamond [23]. Strut-based topologies can be characterized by the Maxwell number, M, which is calculated from the number of struts and nodes [24]. This number is useful to understand if the structures will be mechanically bending-dominated or stretch-dominated [25].

Besides cell geometry, the mechanical response of a lattice structure also depends on the material microstructure. In this regard, an additional peculiar aspect of the L-PBF process is the extremely rapid solidification rate [15]. This influences the microstructure significantly, as already pointed out in the literature. In comparison with casting processes, the microstructure of Co-Cr alloy presents columnar grains growing in the building direction through the building layers, composed of fine cellular sub-grains [26].

Heat treatments may cause further modifications, providing the additional possibility to tune the lattice behavior according to the needs. In the literature [27], several heat treatments have been investigated to identify the effect

of temperature, time, and cooling rate on the Co-Cr alloy samples manufactured by L-PBF. Heat treatments have a big influence on the mechanical properties, due to the microstructural changes they may induce [14,28].

In the present study, Face Centered Cubic (FCC), Diagonal (DG), and Diamond (DM) cells were selected and radially distributed for the lattice design due to their differences in terms of expected mechanical properties and porosity. The lattice structures were designed to investigate how the radial arrangement can affect the mechanical properties of the samples. This specific configuration is particularly relevant for biomedical applications, because the radially graded porosity is similar to the porosity of the physiological structure of the cortical bone, especially at the interface with trabecular bone lamellae [29–32]. Moreover, biocompatible radially graded porous structures have already been demonstrated to promote and guide the repair of bone defects [33]. However, a few studies are available in the literature regarding the mechanical characterization of these structures produced using Co-Cr alloy [18].

This work aims to analyse and report the mechanical characterization of innovative Co-Cr-Mo radially graded porous samples manufactured by L-PBF. Furthermore, the lattice structures were built with different orientations (i.e., horizontal and vertical) as a promising design strategy for biomedical applications involving tissue repair guidance and porosity control.

2.1.2 Materials and methods

2.1.2.1 Sample production and post-processing

Lattice structures were designed by 3D XPert software, (ProX® DMP 100, 3D system, Rock Hill, South Carolina, USA). Six cylindrical lattice samples with a height of 30 mm and a diameter of 24 mm with a nominal volume (Vn) of 13565 mm3, were designed. The porosity was to be 50% or more, according to ISO 13314 standard, with three different unit cell geometry: Face Centered Cubic (FCC), Diamond (DM), and Diagonal (DG). The samples were produced with an orientation of 0° and 90° on the building plate (XY), as reported in Figure 1a. Moreover, Figure 1b shows the radial gradient directions of the cells in relation to the Z-axis. A lower density than the uniformly distributed lattice structures was expected.

The volume of the cellular unit was 2(X) x 2(Y) x 2(Z) mm³. Nodal joints are designed with a spherical shape, with a diameter of 1,0 mm while the cross-sections of lattice struts are designed circular in shape with a diameter of 0,5 mm. The software can automatically generate the correct number of cells based on the dimension and the volume boundaries where it will be generated, setting the radial gradient as shown in Figure 2.

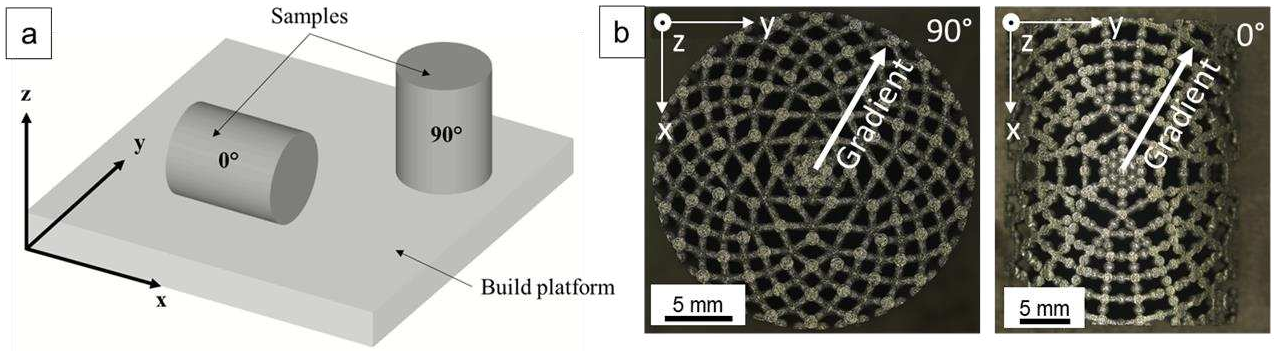

Figure 1: a) Orientations of the building samples on the building plate and b) the radial gradient direction of the cells.

The 90° and 0° radially graded porous lattices are reported in Figure 2a, 3c, 3e and Figure 2b, 3d, 3f, respectively. Therefore, the increasing gradient of porosity from the centre to the edges of samples can be tailored based on the orientation, as shown in Figure 2. The samples are named respectively FCC0, FCC90, DM0, DM90, DG0, and DG90 due to their orientation in relation to the building plate.

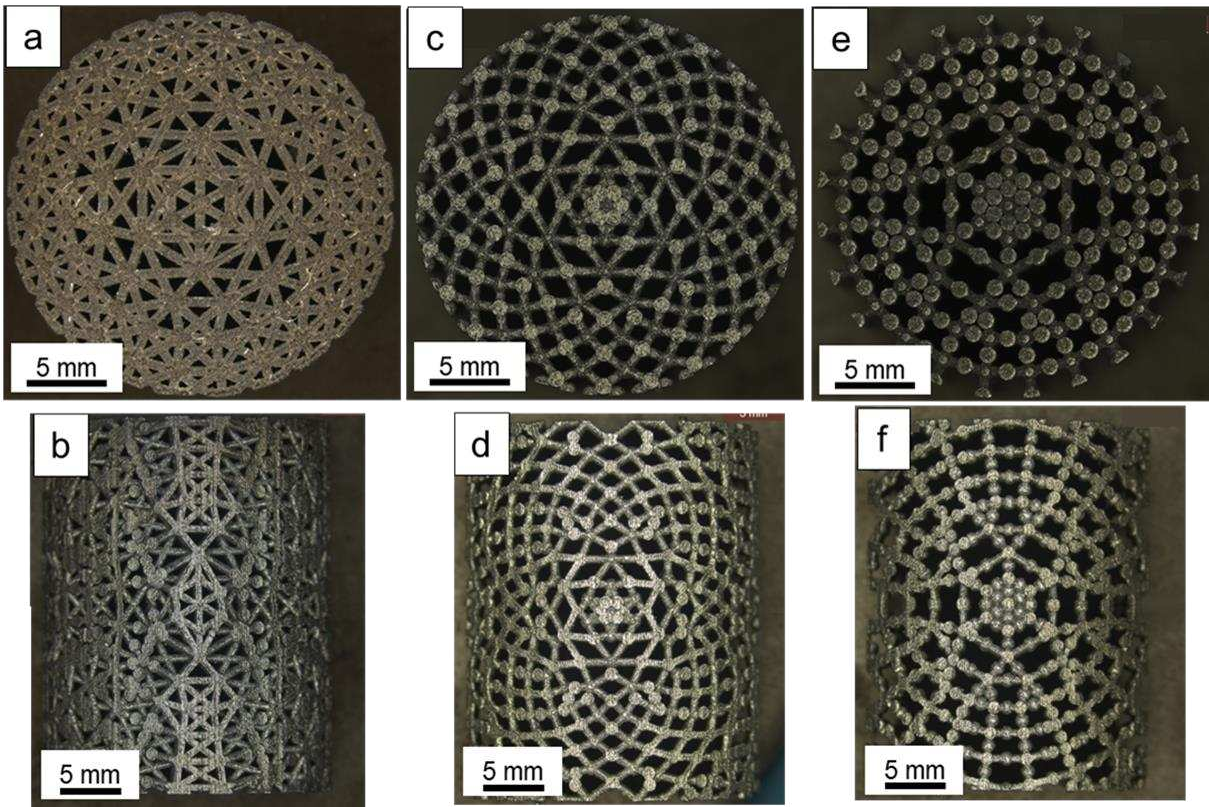

Figure 2: Radially graded porous lattice structures. Top view of: (a) FCC90, (c) DM90, (e) DG90 samples and side view of: (b) FCC0 (d) DM0, (f) DG0 samples.

Samples were manufactured using Co-Cr-Mo alloy powder produced by LaserForm®. The nominal chemical composition is reported in Table 1.

Co-Cr-Mo	Co	Cr	Mo	Ni	Fe	C	Si	Mn
Wt min (%)	Bal.	28.00	5.00	0.00	0.00	0.00	0.00	0.00
Wt max (%)		30.00	6.00	0.10	0.50	0.02	1.00	1.00

Table 1: Nominal chemical composition (wt%) of Co-Cr-Mo powders used for the production of samples.

The ProX® DMP 100 printer (3D system®, Wilsonville, Oregon, USA), was used for printing the lattices in a controlled nitrogen inert gas atmosphere (O2<0.01%) The printer process parameters were set as reported in Table 2:

Process Parameter	Value
Laser power [W]	50
Spot diameter [µm]	80
Scan speed [mm/s]	300
Hatch spacing [µm]	50
Layer thickness [µm]	30

Table 2: Process parameters used for the production of samples.

Supports were generated with the same process parameters as the lattice samples.

Where present, the supports for 90° samples were removed using a metallographic cutting machine. Then, the samples were grinded with sandpaper paying attention not to alter the lattice structure to assure the reliability of the mechanical tests.

Samples before and after heat treatment are named respectively as-built (AB) and heat-treated (HT) samples.

Heat treatment was performed using a horizontal furnace for vacuum heat treatment. The samples were heated from room temperature up to 1200 °C with a heating rate of 13°C/min and soaked at 1200°C for 2h. A partial pressure was applied as the temperature reached 650°C and upwards, while vacuum cooling was carried out. The aim was to relieve residual stresses and homogenize the microstructure [14].

2.1.2.2 Metallurgical, technological, and mechanical characterizations

The sample dimensions were collected to compare the designed model and produced samples. The diameter and height of the cylinders were experimentally measured with a Vernier caliper. The relative density was evaluated as the ratio between the total volume occupied by the material in relation to the geometry of the cell, based on the CAD file, and the total volume of the whole full cylinder [27].

The optical microscope (LEICA DMI 5000 M, Wetzlar, Germany) was used to investigate the microstructure of the samples. The as-built and heat-treated samples were mounted in acrylic resin, polished up to mirror finishing, and electrolytically etched (for 60 seconds in 5% HCl solution) to identify the main microstructural features. The software ImageJ (National Institutes of Health, USA) was used to measure the size of melting pools and laser scan tracks.

Moreover, Vickers microhardness measurements were performed with a Mitutoyo HM-200 (Mitutoyo Corporation, Kawasaki (Kanagawa), Japan) hardness testing machine to evaluate the effectiveness of the heat treatment. A load of 0.5 kg was applied for 15 s. Ten repetitions for each AB and HT sample were performed on the supports.

Compressions tests were carried out with a servo-hydraulic testing machine INSTRON 8501 (Instron, Norwood, MA, USA) equipped with a 500 kN load cell. Tests were conducted in displacement control at a constant crosshead velocity of 2 mm/min and the displacement was measured using the crosshead movement.

Load-displacement curves were generated from Instron output data. Maximum compressive strength (ultimate strength), quasi-elastic gradient, plateau stress between 20% to 40% strain, and compressive offset stress at the plastic compressive strain of 0.2 % (yield stress), were calculated according to ISO 13314:2011 standard. Ultimate strength was detected as the maximum stress, the quasi-elastic gradient was calculated considering the linear trend of the elastic field, and the yield stress was calculated with a 0.2% deviation of the quasi-elastic trend line. Plateau stress was calculated for bending-dominated samples as the average value of stress corresponding to the compressive strain from 20% to 40%, according to ISO 13314:2011. This is because their plateau was extended at higher values of strain, in contrast with stretch-dominated samples, which present lower values of strain. The plateau stress was necessary to understand the behavior of the material and whether the response of the lattice was bending-dominated or stretch-dominated.

Furthermore, fracture surfaces of samples were analyzed by scanning electron microscope (SEM), LEO EVO® 40 (Carl Zeiss AG, Italy), to investigate the fracture mechanism.

2.1.3 Results and discussions

2.1.3.1 Lattice structure

A diameter of 24.1±0.1 mm was measured for the samples. Instead, a height of 30.3±0.1 mm was detected for the 0° samples in contrast with the 90° ones which resulted in a height of 28.6±0.5 mm, due to the support removal of the samples.

Moreover, the relative density was evaluated as a relevant parameter to determine the mechanical properties [1]. In Table 3 the relative density of the samples is reported, where VL is the volume of the designed samples and Vn (nominal volume) is 13565 mm3. The density changes with the kind of cells. The FCC configuration exhibits the highest density, due to the higher number of struts in its configuration.

Sample	Building angle [°]	VL [mm3]	Relative density [%]
FCC	0	6040	45
	90	5480	40
DM	0	3100	23
	90	3160	23
DG	0	2690	20
	90	2890	21

Table 3: Relative density of AB samples.

It is worth mentioning that partially melted powder may be trapped inside the samples due to their complex geometry, at the expense of mechanical behavior and relative density estimation [19,34].

2.1.3.2 Microstructure

Micrographs of the longitudinal (L) and transverse (T) cross-section of the 90° samples are shown in Figure 3a and Figure 3b. The microstructure of the 0° samples is not reported since they are characterized by the same features. The typical overlapped melt pools are shown in Figure 3a on the L cross-section. They are caused by the melting powders under the focused laser energy. Instead, along the T cross-section, the elongated scan tracks are visible, revealing the pattern followed by the laser during the manufacturing process (Figure 3b).

The dimension of melt pools was estimated along the L-section as reported in the literature [35]. The melt pools are semi-circular in shape and their dimension was compared with the laser beam diameter and layer thickness. The width and depth of melt pools range from 60 to 70 µm and from 30 to 35 µm, respectively. The average width is lower than the laser beam diameter, instead, the average depth is comparable with the layer thickness. This is due to the low value of laser power of 50W because it has been demonstrated that this parameter plays an important role in determining the size and geometry of melt pools, i.e. higher laser power leads to deeper melt pools [36,37].

Porosity defects typical of L-PBF components, such as spherical porosities due to trapped gas [38] or lack-of-fusion porosities, are also visible in Figure 3a, and Figure 3b.

In Figure 3c and Figure 3d, an extremely fine cellular sub-structure limited by melt pools boundary inside certain melt pools is visible. This metastable cellular microstructure is a peculiarity of the L-PBF technology, due to the extremely rapid solidification [39], and it is common for various alloys [40]. Unlike most metallic materials, for Co-Cr-Mo alloys, the cell boundaries can be distinguished due to the segregation of Mo and Cr, which surrounds the Co-Cr matrix, and not due to the presence of secondary phases, as recently reported in [40]. The cells are oriented in different directions inside the same melt pool, as highlighted from the arrows in Figure 3d, individuating different sub-grains that grow from the grain boundary following a preferential crystallographic

orientation for Co-Cr alloy [39,40]. Since the grain growth is competitive, when they collide, one of them stops [41].

In addition, the micrographs reported in Figure 3c and Figure 3d show also examples of sintered particles and spatter, typical defects of components produced by L-PBF, usually characterized by poor surface finish in as-built conditions. In particular, the particle presented in Figure 3d is characterized by a dendritic structure, indicating a solidification condition very different from the bulk material.

Regarding the grain structure, it is also well reported in the literature [32,42] that epitaxial columnar grains grow along the highest temperature gradient [43].

In contrast with AB samples, HT samples show a completely different microstructure, as reported in Figure 3e. It clearly shows the disappearance of melt pools and the presence of equiaxed grains highlighted by the presence of precipitates along the grain boundaries. These are also dispersed in the matrix, as visible in Figure 3f at higher magnification.

Various phenomena take place during heat treatment. During soaking at 1200 °C, the fine cellular structure is progressively fragmented and dissolved, leading to a more homogeneous distribution of solute atoms and the formation of precipitates [44]. The chemical composition of these particles is still a topic of discussion and further investigations are needed. A strong dependence on the chemical composition of the alloy is evident from the literature [40] and carbide particles [45] or Cr- and Mo-rich particles are identified according to the C level in the considered alloy [40]. In the present study, the extremely low content of C (0.02 wt. %) suggests that precipitates are mainly particles containing Cr and Mo rather than carbides. This is consistent with a recent study [40] where a deep investigation of the evolution of microstructure during heat treatment is carried out.

Recrystallization also occurs, promoted by the high density of dislocations and residual stresses present in AB conditions, and resulting in coarse equiaxed grains after heat treatment (Figure 3e and 3f). This is also discussed by [40,46–48].

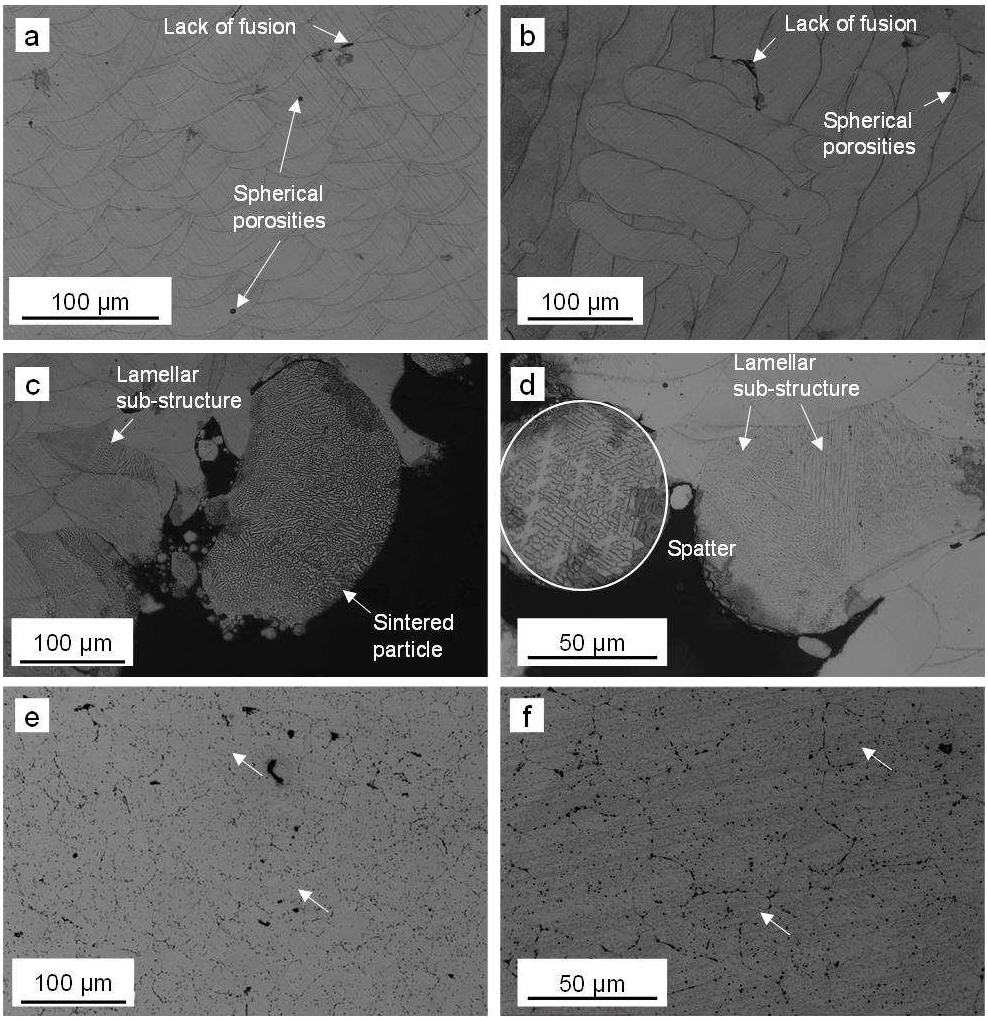

Figure 3: Optical micrographs of longitudinal (a) and transverse (b) cross-sections of AB samples built at 90°. Examples of sintered particles, cellular sub-structure (c), spatter, and lamellar sub-structure (d). Optical micrograph of HT sample (e) and HT sample at higher magnification (f) built at 90° (some examples of equiaxed grains marked by white arrows).

2.1.3.3 Micro hardness

The hardness of AB samples built at 0° is 431 ± 9 HV and at 90° is 423 ± 11 HV, which is 24% and 29% higher compared to the hardness of the treated ones, 321 ± 10 HV and 318 ± 8 HV, respectively. A decrease of hardness in HT samples was observed. This is due to the microstructural change already discussed. In particular, the dissolution of the cellular structure and the recrystallization are mainly responsible for different strengthening mechanisms acting in the HT samples as compared to the AB ones, leading to the observed lower hardness. The effect of the building direction is negligible in HT ones. These results are supported by the literature [44,47–49].

2.1.3.4 Compressive properties of radially graded lattice structures

The stress-strain curves recorded during compression tests are shown in Figure 4 where the corresponding cell morphology is indicated. The different behavior of the samples is noticeable in the different shapes of the curves reported in Figure 4.

The test was considered completed when the samples started to collapse after bending to the ultimate strength value. From the graphs it is also possible to identify which samples are bending-dominated or stretch-dominated, following the Gibson Ashby law [20], considering that in stretch-dominated behavior the stress value is higher at a lower strain value.

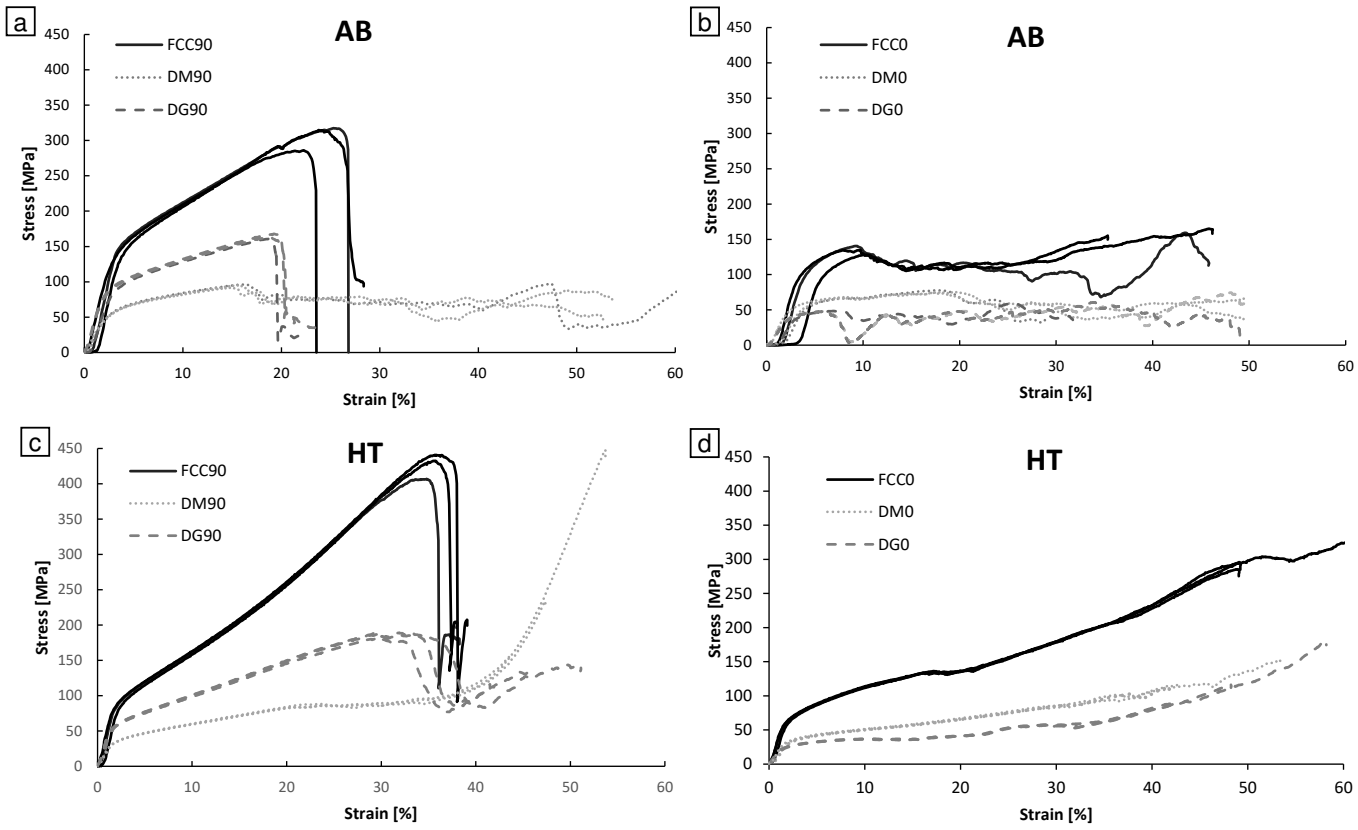

Figure 4: Stress-strain curves of: AB samples with: (a) FCC90, DM90, DG90 and (b) FCC0, DM0, DG0 (3 repetitions for each ones). HT samples with: (c) FCC90, DM90, DG90 and (d) FCC0, DM0, DG0 (3 repetitions for each ones).

For the 90° samples, the curves in Figure 4a suggest that FCC90 and DG90 unit cells exhibit stretch-dominated behavior. In particular, the samples crashed at 306 ± 17 MPa at 25% of strain for FCC90 cells and 164 ± 4 MPa at 20% strain for DG90 cells. The curves of DM90 samples are instead characterized by bending-dominated behavior since they exhibit a more uniform trend, lower stress values, and deform more easily. The DM90 ultimate strength is 95 ± 3 MPa at 17% strain, followed by a decrease due to the collapse of the structure. Since strength is correlated with density, a higher value was expected for the DM cells samples in comparison with DG samples, due to the slightly lower relative density of unit DG cells than the samples with DM cells [50]. The observed behavior could be caused by the radial orientation of cells as mentioned before. As expected, the samples with FCC cells, which featured the highest relative density, also exhibited the highest strength. In fact, for FCC AB samples the ultimate strength is 57% higher than for the DM and DG samples.

The stress-strain in Figure 4b shows that DG0 unit cells exhibit stretch-dominated behavior which is crashed at 65 ± 9 MPa at 35% strain, while bending-dominated is typical for DM0 and FCC0 cells arrangement. These lasts crashed at 76 ± 2 MPa at 42% strain and 160 ± 5MPa at 18% strain, respectively.

Considering the influence of building orientation, for the AB specimens characterized by a stretch-dominated behavior, the resistance to compressive load is higher in the specimens built at 90° and on the contrary, the samples built at 0° can reach higher deformation. In fact, in Figure 4b, it is possible to see that the 0° samples show a continuous increase in strain over 30% whereas, for the 90° ones (Figure 4a), the strain at failure is in the order of 25%. These differences depend on the relation between struts orientation and load direction, the lattice configuration with higher strength and lower elongation at failure are those in which the unit cell has more struts oriented along the load direction.

For the samples characterized by bending-dominated behavior, represented by DM cell configuration, the effects mentioned above for the stretch-dominated behavior, are less marked, because neither in 0° samples nor in 90° ones the cells are oriented along the load direction.

Furthermore, the HT samples were investigated to confirm the AB results. They have a different mechanical response as shown in Figure 4c and Figure 4d. In general, they reach higher deformations than the AB samples. As shown in Figure 4c, FCC90 samples collapsed at 427 ± 18 MPa at 35% strain and DG90 specimens at 185 ± 4 MPa at 30% strain, while the deformation of DM samples continued to increase over 40% strain, and they did not present a collapse point. FCC heat-treated samples showed an ultimate stress value 58% higher than DM and DG samples, due to the density of the structure geometries.

The DM and FCC samples built at 0° are the only ones having a bending-dominated behaviour and therefore a plateau-stress is reached. The plateau stress values of DM samples built at 0° and 90° were 75 MPa and 59 MPa, respectively, while for the FCC sample built at 0° was 112 MPa. In contrast with AB samples, the HT specimens do not present any plateau zone, because all of them are characterized by stretch-dominated behaviour, probably due to the transformation of the microstructure, which gives lower resistance, but higher isotropy and ductility. Additionally, in Figure 5a and Figure 5b, a summary of results of quasi-elastic gradient and yield stress is reported.

The quasi-elastic gradient reported in Figure 5a clearly shows that the influence of the building angle is almost negligible for FCC and DM structures. Regarding the DG samples, the values display a more pronounced deviation. Probably due to the building angle and the strut's distribution influence their stiffness. The DG samples exhibit different properties built at 0° and 90°.

The stiffness of AB and HT samples are similar, and their values differ by a maximum of 20%.

As shown in Figure 5b, the build angle does not significantly affect the yield stress, as indicated for the quasi-elastic gradient analysis. The exception is still for the DG samples. Moreover, the heat treatment is extremely relevant, because the yield stress values remarkably decrease after the treatment, as shown in Figure 5b. When the samples are heat-treated, the linear elastic zone is less wide compared with the AB samples. This is probably due to the homogenization and coarsening of the microstructure during heat treatment.

Both stiffness and strength data show an increase in accordance with the density, as expected.

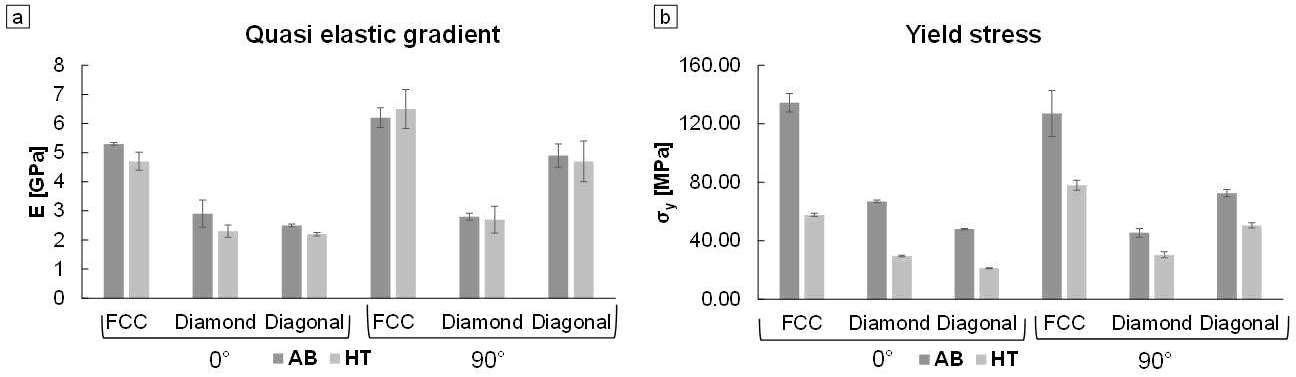

Figure 5: Average values with a standard deviation of quasi-elastic gradient (a) and yield stress (b) of the AB and HT samples.

The energy absorption data are reported in Figure 6. After the heat treatment, it growths for all the samples independently from the cell morphology. This means that that the samples are able to reach higher deformation and therefore to absorb more energy when stressed.

This behavior is consistent with the decrease in hardness recorded after heat treatment and appears interesting for applications in the biomedical fields, such as for surgical implants and tools [2,50].

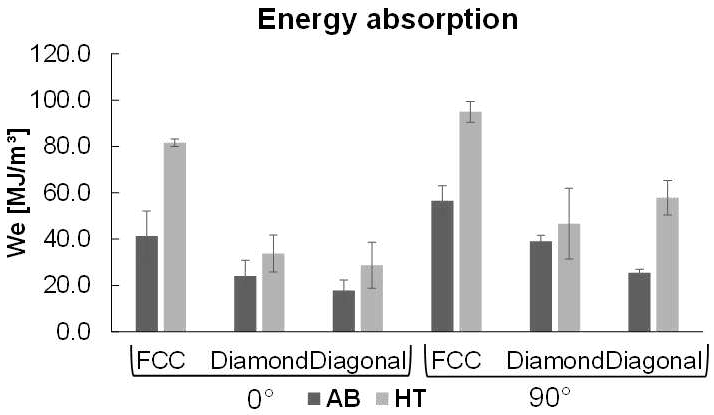

Figure 6: Energy absorption values of the samples.

The reported mechanical performance is in accordance with the literature [18,32,49,51-53]. In particular, the results obtained were compared with the literature to identify the main differences between the radially graded porous structure and uniformly distributed ones. The mechanical properties such as ultimate strength, yield stress, hardness, and energy absorption presented similar values for each configuration of the cell [1], [32], [37,53–55]. Instead, the radial arrangements give the lattices a stiffness homogenization along the planes perpendicular to the symmetry axis, contrary to the non-radially graded lattices, which are characterized by anisotropic stiffness [56,57].

2.1.3.5 Failure modes and Fracture analysis

The compression tests were ended after the first major structural collapse, usually signified by the fracture of the specimen into multiple pieces. Otherwise, they were terminated when the sample reached the strain of 50%-60%.

Some examples of specimen failure, representative of the analyzed AB samples, are reported in Figure 7.

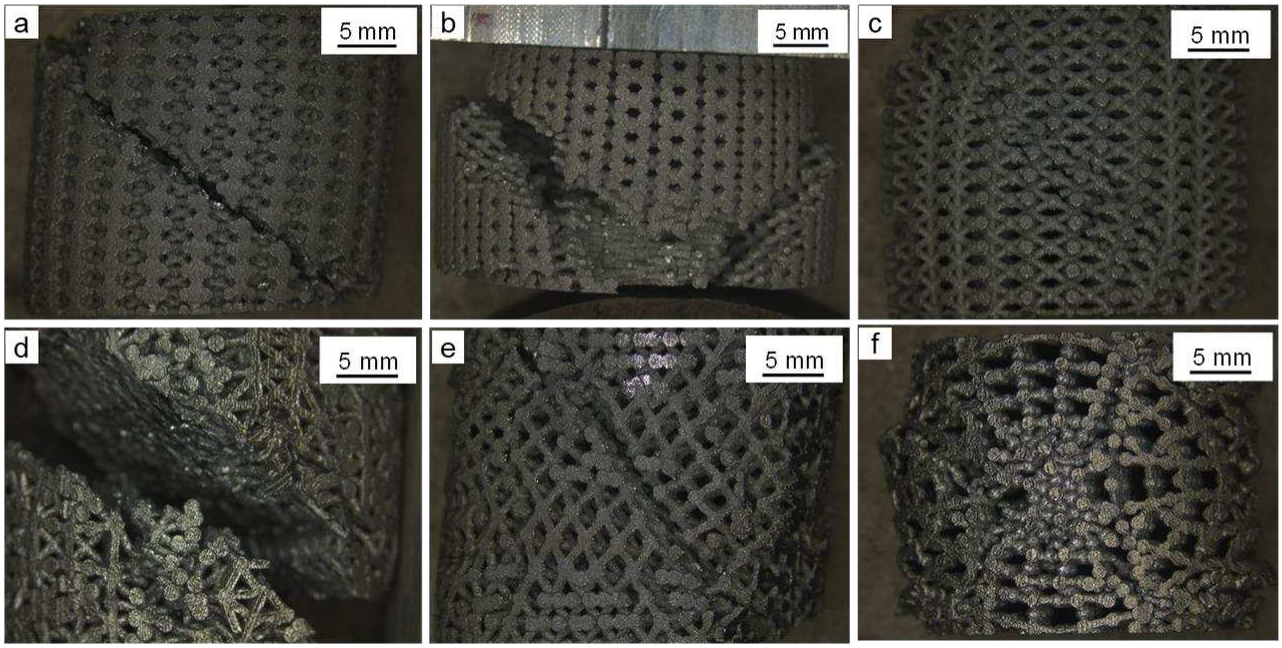

Figure 7: Main failure modes after compression test on AB sample: a) FCC90, b) DM90, c) DG90, d) FCC0, e) DM0 and f) DG0.

Most of the specimens showed the presence of an inclined plane along which final failure occurred, although with some differences. For FCC90 and DG90 (Figure 7a and Figure 7c) failure was almost simultaneous along with layers at different heights and, as shown in Fig. 5a, no plateau was observed. For DM90, FCC0 and DM0 (Figure 7b, Figure 7d, and Figure 7e) failure were more progressive and a plateau with small fluctuation was present (see Figure 4a and Figure 4b). On the contrary, DG0 samples (Figure 7f) progressively crashed layer after layer and the plateau showed more evident fluctuations (Figure 4b), suggesting a brittle nature of the failure mechanism.

Some examples of heat-treated specimen failure, representative of all the analyzed ones is reported in Figure 8, again with the presence of different failure modes. In particular, while the FCC90 and the DG90 (Figure 8a and Figure 8c) failed similarly to the AB condition and the stress-strain behavior is of the same type (Figure 4c), the DM90 (Figure 8b) progressively crushed with a more extended and flatter plateau and very limited stress fluctuations.

A similar response was observed (Figure 4d) for FCC0 (Figure 8d), with some discontinuities related to sudden local failures, and for DM0 and DG0 (Figure 8e and Figure 8f). For this latter condition, by comparison with AB, a damping effect due to the increased ductility related to HT can be appreciated.

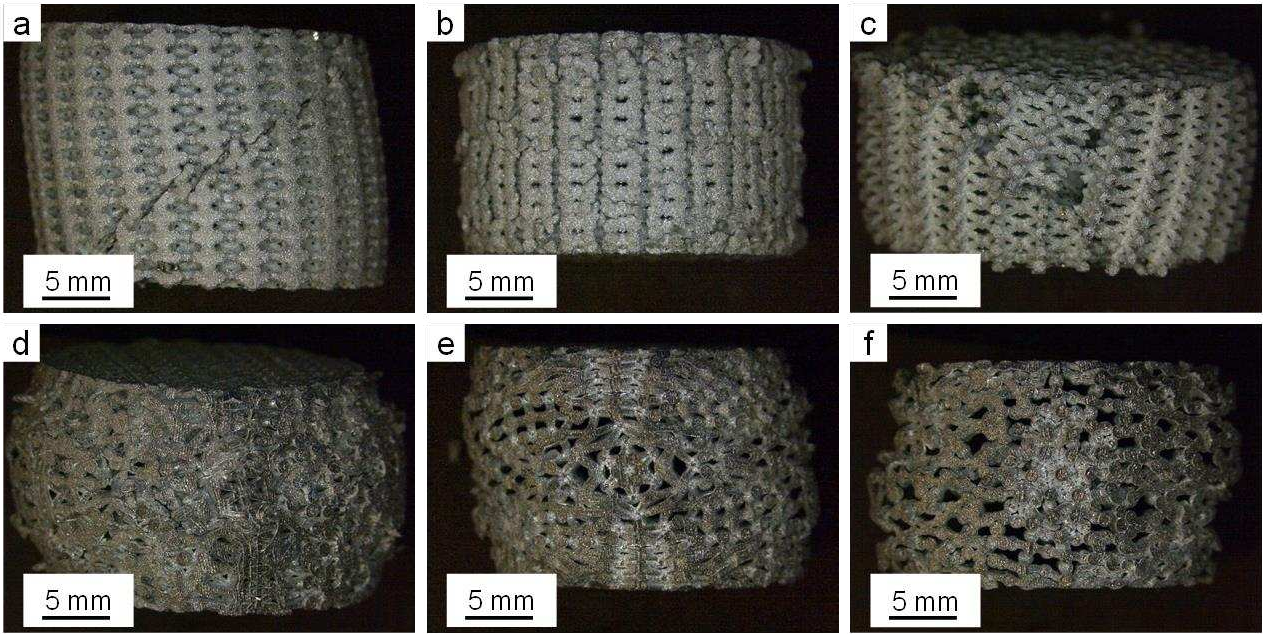

Figure 8: Main failure modes after compression test on HT samples: (a) FCC90, (b) DM90, c) DG90, d) FCC0, e) DM0 and f) DG0.

Overall, the different failure modes observed at the macroscopical level agree with the literature confirming that by exploiting different combinations of lattice cell configurations, orientation, and post-treatments a variety of deformation behaviors can be achieved. The change of the failure mode through the heat treatment can be shown in other metals [22,58,59].

Representative SEM images of the fracture surface of the AB samples are shown in Figure 9a, Figure 9b, and Figure 9c. Images related only to FCC and DG samples are shown since no different role of the microstructure was identified changing the design of the geometry of the lattice.

At low magnification (Figure 9a), details indicating a quasi-cleavage mechanism can be observed, as flat areas with parallel markings. Terrace-like steps were also presents where the fracture is crossing grain boundaries, probably due to the presence of defects that guide the fracture propagation. Similar features in terms of fracture behavior were also found in the literature [43,44] for samples after tensile tests, such as terrace-like steps and cleavage facets.

Additional features can be identified by observing the specimen at higher magnification (Figure 9b, Figure 9c). For instance, the elongated markings indicated by arrows in Figure 9b resemble the elongated cellular structure visible in the melt pools suggesting that these can influence the direction of fracture propagation. Similarly, according to the fracture propagation, the cell structure can be crossed in a normal direction. In this case, instead

of elongated markings, a dimple-like structure may be detected, as in Figure 9c. The size of these dimples is comparable with the cell spacing of the samples (Figure 3) and this is also confirmed by the literature [46,58]. In contrast, larger areas that exhibit ductile fracture are visible in HT sample [60], as shown in Figure 9d. Coarser dimples than in AB samples are present probably due to the loss of extra-fine microstructure after heat treatment (Figure 9e). Moreover, the presence of fine particles at the center of the dimples is shown in Figure 9f. These fine particles are detected only in the HT samples, and they are associated with the formation of coarse precipitates during heat treatment, as visible in Figure 3e.

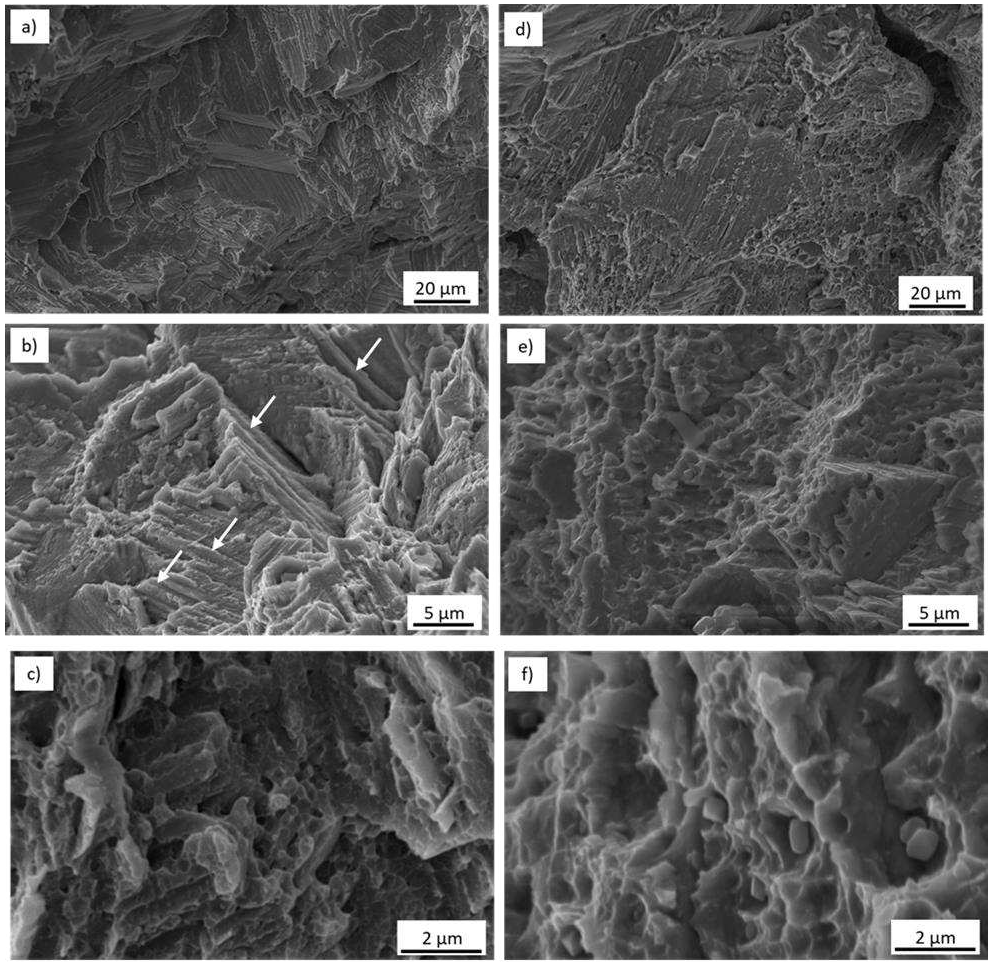

Figure 8: Representative SEM images of fracture mechanism of AB samples (a), (b), (c), and HT samples (d), (e), (f).

2.1.4 Conclusions

The main aim of this work was to analyse the compression behavior of Co-Cr-Mo radially graded lattice structure, manufactured by L-PBF aimed to biomedical applications. Different lattice configurations printed at 0° and 90° build angles were considered to investigate the variation in sample properties due to the different orientations of the struts of FCC, DM and DG cells with a radial gradient direction. Moreover, the samples were heat-treated to study the consequent evolution of the mechanical properties.

Based on the experimental results and discussion, it can be concluded that:

- The building orientation resulted an important parameter affecting the mechanical response of the structures. In fact, for the AB samples, the ultimate stress of 90° samples is higher than for the 0° ones. In particular, the ultimate stress of FCC, DM, and DG samples built at 90° is 48%, 20%, and 61% higher than for those built at 0°, respectively. Both stiffness and strength showed a growing trend with the increase in density, where FCC showed the highest value.
- For all three geometries, the radially graded porous structures exhibited different mechanical properties according to the orientation at 0° or 90° of the samples. The 0° specimens showed a continuous increase in strain over 30% while, for the 90° ones, at 25% strain the structure collapsed. These differences depend on the relationship between struts orientation and load direction. In particular, the lattice configuration with higher strength and lower elongation at failure are those in which the unit cell has more struts oriented along the load direction.
- In general, the HT samples exhibited a more ductile behavior since a decrease in stiffness and hardness of the samples was recorded. This is consistent with the mainly ductile fracture behavior detected from the analysis of fracture surfaces, while AB structures exhibited features of a quasi-cleavage mechanism.

The possibility to produce radially graded lattice structures was demonstrated. Moreover, it was shown how the mechanical properties are affected by cell geometry and orientation in combination with heat treatment. The obtained results give further insight into the possibility to tailor the mechanical properties of lattice structures according to a specific selected application. Therefore, the achieved results can open novel solutions for the proper repair of local defects within the bone and the acceleration of the regeneration of the physiological tissue due to the combination of mechanical and morphological stimuli. Additionally, the proposed configurations could represent an optimal solution to produce customized metal implants.

References

[1] Riva, L., Ginestra, P.S., Ceretti, E. (2021). Mechanical characterization and properties of laser-based powder bed–fused lattice structures: a review, Int. J. Adv. Manuf. Technol., 113(3–4), pp. 649–71, Doi: 10.1007/s00170-021-06631-4.

[2] Buj-Corral, I., Tejo-Otero, A., Fenollosa-Artés, F. (2020). Development of am technologies for metals in the sector of medical implants, Metals (Basel)., 10(5), pp. 1–30, Doi: 10.3390/met10050686.

[3] Johnson, N.S., Vulimiri, P.S., To, A.C., Zhang, X., Brice, C.A., Kappes, B.B., Stebner, A.P. (2020). Invited review: Machine learning for materials developments in metals additive manufacturing, Addit. Manuf., 36, Doi: 10.1016/j.addma.2020.101641.

[4] Wang, C., Tan, X.P., Tor, S.B., Lim, C.S. (2020). Machine learning in additive manufacturing: State-of-the-art and perspectives, Addit. Manuf., 36(August), pp. 101538, Doi: 10.1016/j.addma.2020.101538.

[5] Ginestra, P., Ferraro, R.M., Zohar-Hauber, K., Abeni, A., Giliani, S., Ceretti, E. (2020). Selective laser melting and electron beam melting of Ti6Al4V for orthopedic applications: A comparative study on the applied building direction, Materials (Basel)., 13(23), pp. 1–23, Doi: 10.3390/ma13235584.

[6] Ginestra, P., Ceretti, E., Lobo, D., Lowther, M., Cruchley, S., Kuehne, S., Villapun, V., Cox, S., Grover, L., Shepherd, D., Attallah, M., Addison, O., Webber, M. (2020). Post processing of 3D printed metal scaffolds: A preliminary study of antimicrobial efficiency, Procedia Manuf., 47(2019), pp. 1106–12, Doi: 10.1016/j.promfg.2020.04.126.

[7] Sing, S.L., An, J., Yeong, W.Y., Wiria, F.E. (2016). Laser and electron-beam powder-bed additive manufacturing of metallic implants: A review on processes, materials and designs, J. Orthop. Res., 34(3), pp. 369–85, Doi: 10.1002/jor.23075.

[8] Gu, D.D., Meiners, W., Wissenbach, K., Poprawe, R. (2012). Laser additive manufacturing of metallic components: Materials, processes and mechanisms, Int. Mater. Rev., 57(3), pp. 133–64, Doi: 10.1179/1743280411Y.0000000014.

[9] Murr, L.E., Quinones, S.A., Gaytan, S.M., Lopez, M.I., Rodela, A., Martinez, E.Y., Hernandez, D.H., Martinez, E., Medina, F., Wicker, R.B. (2009). Microstructure and mechanical behavior of Ti-6Al-4V produced by rapid-layer manufacturing, for biomedical applications, J. Mech. Behav. Biomed. Mater., 2(1), pp. 20–32, Doi: 10.1016/j.jmbbm.2008.05.004.

[10] Murr, L.E., Esquivel, E. V., Quinones, S.A., Gaytan, S.M., Lopez, M.I., Martinez, E.Y., Medina, F., Hernandez, D.H., Martinez, E., Martinez, J.L., Stafford, S.W., Brown, D.K., Hoppe, T., Meyers, W., Lindhe, U., Wicker, R.B. (2009). Microstructures and mechanical properties of electron beam-rapid manufactured Ti-6Al-4V biomedical prototypes compared to wrought Ti-6Al-4V, Mater. Charact., 60(2), pp. 96–105, Doi: 10.1016/j.matchar.2008.07.006.

[11] Mazzoli, A. (2013). Selective laser sintering in biomedical engineering, Med. Biol. Eng. Comput., 51(3), pp. 245–56, Doi: 10.1007/s11517-012-1001-x.

[12] Ginestra, P.S., Riva, L., Allegri, G., Giorleo, L., Attanasio, A., Ceretti, E. (2020). Analysis of 3D printed 17-4 PH stainless steel lattice structures with radially oriented cells, Ind. 4.0 – Shap. Futur. Digit. World, , pp. 136–41, Doi: 10.1201/9780367823085-25.

[13] Bayat, M., Thanki, A., Mohanty, S., Witvrouw, A., Yang, S., Thorborg, J., Tiedje, N.S., Hattel, J.H. (2019). Keyhole-induced porosities in Laser-based Powder Bed Fusion (L-PBF) of Ti6Al4V: High-fidelity modelling and experimental validation, Addit. Manuf., 30(August), pp. 100835, Doi: 10.1016/j.addma.2019.100835.

[14] Razavi, S.M.J., Avanzini, A., Cornacchia, G., Giorleo, L., Berto, F. (2021). Effect of heat treatment on fatigue behavior of as-built notched Co-Cr-Mo parts produced by Selective Laser Melting, Int. J. Fatigue, 142(September 2020), pp. 105926, Doi: 10.1016/j.ijfatigue.2020.105926.

[15] Wang, J.H., Ren, J., Liu, W., Wu, X.Y., Gao, M.X., Bai, P.K. (2018). Effect of selective laser melting process parameters on microstructure and properties of co-cr alloy, Materials (Basel)., 11(9), Doi: 10.3390/ma11091546.

[16] Gupta, S.K., Shahidsha, N., Bahl, S., Kedaria, D., Singamneni, S., Yarlagadda, P.K.D.V., Suwas, S., Chatterjee, K. (2021). Enhanced biomechanical performance of additively manufactured Ti-6Al-4V bone plates, J. Mech. Behav. Biomed. Mater., 119(March), pp. 104552, Doi: 10.1016/j.jmbbm.2021.104552.

[17] Henriques, B., Bagheri, A., Gasik, M., Souza, J.C.M., Carvalho, O., Silva, F.S., Nascimento, R.M. (2015). Mechanical properties of hot pressed CoCrMo alloy compacts for biomedical applications, Mater. Des., 83, pp. 829–34, Doi: 10.1016/j.matdes.2015.06.069.

[18] Limmahakhun, S., Oloyede, A., Sitthiseripratip, K., Xiao, Y., Yan, C. (2017). Stiffness and strength tailoring of cobalt chromium graded cellular structures for stress-shielding reduction, Mater. Des., 114, pp. 633–41, Doi: 10.1016/j.matdes.2016.11.090.

[19] Jin, N., Yan, Z., Wang, Y., Cheng, H., Zhang, H. (2021). Effects of heat treatment on microstructure and mechanical properties of selective laser melted Ti-6Al-4V lattice materials, Int. J. Mech. Sci., 190(July 2020), pp. 106042, Doi: 10.1016/j.ijmecsci.2020.106042.

[20] Maconachie, T., Leary, M., Lozanovski, B., Zhang, X., Qian, M., Faruque, O., Brandt, M. (2019). SLM lattice structures: Properties, performance, applications and challenges, Mater. Des., 183, pp. 108137, Doi: 10.1016/j.matdes.2019.108137.

[21] Liverani, E., Rogati, G., Pagani, S., Brogini, S., Fortunato, A., Caravaggi, P. (2021). Mechanical interaction between additive-manufactured metal lattice structures and bone in compression: implications for stress shielding of orthopaedic implants, J. Mech. Behav. Biomed. Mater., 121(March), pp. 104608, Doi: 10.1016/j.jmbbm.2021.104608.

[22] Maskery, I., Aboulkhair, N.T., Aremu, A.O., Tuck, C.J., Ashcroft, I.A. (2017). Compressive failure modes and energy absorption in additively manufactured double gyroid lattices, Addit. Manuf., 16, pp. 24–9, Doi: 10.1016/j.addma.2017.04.003.

[23] Amin Yavari, S., Ahmadi, S.M., Wauthle, R., Pouran, B., Schrooten, J., Weinans, H., Zadpoor, A.A. (2015). Relationship between unit cell type and porosity and the fatigue behavior of selective laser melted meta-biomaterials, J. Mech. Behav. Biomed. Mater., 43, pp. 91–100, Doi: 10.1016/j.jmbbm.2014.12.015.

[24] Abdelhamid, M., Czekanski, A. (2018). Impact of the lattice angle on the effective properties of the octet-truss lattice structure, J. Eng. Mater. Technol. Trans. ASME, 140(4), pp. 1747–69, Doi: 10.1115/1.4040409.

[25] Leary, M., Mazur, M., Williams, H., Yang, E., Alghamdi, A., Lozanovski, B., Zhang, X., Shidid, D., Farahbod-Sternahl, L., Witt, G., Kelbassa, I., Choong, P., Qian, M., Brandt, M. (2018). Inconel 625 lattice structures manufactured by selective laser melting (SLM): Mechanical properties, deformation and failure modes, Mater. Des., 157, pp. 179–99, Doi: 10.1016/j.matdes.2018.06.010.

[26] Anantharaj, S., Kundu, S., Noda, S. (2020). Ur n al Pr, Nano Energy, , pp. 105514, Doi: 10.1016/j.addma.2021.102025.

[27] Alomar, Z., Concli, F. (2020). A Review of the Selective Laser Melting Lattice Structures and Their Numerical Models, Adv. Eng. Mater., 22(12), pp. 1–17, Doi: 10.1002/adem.202000611.

[28] Guoqing, Z., Junxin, L., Xiaoyu, Z., Jin, L., Anmin, W. (2018). Effect of Heat Treatment on the Properties of CoCrMo Alloy Manufactured by Selective Laser Melting, J. Mater. Eng. Perform., 27(5), pp. 2281–7, Doi: 10.1007/s11665-018-3351-5.

[29] Alabort, E., Barba, D., Reed, R.C. (2019). Design of metallic bone by additive manufacturing, Scr. Mater., 164(April), pp. 110–4, Doi: 10.1016/j.scriptamat.2019.01.022.

[30] Di Luca, A., Longoni, A., Criscenti, G., Mota, C., Van Blitterswijk, C., Moroni, L. (2016). Toward mimicking the bone structure: Design of novel hierarchical scaffolds with a tailored radial porosity gradient, Biofabrication, 8(4), Doi: 10.1088/1758-5090/8/4/045007.

[31] Barba, D., Alabort, E., Reed, R.C. (2019). Synthetic bone: Design by additive manufacturing, Acta Biomater., 97, pp. 637–56, Doi: 10.1016/j.actbio.2019.07.049.

[32] Caravaggi, P., Liverani, E., Leardini, A., Fortunato, A., Belvedere, C., Baruffaldi, F., Fini, M., Parrilli, A., Mattioli-Belmonte, M., Tomesani, L., Pagani, S. (2019). CoCr porous scaffolds manufactured via selective laser melting in orthopedics: Topographical, mechanical, and biological characterization, J. Biomed. Mater. Res. - Part B Appl. Biomater., 107(7), pp. 2343–53, Doi: 10.1002/jbm.b.34328.

[33] Xie, J., MacEwan, M.R., Ray, W.Z., Liu, W., Siewe, D.Y., Xia, Y. (2010). Radially aligned, electrospun nanofibers as dural substitutes for wound closure and tissue regeneration applications, ACS Nano, 4(9), pp. 5027–36, Doi: 10.1021/nn101554u.

[34] Mahmoudi, M., Elwany, A., Yadollahi, A., Thompson, S.M., Bian, L., Shamsaei, N. (2017). Mechanical properties and microstructural characterization of selective laser melted 17-4 PH stainless steel, Rapid Prototyp. J., 23(2), pp. 280–94, Doi: 10.1108/RPJ-12-2015-0192.

[35] Seede, R., Shoukr, D., Zhang, B., Whitt, A., Gibbons, S., Flater, P., Elwany, A., Arroyave, R., Karaman, I. (2020). An ultra-high strength martensitic steel fabricated using selective laser melting additive manufacturing: Densification, microstructure, and mechanical properties, Acta Mater., 186, pp. 199–214, Doi: 10.1016/j.actamat.2019.12.037.

[36] Zhao, C., Fezzaa, K., Cunningham, R.W., Wen, H., De Carlo, F., Chen, L., Rollett, A.D., Sun, T. (2017). Real-time monitoring of laser powder bed fusion process using high-speed X-ray imaging and diffraction, Sci. Rep., 7(1), pp. 1–11, Doi: 10.1038/s41598-017-03761-2.

[37] Darvish, K., Chen, Z.W., Phan, M.A.L., Pasang, T. (2018). Selective laser melting of Co-29Cr-6Mo alloy with laser power 180–360 W: Cellular growth, intercellular spacing and the related thermal condition, Mater. Charact., 135(September 2017), pp. 183–91, Doi: 10.1016/j.matchar.2017.11.042.

[38] Zhang, B., Li, Y., Bai, Q. (2017). Defect Formation Mechanisms in Selective Laser Melting: A Review, Chinese J. Mech. Eng. (English Ed., 30(3), pp. 515–27, Doi: 10.1007/s10033-017-0121-5.

[39] Prashanth, K.G., Eckert, J. (2017). Formation of metastable cellular microstructures in selective laser melted alloys, J. Alloys Compd., 707, pp. 27–34, Doi: 10.1016/j.jallcom.2016.12.209.

[40] Roudnická, M., Molnárová, O., Drahokoupil, J., Kubásek, J., Bigas, J., Šreibr, V., Paloušek, D., Vojtěch, D. (2021). Microstructural instability of L-PBF Co-28Cr-6Mo alloy at elevated temperatures, Addit. Manuf., 44(April), pp. 102025, Doi: 10.1016/j.addma.2021.102025.

[41] Chen, Z.W., Phan, M.A.L., Darvish, K. (2017). Grain growth during selective laser melting of a Co–Cr–Mo alloy, J. Mater. Sci., 52(12), pp. 7415–27, Doi: 10.1007/s10853-017-0975-z.

[42] Takaichi, A., Suyalatu., Nakamoto, T., Joko, N., Nomura, N., Tsutsumi, Y., Migita, S., Doi, H., Kurosu, S., Chiba, A., Wakabayashi, N., Igarashi, Y., Hanawa, T. (2013). Microstructures and mechanical properties of Co-29Cr-6Mo alloy fabricated by selective laser melting process for dental applications, J. Mech. Behav. Biomed. Mater., 21, pp. 67–76, Doi: 10.1016/j.jmbbm.2013.01.021.

[43] Tonelli, L., Fortunato, A., Ceschini, L. (2020). CoCr alloy processed by Selective Laser Melting (SLM): effect of Laser Energy Density on microstructure, surface morphology, and hardness, J. Manuf. Process., 52(October 2019), pp. 106–19, Doi: 10.1016/j.jmapro.2020.01.052.

[44] Zhang, M., Yang, Y., Song, C., Bai, Y., Xiao, Z. (2018). An investigation into the aging behavior of CoCrMo alloys fabricated by selective laser melting, J. Alloys Compd., 750, pp. 878–86, Doi: 10.1016/j.jallcom.2018.04.054.

[45] Sing, S.L., Huang, S., Yeong, W.Y. (2020). Effect of solution heat treatment on microstructure and mechanical properties of laser powder bed fusion produced cobalt-28chromium-6molybdenum, Mater. Sci. Eng. A, 769(September 2019), pp. 138511, Doi: 10.1016/j.msea.2019.138511.

[46] Bawane, K.K., Srinivasan, D., Banerjee, D. (2018). Microstructural Evolution and Mechanical Properties of Direct Metal Laser-Sintered (DMLS) CoCrMo After Heat Treatment, Metall. Mater. Trans. A Phys. Metall. Mater. Sci., 49(9), pp. 3793–811, Doi: 10.1007/s11661-018-4771-4.

[47] Kajima, Y., Takaichi, A., Kittikundecha, N., Nakamoto, T., Kimura, T., Nomura, N., Kawasaki, A., Hanawa, T., Takahashi, H., Wakabayashi, N. (2018). Effect of heat-treatment temperature on microstructures and mechanical properties of Co–Cr–Mo alloys fabricated by selective laser melting, Mater. Sci. Eng. A, 726(January), pp. 21–31, Doi: 10.1016/j.msea.2018.04.048.

[48] Tonelli, L., Boromei, I., Liverani, E., Ceschini, L. (2021). Microstructural evolution induced by heat treatment in the Co28Cr6Mo alloy produced by selective laser melting, Metall. Ital., 113(2), pp. 22–30.

[49] Dolgov, N, A., Dikova, T., Dzhendov, D., Pavlova, D., Simov, M. (2016). Mechanical Properties of Dental Co-Cr Alloys Fabricated via Casting and Selective Laser Melting, Sci. Proc. Ii Int. Sci. Conf. "Innovations Eng. 2016, 33(June), pp. 29–33.

[50] Liu, F., Zhang, D.Z., Zhang, P., Zhao, M., Jafar, S. (2018). Mechanical properties of optimized diamond lattice structure for bone scaffolds fabricated via selective laser melting, Materials (Basel)., 11(3), Doi: 10.3390/ma11030374.

[51] Özeren, E., Altan, M. (2020). Effect of structural hybrid design on mechanical and biological properties of CoCr scaffolds fabricated by selective laser melting, Rapid Prototyp. J., 26(4), pp. 615–24, Doi: 10.1108/RPJ-07-2019-0186.

[52] Van Hooreweder, B., Kruth, J.P. (2017). Advanced fatigue analysis of metal lattice structures produced by Selective Laser Melting, CIRP Ann. - Manuf. Technol., 66(1), pp. 221–4, Doi: 10.1016/j.cirp.2017.04.130.

[53] Cutolo, A., Neirinck, B., Lietaert, K., de Formanoir, C., Van Hooreweder, B. (2018). Influence of layer thickness and post-process treatments on the fatigue properties of CoCr scaffolds produced by laser powder bed fusion, Addit. Manuf., 23(June), pp. 498–504, Doi: 10.1016/j.addma.2018.07.008.

[54] Koizumi, Y., Okazaki, A., Chiba, A., Kato, T., Takezawa, A. (2016). Cellular lattices of biomedical Co-Cr-Mo-alloy fabricated by electron beam melting with the aid of shape optimization, Addit. Manuf., 12, pp. 305–13, Doi: 10.1016/j.addma.2016.06.001.

[55] Lu, Y., Wu, S., Gan, Y., Zhang, S., Guo, S., Lin, J., Lin, J. (2016). Microstructure, mechanical property and metal release of As-SLM CoCrW alloy under different solution treatment conditions, J. Mech. Behav. Biomed. Mater., 55, pp. 179–90, Doi: 10.1016/j.jmbbm.2015.10.019.

[56] Tan, X.P., Tan, Y.J., Chow, C.S.L., Tor, S.B., Yeong, W.Y. (2017). Metallic powder-bed based 3D printing of cellular scaffolds for orthopaedic implants: A state-of-the-art review on manufacturing, topological design, mechanical properties and biocompatibility, Mater. Sci. Eng. C, 76, pp. 1328–43, Doi: 10.1016/j.msec.2017.02.094.

[57] Hacisalihoğlu, İ., Yildiz, F., Çelik, A. (2021). Experimental and Numerical Investigation of Mechanical Properties of Different Lattice Structures Manufactured from Medical Titanium Alloy by Using Laser Beam-Powder Bed Fusion, J. Mater. Eng. Perform., 30(7), pp. 5466–76, Doi: 10.1007/s11665-021-05865-3.

[58] Obadimu, S.O., Kourousis, K.I. (2021). Compressive behaviour of additively manufactured lattice structures: A review, Aerospace, 8(8), Doi: 10.3390/aerospace8080207.

[59] Cutolo, A., Engelen, B., Desmet, W., Van Hooreweder, B. (2020). Mechanical properties of diamond lattice Ti–6Al–4V structures produced by laser powder bed fusion: On the effect of the load direction, J. Mech. Behav. Biomed. Mater., 104(December 2019), Doi: 10.1016/j.jmbbm.2020.103656.

[60] Song, C., Zhang, M., Yang, Y., Wang, D., Jia-kuo, Y. (2018). Morphology and properties of CoCrMo parts fabricated by selective laser melting, Mater. Sci. Eng. A, 713(December 2017), pp. 206–13, Doi: 10.1016/j.msea.2017.12.035.

2.2 Modelling and FE simulation of 3D printed Co-Cr Lattice Structures for biomedical applications

2.2.1 INTRODUCTION

A new innovative architectured material is the lattice configuration, usually referred to as cellular solid [1-3]. This is a combination of a common material and space, which forms a specific array of spatial periodic unit cells repeated in the component volume, configured in such a way to create new parts that are lightweight while having high mechanical properties. The idea of a lattice structure is to use less material as possible to obtain a relatively stiff component, or only where needed. With the design flexibility allowed by Additive Manufacturing (AM) methods, lattice structures are also able to integrate more than one function into a physical part, making them attractive for a wide range of applications. In particular, the biomedical field has taken advantage of many design opportunities from these types of materials, and now with the help of AM technique, it is possible to build parts otherwise not achievable with traditional approaches. For instance, the metallic prostheses manufactured by a dense biocompatible material are often too stiff and can shield the adjacent bone tissue and cause loosening of the implant [5,7]. Lattice structures produced using bio-alloys, are a suitable alternative in the design of prosthetic implants and bone scaffolds, with the possibility to increment their fatigue resistance and to tailor their mechanical properties to reduce shear stress on the adjacent bones.

FEM analyses are widely used to predict the behavior (especially compression [5]) of components during the design phase and to reduce the number of prototypes. This make it a powerful tool to study a specific physical problem, in particular it can be used to run virtual simulation to optimize the design [6]. The lattice structures are classified according to their mechanical compression behavior, since they can exhibit a stretch-dominated or bending-dominated behavior [6]. In literature, a number of studies are reported concerning how to implement and study these structures [5–11]. In this work the results of numerical simulations were compared with experimental data from the compression tests for the validation of the numerical model. Finally, NTopology was used to evaluate the stiffness matrix of the designed cells, both with base and radial orientation.

2.2.2 MATERIALS AND METHODS

2.2.2.1 Design and production of the lattice structures

The samples were manufactured by Laser Powder Bed Fusion machine (ProX® 100, 3D System, Rock Hill, South Carolina, USA) in nitrogen atmosphere with O2 content lower than 0.1 vol. % with the studied parameters by PS Ginestra et al. [14] using Co-Cr-Mo alloy powder, which was widely studied in the biomedical sector [8,11]. The powder is characterized by the nominal chemical composition shown in Table 1.

Table 1: Nominal chemical composition (wt%) of Co-Cr-Mo powders used for the production of samples.

Co-Cr-Mo	Co	Cr	Mo	Ni	Fe	C	Si	Mn
Wt min (%)	Bal.	28.00	5.00	0.00	0.00	0.00	0.00	0.00
Wt max (%)		30.00	6.00	0.10	0.50	0.02	1.00	1.00

In this work, diamond (DM) unit cell was used to produce the lattice structures. The volume of the unit cells was 2(x) x 2(y) x 2(z) mm^3, the diameter of the struts (Dc) was 0.5 mm, and the diameter of the junction (Dn) was 1 mm.

Samples were built with two different types of building orientation, 0° and 90° in relation to the building plate, as shown in Figure 1 [14], indicated respectively as DM0 and DM90 samples. For every geometry, following the ISO standard 13314, three cylindrical specimens with height of 30 mm and diameter of 24 mm were produced, to ensure repeatability of the results.

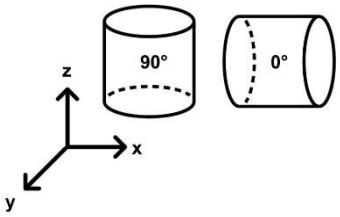

Figure 1: Samples building orientations in relation to the building plate.

In

Figure 2, pictures of DM0 and DM90 samples are reported. The different geometries obtained from the unit cells were made possible because radial symmetry was added to the geometries changing the orientation of the cells inside the component.

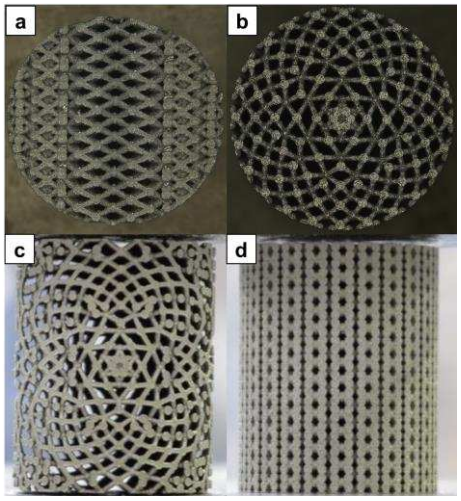

Figure 2: Top view of samples with diamond unit cell geometry at: a) 0° and b) 90° building angle and side view at: c) 0° and d) 90° building angle.

2.2.2.2 Characterization of the lattice samples

In order to study the main differences in the mechanical response, compression tests were carried out to characterize the samples under as-built condition [15]. The tests were performed following the ISO standard 13314. For these two samples families, the compression curves were divided into 90° and 0°, with the aim to analyze the change in the properties generated by the application of the radial symmetry. The tests were performed using servo hydraulic testing machines: Instron 8501 (Instron, Norwood, MA, USA) (100 kN) and Instron 500 kN, depending on the load level required with a cross head speed of 2 mm/min. The results from compression tests were collected in order to compare them with the numerical simulations.

2.2.2.3 FEM analysis

The simulations were performed using the commercial software Abaqus CAE (Dassault Systèmes SE, Vélizy-Villacoublay, France), with the aim to find the best configuration and set of parameters for the prediction of the mechanical properties of the specimens. Lattice structures are commonly tested and evaluated under compressive loading. Consequently, the goal of the analysis was to reproduce this test, comparing the prediction of the mechanical characteristics with the experimental evidence.

In principle, to simulate the compression test using FE simulation two possible strategies can be followed:

- Apply the constraints and the load/displacement directly to the specimen.
- Create two rigid plates to simulate rigid contact between the test machine plates and the specimens.

The first one simplifies the simulation, as it requires less parts and more importantly no interactions between the parts, the second one allows to better represent the real behavior of the specimen, during the real compression test.

The parameters changed in the different simulations were:

- The height of the solid model (to find the best number of cells in the vertical direction).
- The mesh size.
- The friction coefficient with the plate.
- The material model: Johnson Cook and Elasto-Plastic.

These parameters were analyzed considering the computational costs required to perform the analysis.

Tests on the samples built at 90° were simulated, as shown in Figure 3a, because those printed at 0° are too complex in terms of geometries and computational costs. The minimum number of unit cells and the portion of solid that can represent the entire structures were investigated. An element with a height of 2 mm, as the dimension of a single unit cell, and a slice of 60°, represented in Figure 3b, was found to be sufficient to study the mechanical response of whole structure.

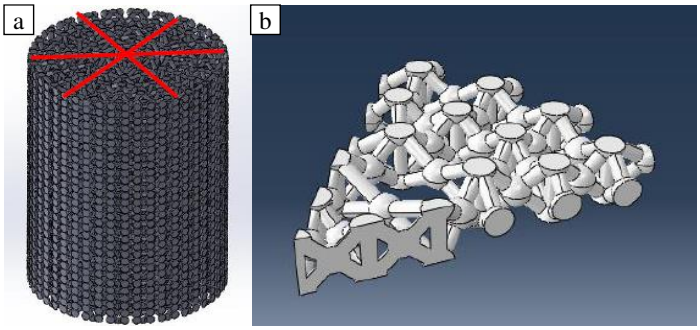

Figure 3: Minimum representative FE Model of the lattice structures built at 90°.

The section was used for the analysis of different configuration of the same model, following the approach of the work by Ruiz de Galarreta et al. [6], where geometries, with different number of unit cells along the load direction, were studied to analyze which configuration could give better results.

2.2.2.4 Stiffness Matrix for base and radial unit cell

To have a first evaluation of the type of mechanical response of unit cells, NTopology software (nTopology, NY, USA) was used, with this software it is possible to obtain the stiffness matrix representative of any kind of unit cell by means of homogenization techniques.

It is important to highlight that this method can help to understand the general mechanical response of the unit cells, in particular when dealing with structures consisting of a single linear unit cell, it also suffers some limitations when applied to complex lattice structures, as a consequence of the design constraints given from placing the unit cell inside a limited geometry. Nonetheless, for the scope of this study a single unit cell can suffice for a preliminary evaluation of the effect of cell configuration on the mechanical response, in particular regarding anisotropy.

The stiffness matrix analysis was carried out also for radial geometries with the purpose to study the effect of the radiality on the mechanical response. In this case, since the dimensions of the unit cell change depending on position, a cube of 10x10x10 mm was considered, in order to include a high number of unit cells and provide a reasonably good representation of the equivalent stiffness. To discuss the behavior of the radial geometries we considered the axis of symmetry placed in the z-direction.

2.2.3 RESULTS

2.2.3.1 Mechanical response

The results of the compression tests are reported in Figure 4. Here, the stress – strain curves recorded during the tests were classified by the building angles and compared. It is shown that both DM90 and DM0 samples are characterized by bending-dominated behavior.

The blue curves (building direction 90°) reached their first maximum, followed by a long plateau characterized by a plateau stress value, due to a local failure and densification of each layer, and showed at the end a new maximum given by the densification of the whole specimen with a deformation above 40%.

For the red ones (building direction 0°), again a long plateau up to 30% of deformation is visible. In this case, the densification effect occurs at 40% of strain. The final stress increase due to the densification effect is less marked than what observed for the samples built at 90°.

Considering the building orientation, the resistance to compressive load is higher for the samples built at 90°, while big differences in terms of deformation were not noted, because the struts of DM cells were not oriented along the load direction.

The quasi-elastic gradient and yield stress are also reported in Table 2. In particular, it is noted that the building orientation is negligible for the quasi-elastic gradient, while the variation of yield stress and energy absorption is more relevant.

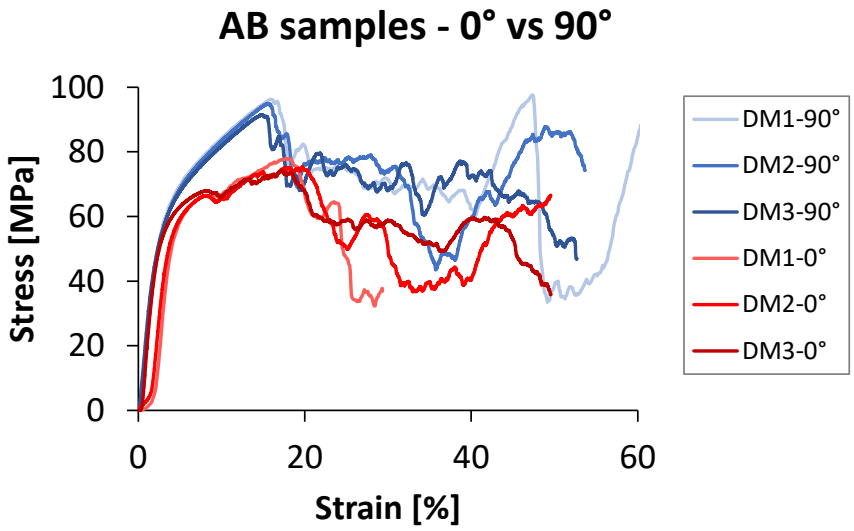

Figure 4: Stress-strain curves of AB samples with DM unit cell built at 90° and 0° (3 repetitions for each one).

Table 2: Mechanical properties of DM0 and DM90 samples.

Building orientation	E [GPa]	σy [MPa]	We [MJ/m³]
0°	2,9±0,5	66,9±0,9	24,1±6,8
90°	2,8±0,1	45,4±3,1	39±2,6

2.2.3.2 FEM Analysis

Once the experimental data were obtained, the FEM analysis was carried out. In Figure 5a a finite element model for the compression test is shown, in which, taking advantage of symmetry, a portion of the lattice structure was placed between the upper and lower rigid plates.

Considering the mesh elements, the Quadratic Tetrahedral Element (C3D10) was chosen due to the capacity to reduce, in comparison with other element, the computational effort, with a good accuracy of the results. This aspect depends also on the mesh size, shown in Figure 5b, which was varied in different simulations, in order to find an optimal value.

Furthermore, constraints and displacement were defined on the structure as shown in Figure 5c. A portion of the stress-strain curve of the material, sufficient to identify the stiffness and strength features, was studied for a computational cost issue.

To simulate the slow movement of the plate, during the compression test, a general static step was chosen. The boundary conditions were defined. One plate was fixed and the other one was moved in the vertical direction applying a displacement. Moreover, on the lateral side, constraint on the movement along the lateral direction due to the symmetry plane were imposed, while the nodes on the symmetry axis were constrained in the radial and transversal directions. In particular, the results for the DM90 sample were analyzed.

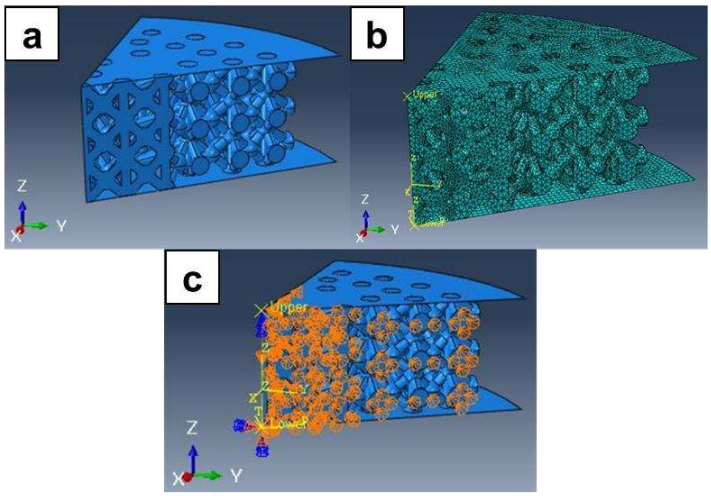

Figure 5: Representation of a) FE model, b) FE Mesh, and c) Constraints and displacement on the FEA model.

Mesh size

A mesh sensitivity analysis was performed to capture influence of the mesh size on the accuracy of the results and on the computational time. When considering the Young Modulus, it was noticed that a finer mesh size results in a lower overall stiffness. On the other hand, when using a smaller mesh size, the simulation requires higher computational costs due to the higher number of elements inside the FEA, reducing the overall advantage given by using finer meshes.

2.2.3.3 Friction coefficient

In Figure 6, the results for the predicted Young Modulus and yield stress are shown, obtained by using three different plate friction coefficients from 0.1 to 0.3 for three different samples geometries, with one-, two-, and three-unit cells along the vertical direction. The material model used is the Johnson-Cook model while for the finite element it was used quadratic tetrahedral element C3D10 set to a dimension of 0.2.

From this analysis, it can be understood that increasing the height of the model could decrease the overall stiffness of the lattice by mitigating the effect of friction, which, on one side, better represents the behavior of the lattice.

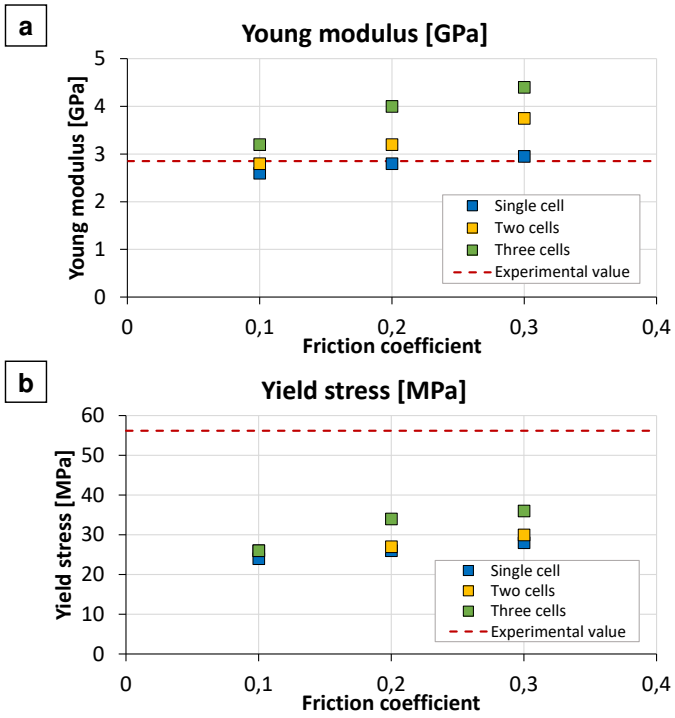

Figure 6: a) Young modulus FE model result, b) Yield stress FE model result

Increasing the tangential friction coefficient increases the stiffness, resulting in higher resistance for the longitudinal expansion of the lattice model. On the other hand, due to the high porosity and roughness of the lattice surface, it seems that higher friction coefficient could be more realistic to simulate the behavior of the lattice during the test. Increasing the height of the model allows to simulate more accurately the behavior of the lattice but, on the other hand, it increases the computational costs and time required for the simulations.

The same analysis was made considering the Yield Stress. The same trend detected for the Young Modulus was observed, but, in this case, the simulation tends to underestimate the strength of the lattice with a maximum value lower than the experimental data.

2.2.3.4 Material law

Once the tangential friction coefficient and mesh size of the FEA were considered, a comparison between the curves of the experimental compression test and the FEA using the Elasto-Plastic and Johnson-Cook model was studied, as shown in Figure 7. The parameters needed for the model were obtained basing on the mechanical properties for SLM Co-Cr-Mo alloys previously investigated in [16-17] It can be appreciated that the experimental curve was characterized by the same trend of the theoretical ones.

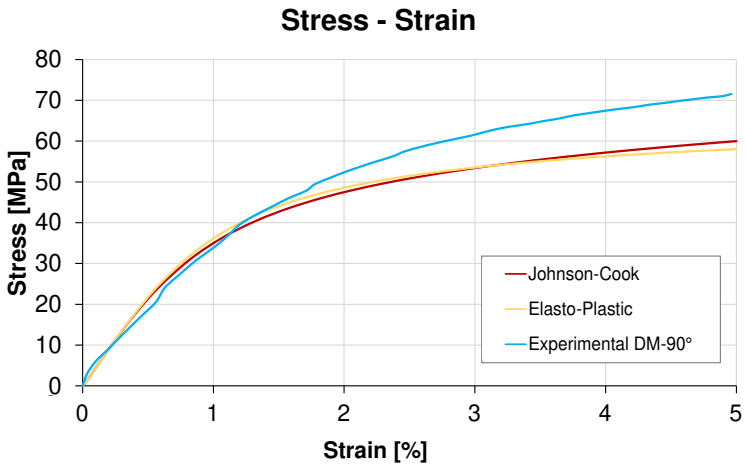

Figure 7: Comparison between the experimental (DM90) and simulated curves using the two materials model, Johnson-Cook and Elasto-Plastic.

It is noted that the curve predicted by the computational model is more accurate at low strain values, but it presented a higher discrepancy at higher strain value. One of the possible reasons of such difference between FEA and experimental results was probably due to the 3D models, which represent an idealized geometry of the real parts. In fact, the ideal model does not consider all the geometry's inaccuracies and errors due to the manufacturing process added to the lattice structure.

2.2.3.5 Stiffness matrix

For the purpose of this first evaluation, and to make considerations only upon the topology of the DM unit cell, an equivalent elastic isotropic material was considered, assuming 1 Pa for the Young Modulus and 0.3 for the Poisson Coefficient.

In Figure 8a, the stiffness distribution was reported. The regions in red show the direction of the unit cell where the stiffness is higher, while the blue one represents the direction of the unit cell with the lower stiffness. For a perfect isotropic material, the image representative of the stiffness matrix would be a perfect homogeneous sphere. The DM Cell is characterized by a good stiffness, but only in direction of its inclined struts meanwhile, it shows a lower stiffness along the other directions.

As shown in Figure 8b, the DM radial cell shows a different behavior from that of the fixed unit cell. In this case, the stiffness is more homogeneous in the direction transversal to the axis of symmetry but as before, there is higher compliance in the z direction. The effect of the radiality on the macroscopical mechanical response is to homogenize the stiffness along the planes perpendicular to the axis of symmetry. This is due to the change in the orientation of the struts since the size of the unit cells varies along the radius of the structure.

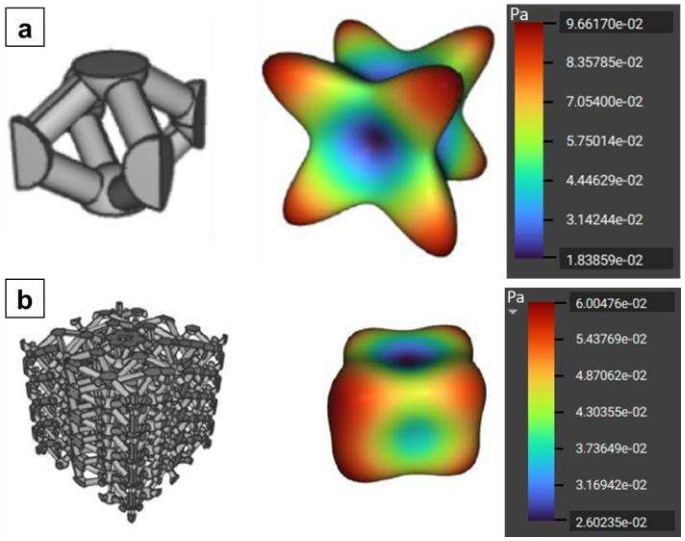

Figure 8: Representation of the stiffness matrix for the a) fix and b) radial unit cells.

2.2.4 CONCLUSIONS

In this work, the mechanical properties of lattice structures characterized by diamond radially oriented unit cell, manufactured by L-PBF using Co-Cr-Mo alloy, were characterized, and compared to the FEA and stiffness matrix results. The compression test on AB were performed. Subsequently, the FEA and stiffness's matrix were simulated to predict the structural behavior of the samples.

The experimental trend of the simulated stress-strain curve resulted really close to the experimental ones except for high strain values, probably because of the geometry's inaccuracy due to the manufactured process. The stiffness matrix trend was also evaluated in support to the FEA analysis, to have a better visualization of the simulated result. It was demonstrated that the radial orientation of the cells provides a homogenization of the stiffness along the planes perpendicular to the axes of symmetry. These considerations can be helpful for the design and production of prostheses or implants, which are widely used in the biomedical field.

In literature the validations of FEM analysis for lattice structures, with particular configurations and orientations of cells, have not yet been deeply investigated. The present study allowed to have a prediction of mechanical behavior of radially graded lattice structures. In particular, the possibility to study a single slice of the structure has allowed to significantly reduce the time and costs required by the FEM analysis. Compression tests to validate the software results were needed. Once validated, the mechanical characteristics were consistent with radial cells orientation. The mechanical features of radially graded lattice structure characterized by diamond unit cell can be exploited for biomedical prosthesis applications.

References

[1] M. F. Ashby, "The properties of foams and lattices," Philos. Trans. R. Soc. A Math. Phys. Eng. Sci., vol. 364, no. 1838, pp. 15–30, 2006, doi: 10.1098/rsta.2005.1678.

[2] B. Van Hooreweder, K. Lietaert, B. Neirinck, N. Lippiatt, and M. Wevers, “CoCr F75 scaffolds produced by additive manufacturing: Influence of chemical etching on powder removal and mechanical performance,” J. Mech. Behav. Biomed. Mater., vol. 70, pp. 60–67, 2017, doi: 10.1016/j.jmbbm.2017.03.017.

[3] P. F. Egan, V. C. Gonella, M. Engensperger, S. J. Ferguson, and K. Shea, “Computationally designed lattices with tuned properties for tissue engineering using 3D printing,” PLoS One, vol. 12, no. 8, pp. 1–20, 2017, doi: 10.1371/journal.pone.0182902.

[4] S. Xu, J. Shen, S. Zhou, X. Huang, and Y. M. Xie, “Design of lattice structures with controlled anisotropy,” Mater. Des., vol. 93, pp. 443–447, 2016, doi: 10.1016/j.matdes.2016.01.007.

[5] P. S. Ginestra, E. Ceretti, and A. Fiorentino, “Potential of modeling and simulations of bioengineered devices: Endoprostheses, prostheses and orthoses,” Proc. Inst. Mech. Eng. Part H J. Eng. Med., vol. 230, no. 7, pp. 607–638, Apr. 2016, doi: 10.1177/0954411916643343.

[6] S. Ruiz de Galarreta, J. R. T. Jeffers, and S. Ghouse, “A validated finite element analysis procedure for porous structures,” Mater. Des., vol. 189, p. 108546, 2020, doi: 10.1016/j.matdes.2020.108546.

[7] Z. Xiao, Y. Yang, R. Xiao, Y. Bai, C. Song, and D. Wang, “Evaluation of topology-optimized lattice structures manufactured via selective laser melting,” Mater. Des., vol. 143, pp. 27–37, 2018, doi: 10.1016/j.matdes.2018.01.023.

[8] M. R. Karamooz Ravari and M. Kadkhodaei, “A Computationally Efficient Modeling Approach for Predicting Mechanical Behavior of Cellular Lattice Structures,” J. Mater. Eng. Perform., vol. 24, no. 1, pp. 245–252, 2015, doi: 10.1007/s11665-014-1281-4.

[9] G. Campoli, M. S. Borleffs, S. Amin Yavari, R. Wauthle, H. Weinans, and A. A. Zadpoor, “Mechanical properties of open-cell metallic biomaterials manufactured using additive manufacturing,” Mater. Des., vol. 49, pp. 957–965, 2013, doi: 10.1016/j.matdes.2013.01.071.

[10] M. R. Karamooz Ravari, M. Kadkhodaei, M. Badrossamay, and R. Rezaei, “Numerical investigation on mechanical properties of cellular lattice structures fabricated by fused deposition modeling,” Int. J. Mech. Sci., vol. 88, pp. 154–161, 2014, doi: 10.1016/j.ijmecsci.2014.08.009.

[11] H. Sadeghi, D. Bhate, J. Abraham, and J. Magallanes, “Quasi-static and dynamic behavior of additively manufactured metallic lattice cylinders,” AIP Conf. Proc., vol. 1979, pp. 1–15, 2018, doi: 10.1063/1.5044838.

[12] B. Lozanovski et al., “Computational modelling of strut defects in SLM manufactured lattice structures,” Mater. Des., vol. 171, p. 107671, 2019, doi: 10.1016/j.matdes.2019.107671.

[13] M. Forets, D. F. Caporale, and J. M. P. Zerpa, “Combining Set Propagation with Finite Element Methods for Time Integration in Transient Solid Mechanics Problems,” 2021, doi: 10.1016/j.compstruc.2021.106699.

[14] P. S. Ginestra, L. Riva, G. Allegri, L. Giorleo, A. Attanasio, and E. Ceretti, “Analysis of 3D printed 17-4 PH stainless steel lattice structures with radially oriented cells,” Ind. 4.0 – Shap. Futur. Digit. World, pp. 136–141, 2020, doi: 10.1201/9780367823085-25.

[15] L. Riva, P. S. Ginestra, and E. Ceretti, “Mechanical characterization and properties of laser-based powder bed–fused lattice structures: a review,” Int. J. Adv. Manuf. Technol., vol. 113, no. 3–4, pp. 649–671, 2021, doi: 10.1007/s00170-021-06631-4.

[16] G. Cornacchia, S. Cecchel, D. Battini, C. Petrogalli, and A. Avanzini, “Microstructural, Mechanical, and Tribological Characterization of Selective Laser Melted CoCrMo Alloy under Different Heat Treatment Conditions and Hot Isostatic Pressing,” Adv. Eng. Mater., vol. 2100928, 2021, doi: 10.1002/adem.202100928.

[17] S. M. J. Razavi, A. Avanzini, G. Cornacchia, L. Giorleo, and F. Berto, “Effect of heat treatment on fatigue behavior of as-built notched Co-Cr-Mo parts produced by Selective Laser Melting,” Int. J. Fatigue, vol. 142, no. August 2020, p. 105926, 2021, doi: 10.1016/j.ijfatigue.2020.105926.

Chapter 3
Ti-6Al-4V

In this chapter the mechanical and microstructural characterization of Ti-6Al-4V lattice structures produced with Laser Powder Bed Fusion (L-PBF) and Electron Beam Powder Bed Fusion (EB-PBF) are carried out. Moreover, the single contour strategy for the production of Ti-6Al-4V lattices with L-PBF is evaluated and optimized. Finally, a case study is realized and characterized.

The published papers related to the Ti-6Al-4V alloy are listed below:

- Cantaboni F, Battini D, Hauber KZ, Ginestra PS, Tocci M, Avanzini A, et al. Mechanical and microstructural characterization of Ti6Al4V lattice structures with and without solid shell manufactured via electron beam powder bed fusion. The International Journal of Advanced Manufacturing Technology 2024. https://doi.org/10.1007/s00170-024-13137-2.
- Cao, X., Carter, L. N., Villapún, V. M., Cantaboni, F., De Sio, G., Lowther, M., Louth, S. E. T., Grover, L., Ginestra, P., & Cox, S. C. (2022). Optimisation of single contour strategy in selective laser melting of Ti-6Al-4V lattices. Rapid Prototyping Journal, 28(5), 907–915. https://doi.org/10.1108/RPJ-04-2021-0103.
- Cantaboni, F., Ginestra, P., Tocci, M., Ceretti, E., De Sio, G., Cao, X., Carter, L. N., Villapún, V. M., Lowther, M., Louth, S., & Cox, S. C. (2022). Selective Laser Melting of Ti-6Al-4V Lattices: Case Study on a Spinal Cage Prosthesis. Key Engineering Materials, 926 KEM, 147–158. https://doi.org/10.4028/p-g7ip54.

3.1 Mechanical and microstructural characterization of Ti6Al4V lattice structures with and without solid shell manufactured via Electron Beam Powder Bed Fusion

3.1.1 Introduction

Additive Manufacturing (AM) can be successfully used to produce metallic structures. In particular, Powder Bed Fusion (PBF) systems are in constant growth and present many advantages over traditional technologies since they allow to produce structures with complex internal shapes [1–5]. In PBF systems, both laser and electron beam sources can be used to melt the metal powder [6,7].

In the Electron Beam Powder Bed Fusion (EB-PBF) process, the electron beam locally melts the powder in a vacuum atmosphere and the build chamber is maintained at high temperature (~1000°C or above if needed) during the manufacturing process. This allows to obtain samples and components with reduced residual stresses. On the other hand, components produced with this technology suffer from poor surface quality due to the beam energy [8].

One of the most used alloys in the industrial applications of AM is Ti6Al4V alloy, applied in several fields due to its relevant mechanical properties, high corrosion resistance, and good processability, also at high temperatures [9]. For instance, Ti6Al4V alloy is widely used for the production of biomedical implants [10]. Furthermore, Ti6Al4V alloy is used for the production of porous structures, such as scaffolds and lattice structures, needed for lightweighting and reducing the stiffness of components [2,6-7].

Lattice structures can be easily manufactured using EB-PBF techniques modifying the cell type and size in order to have different densities. Specifically, lattices can be applied in energy absorption applications, such as packaging and protective devices, and have potential applications in thermal systems [11]. Different studies analyzed the mechanical behavior of lattice structures by changing the density and cell and strut dimensions [12,13]. It was demonstrated that the production of lattice structures with PBF technology is affected by the size, length, and orientation angle of struts [14]. Several studies on the geometry of lattice manufactured with EB-PBF are also reported in the literature. Hernández-Nava et al. [15] found that the dimensions of the struts differed from the designed one and were undersized due to the sub-optimal offset in the contour parameters. The welding process produced an oversizing of the small features when a contour around the strut diameter was applied. Suard et al. [16] demonstrated a discrepancy in size between the designed and manufactured struts which induced a decrease in the stiffness of the strut and Young's modulus in the lattices due to mismatches between CAD and as-built parts. Huang et al. [17] demonstrated that the struts of the sample were highly irregular and rough. The main contributing factor was the partially melted powder adhered to the surface which was formed during the EB-PBF process. The application of EB-PBF led to an average strut size that exceeded the designed strut size by more than 10%.

Among the different challenges in the design, production, and characterization of components containing a lattice structure, the interaction between the lattice itself and a solid surface or a bulk part represents a crucial

topic. In fact, rarely purely lattice components are manufactured, but more often the lattice is surrounded by or connected to solid walls, which can influence the mechanical behavior of the component.

In this regard, Güden et al. [18] investigated the effect of the number of cells, strut diameter and rigid-face sheets on the compression behavior of EBM-Ti6Al4V Body Centered Cubic lattices. The addition of a dense layer that covered the lattice core altered the behavior of the structure compared with the lattice without a solid shell. The solid layer constrained the edge of the lattice and the fracture mode changed with and without the solid face sheets. Moreover, the mechanical properties of foam-filled tubes were investigated by Novak et al. [19]. In this study, thin-walled tubes were filled with various metal lattices. The interaction between tube and lattice structures gave a positive contribution to the energy absorption increasing the impact properties. This application is useful not only for the biomedical application but also for the automotive, marine aerospace, and railway industries. Furthermore, Xiong et al. [20] studied porous metallic scaffolds with dense core structures with different diameters to test the effectiveness in enhancing the strength of the scaffold. The tested lattice structures with dense cores exhibited mechanical features and level of porosity favorable for biomedical applications. Finally, Fu et al. [21] focused on the mechanical properties of triply periodic minimal surface shell lattices produced by micro laser powder bed fusion. The lightweight design was analyzed, and the deformation mechanisms and mechanical properties of the shell lattices were correlated to the relative density. The deformation mechanism was highly dependent on the relative density, and the discrepancy between the design and measured values of the shell thickness was a crucial point, especially for the low-density structures. These studies revealed that the addition of the solid part resulted in an increase in mechanical properties due to the higher load support than the lattice without the shell. Moreover, enhanced compression strength and energy absorption were also detected maintaining a good level of porosity of the samples. An additional example is the investigation by Dong et al. [22] into solid-lattice hybrid structures, which consist of both solid and lattice components. In this study, a specifically designed model of solid-lattice hybrid structure was introduced. The model included optimized strut thickness connected to the solid part through Boolean operations and was compared with both pure solid and pure lattice structures. The findings illustrated that the solid-lattice hybrid structure exhibited superior mechanical performance. Additionally, lattice structures are incorporated into pre-existing components to reduce weight while maintaining equivalent mechanical properties, as highlighted by Bertol et al. [23]. Moreover, Wang et al. [24] suggested a multi-scale design approach for solid-lattice hybrid structures to provide new opportunities for next-generation aerospace vehicle components, characterized by lightweight construction and high-performance improvement.

The relevant number of studies that mention the interaction between a solid and a lattice structure demonstrates the growing interest in these designs and the relative mechanical behavior. From the literature, it appears that it is crucial to analyze how the connections between the struts and the solid wall influence the behavior of these structures and how the defects are distributed. However, the solid part in the hybrid structure is usually applied above and below the lattice part (lattice sandwich structure). In the present study, the designed solid shell was

applied on the lateral side of the lattice, parallel to the direction of the compression load. The shell constrains the inner lattice avoiding its free expansion under compression load. In contrast to the hybrid structures studied in the literature, the solid-lattice interface was affected by stress due to the compression load and deformation of the inner lattice part. The compression behavior of lattice with lateral-shell, and the interface solid-lattice, were investigated.

In particular, in this work, Ti6Al4V lattice structures with Body Centered Cubic (BCC) unit cells were designed with and without a solid shell and produced by the E-PBF process with an orientation of 90° in relation to the building platform in order to provide additional insight into the behavior of such complex structures.

The microstructural and mechanical characterization of the samples were carried out on the samples with and without the shell. The analysis of the lattice without the solid shell was carried out for comparison to provide a better understanding of load-bearing capacity of the hybrid solid-lattice structure. Moreover, Finite Element Model (FEM) parameters were extracted based on the mechanical tests on the lattice structures and a numerical analysis of the mechanical performances was carried out to compare experimental and simulation results.

3.1.2 Materials and methods

3.1.2.1 Samples production

The Ti6Al4V square-based lattice structures were designed using PTC Creo parametric (CREO®). The samples were characterized by a Body Centered Cubic (BCC) unit cell with a length (a) of 2 mm, a volume of 2 x 2 x 2 mm3, and cylindrical struts with diameter (Øs) of 500 μm, as reported in Figure 1. For better comprehension, the junction of the oblique struts will be named node.

As reported in Figure 1, the lattice structures were designed with and without an external solid shell. The structures are named S and NS, respectively (Figure 1). The dimension of both sets of samples was 24 (L) x 24 (L) x 30 (H) mm, where L and H are the length and the height of the cube, respectively. The thickness of the shell (t) was 1 mm. The samples with and without solid shell were produced with an orientation of 90° in relation to the printing plate (plane XY), which represents the vertical direction [25]. This configuration was chosen to ensure that the growth of the four walls was perpendicular to the direction of the roller avoiding distortion of the structure.

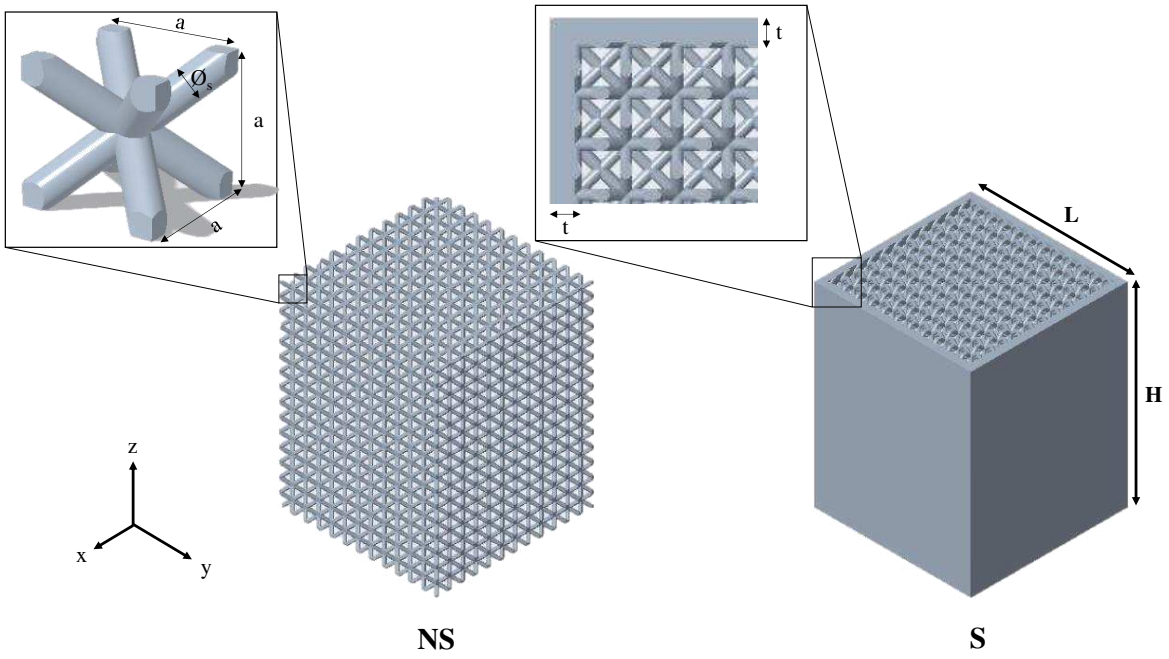

Figure 1: Design of Body Centered Cubic (BCC) unit cell and design of the samples with and without solid shell (S and NS) produced with an orientation of 90° respect to the printing plate xy.

The samples were manufactured with Ti6Al4V (Grade 5) alloy powder, with particle size distribution (PSD) in the range of 40-80 μm [26], produced by GE additive®. The nominal chemical composition is reported in Table 1 [13].

Table 1: Chemical composition of Ti-6Al-4V alloy.

Ti6Al4V	Al	V	Fe	C	O	N	H	Ti
Wt min (%)	5.50	3.50	0.00	0.00	0.00	0.00	0.00	
Wt max (%)	6.75	4.50	0.30	0.08	0.20	0.05	0.02	Bal.

Each sample was designed as a unique .STL file considering the lattice and the shell part merged. The specimens were produced by EB-PBF technology (Arcam EBM A2X, GE®, USA) with a single set of process parameters reported in Table 2. The process parameters used in the present study were selected based on a previous work of some of the Authors [27]. In this paper, it is clearly demonstrated that the selected set of process parameters are optimal to produce samples with different building directions in relation to the printing plate correlated to the orientation of the struts of the lattice.

Table 2: Process parameters of EB-PBF Arcam EBM A2X machine [27].

Process Parameters	
Hatch spacing [μm]	100
Spot size [μm]	200
Layer thickness [μm]	50
Scanning speed [mm/s]	4530
Beam current [mA]	15
Max beam current [mA]	21
Focus offset [mA]	3

3.1.2.2 Samples morphology and structure.

First, the size of the samples was measured by Vernier caliper to assess the repeatability of the process. In addition, the struts morphology was observed with a scanning electron microscope (SEM), LEO EVO® 40 (Carl Zeiss AG, Italy).

For the microstructural characterization, one sample for each condition was cut to observe the cross-sections parallel and normal to the building direction. Samples were mounted in acrylic resin and polished up to mirror finishing according to conventional metallographic practices. Polished samples were observed using LEICA DMI 5000 M optical microscope (Wetzlar, Germany). The diameter of the struts and the thickness of the solid shell were measured on 60 micrographs (magnification 50x) and average values and standard deviations were calculated in order to obtain reliable results. The diameter of the strut was measured as the width of the cross-section of the strut.

Image analysis was carried out on 70 micrographs (magnification 50x) with the LAS software to evaluate the porosity level of the samples. The porosity analysis was carried out on the lattice (struts and nodes) and shell separately. The porosity of the samples was estimated as the ratio of the total pores area to the total area of the cross-section of the lattice.

Selected samples were etched with Kroll's reagent for 15 s to identify the microstructure along the longitudinal and transversal directions.

After compression tests, the fracture surface was analyzed using a Scanning Electron Microscope (SEM) (FEI Inspect S, FEI Co., USA).

3.1.2.3 Mechanical analysis

Compression tests were performed with a servo-hydraulic testing machine INSTRON 8802 (Instron, Norwood, MA, USA) equipped with a 250 kN load cell. The tests were conducted in displacement control mode at a constant crosshead speed of 2 mm/min and the displacement was measured using the crosshead movement. The stress (σ) was calculated by dividing the force by the nominal cross-section area of the sample as a filled cube, defined as the square of length (l) of each square-based sample measured. The strain (ε) was obtained by dividing the displacement by the initial height of each sample. The ultimate strength (σm) was identified as the maximum and the yield stress (σY) was defined as the stress at 0.2% of plastic deformation. The elastic modulus was calculated considering the linear trend of the elastic field of the stress-strain curves. Three repetitions for each sample were carried out and the tests were considered completed when the samples reached 20% of strain, to assure uniformity of results interpretation. Moreover, the energy absorption was calculated until the first peak of stress (WM) and until the end of the compression test (We) by Equation 1.

$$\boldsymbol{W = \frac{1}{100}\int_{0}^{\varepsilon_0} \sigma d\varepsilon} \qquad \text{Eq. 1}$$

W is the energy absorption per unit volume, σ is the nominal compressive stress calculated as the load over the full cross-section area, ε is the nominal strain calculated as the crosshead displacement over the initial length and ε_0 is the upper limit of the compressive strain. The equation was divided by 100 because the strain value was defined as a percentage. In addition, the fracture and failure modes of the samples were investigated.

3.1.2.4 Finite element model

The finite element software Simulia Abaqus® was used to simulate the behavior of the lattice samples within the elastic regime. Since there is abundant evidence in the literature that FEA of lattice structures is difficult, different models were implemented, based on different assumptions regarding deviations of the real structure and testing conditions from the ideal ones. A total of six different models were realized with three geometry/material variants for the S lattice and three geometry variants for the NS lattice. One variant for each lattice type represented the stiffest condition which corresponds to the ideal lattice specimens (material constants from the powder supplier's datasheet and nominal geometry). A second variant represented lattice specimens with average stiffness, associated with average geometry size and an average Young modulus correction to account for shell porosities. A third variant represented lattice specimens with minimum stiffness, associated with minimum geometry size (assumed as average minus one standard deviation, see Table 3) and maximum Young modulus correction.

Overall, the nominal Young modulus is 120 GPa and the correction was only applied to the shell material as the porosity level of struts and nodes porosities was negligible. Since different approaches to predict a modulus correction are available, a corrected Young modulus range of 100-110 GPa for 6% porosity was gathered by considering the analytical approach from [28], the FEM approach from [29] and the experimental data on Laser-Powder Bed Fusion (L-PBF) Ti6Al4V from [30,31]. For this reason, a Young modulus of 105 GPa was used for the shell material of the average stiffness variant, and a Young modulus of 100 GPa was used for the most compliant variant.

The current FEM model aims at estimating stiffness and its validity is limited to the macroscopic linear-elastic response of the lattice. This choice allowed exploiting all the symmetry planes of the geometry and boundary/loading conditions, thus leading to the model of 1/8th of the cross-section and half-thickness layer (see Fig. 2). The modelling of non-linear effects is well beyond the purpose of the current finite element study as catching the full response of the compression tests would require the experimental characterization of a damage constitutive law and, possibly, the implementation of local defects, non-ideal geometry, trapped unmelted powder and the full lattice to also account for friction at lattice ends.

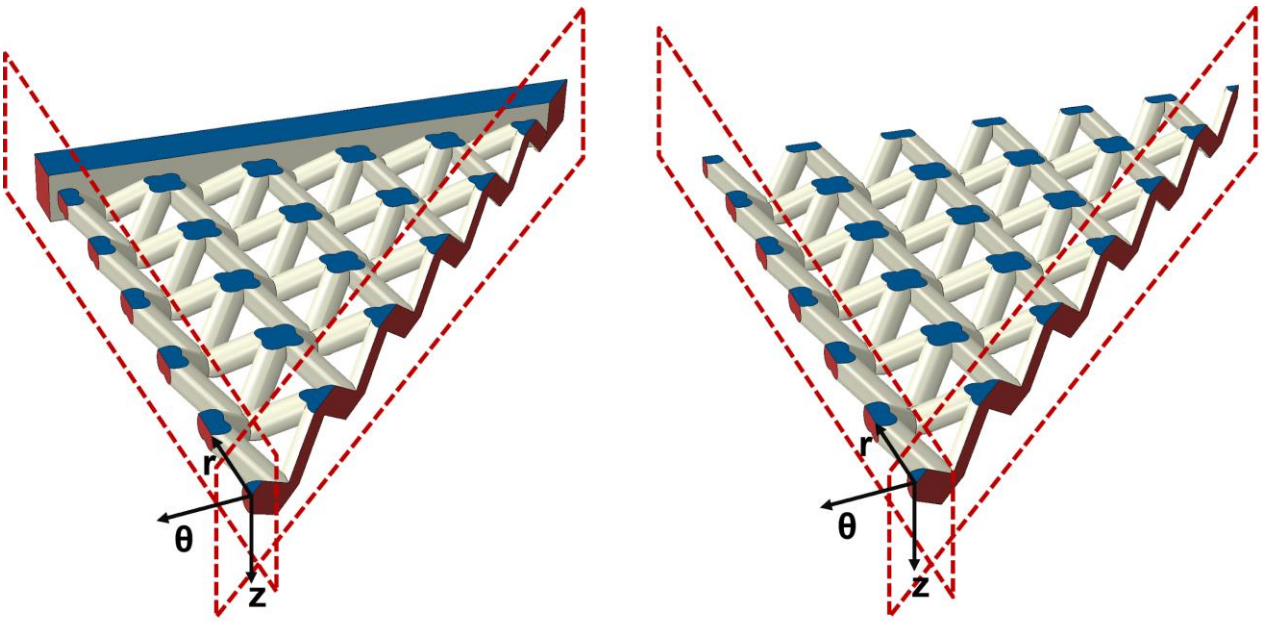

Figure 2: FEM model of the lattice structures (nominal S on the left, nominal NS on the right).

A Z- displacement was applied on the face highlighted in blue while the opposite face was constrained with a Z-symmetry boundary condition. Faces highlighted in red were instead constrained with a symmetry boundary condition along the tangential direction of a cylindrical coordinate system centered on the Z-axis.

3.1.3 Results and discussions

3.1.3.1 Lattice characterization

The dimensions of the manufactured struts of S and NS samples were measured and reported in Table 3.

Table 3: Measured dimensions of As-Built S and NS lattice samples.

	H [mm]	L [mm]
S	29.41 ± 0.04	23.75 ± 0.05
NS	30.13 ± 0.09	24.03 ± 0.07

The dimensions of the S parts are lower than the designed one as already analyzed [16]. For the NS parts, the dimensions are quite close to the designed ones. The differences between the experimental and the designed values can be attributed to the irregularities of the surfaces [26] and can be due to the suboptimal offset of contour parameters and influenced by the strut inclination angle [14,16].

The morphology of the struts of NS samples was observed under SEM (Figure 3). The surface appears extremely irregular, with unmelted or partially melted powder particles clearly visible on all the struts (Fig. 3a-b). The irregularity of the surface was not attributed to the samples design but to the production process. The spot of the electron beam, the residual powder adhered on the surface, and the strut orientation, changed the size of the diameter as already observed in the literature [32,33]. The SEM images of S samples are not reported for brevity's sake since they showed the same features.

The partially melted powder is more visible in Figure 3c with an average particle size of 62 ± 17 μm, which is within the nominal range value of 40 - 80 μm reported on the datasheet of the Ti6Al4V alloy powder [34]. Moreover, the high variation in the thickness of the struts is particularly evident in Fig. 3c, where also a staircase-shaped profile can be observed, with gaps between layers. An evident staircase effect is typical for the EB-PBF process, leading to larger surface roughness [35]. The evident irregularity in the size of the struts will be better investigated by performing a specific dimensional analysis on the cross-section of the samples. Moreover, the surface of the struts, with the layer scanned by electron beam partially covered by the next one, is visible in Figure 4d, as mentioned also by Zhang et al. [14].

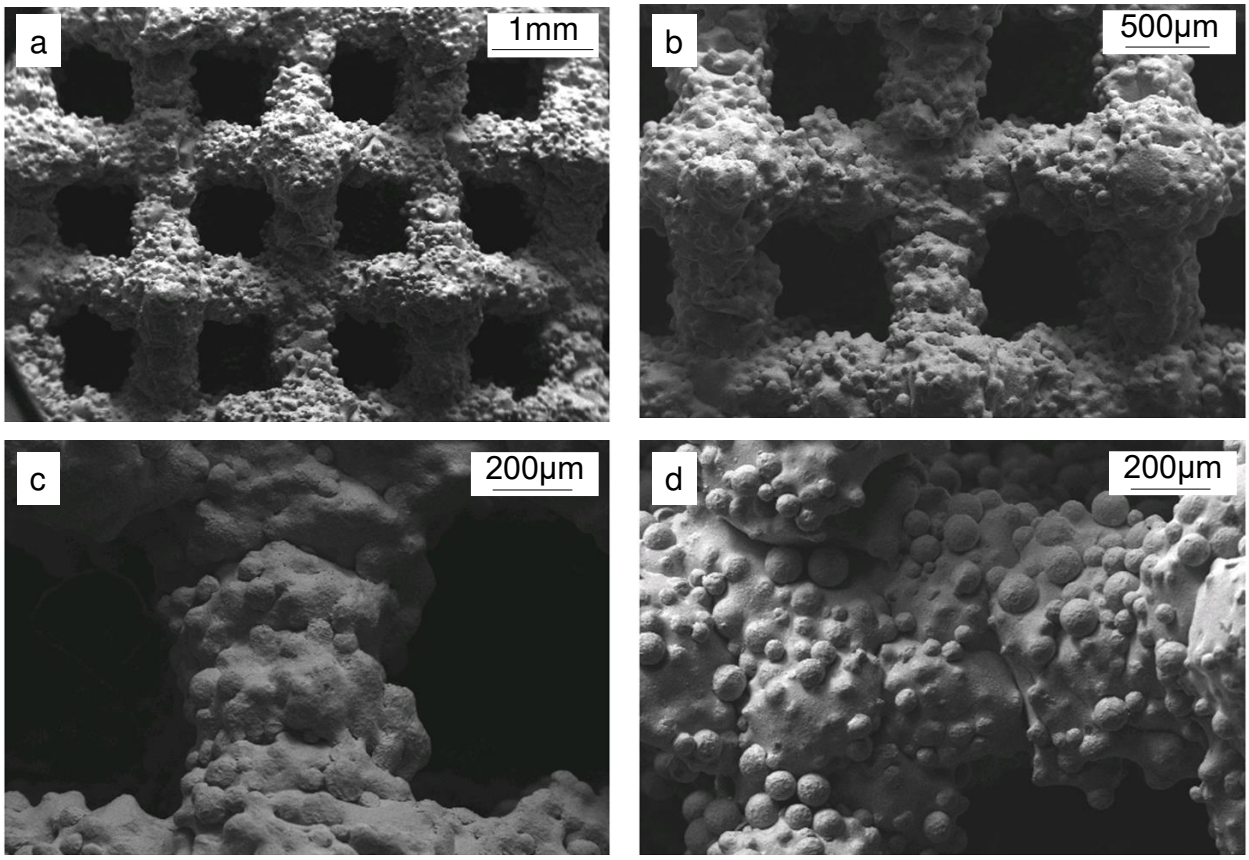

Figure 3: SEM images of the (a) strut and (b) node connections, (c) different melted layers and (d) unmelted powders for NS samples.

The thickness of the solid shell for S samples and the diameter of the struts for S and NS samples were measured on three different cross-sections of the specimens and the results are reported in Table 4.

The struts appear extremely irregular in size, as seen by SEM analysis. The diameter of the struts for S and NS samples differ by 10% and 5% from the designed size (500 μm), respectively. The significant standard deviation detected is likely due to the inclination angle of the struts and the presence of partially melted and unmelted powder.

The thickness of the shell is lower than the designed one and shows an instability in size, demonstrated by the large standard deviation. The dimension fluctuates from a minimum of 406 μm to a maximum of 810 μm. In

Figure 4 the irregular geometry on the cross-section normal (Fig. 4a) and parallel (Fig. 4b) to the building direction is shown.

As abovementioned, the porosity of the samples was calculated using image analysis along the cross-section normal and parallel to the building direction on the solid shell and the lattice part (nodes and struts). A relatively high porosity level of 5 % was detected on the shell, while a porosity level of 0.6 % on the struts and nodes was measured for the S samples. A porosity value of 0.4 % was detected for the struts and nodes cross-section of NS samples. The results are in accordance with porosity analysis from Suard et al. [16] and Neils et al. [36].

The reason behind the significant porosity level of the shell can be found in the process parameters, and more precisely in the contour strategy and hatch spacing used [37,38]. Moreover, it has been decided to set the same process parameter for both lattice and shell, merging them in a unique component. In fact, large porosities can be observed in the central part of the solid shell because the strategy of the beam and the hatch spacing used for the lattice part were also used for the shell. This indicates that the powder was melted on the edge of the solid shell but not in the center. The unmelted powder was detected in the central part of the shell: this resulted in the large lack-of-fusion porosities observed and reported in Figure 4a-b, due probably to the hatching distance of the electron beam. The interface between lattice and solid part shown in Figure 4b did not reported significant defects such as porosity or geometry discrepancy. The continuity of the building was due to the same process parameters applied for both parts merging them as a single component.

Table 4: Measured dimensions of As-Built S and NS lattice samples.

	Øs [µm]	tk [µm]
S	459 ± 43	608 ± 202
NS	475 ± 41	-

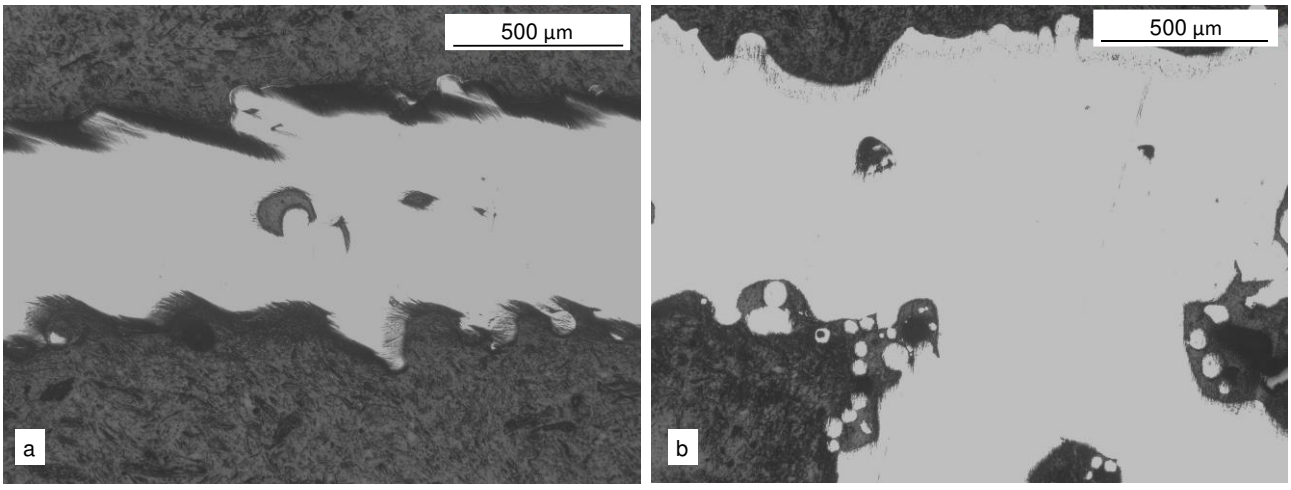

Figure 4: Micrographs of the cross-section normal to the building direction of solid shell (a) and strut and solid shell (b) of S90 sample.

3.1.3.2 Microstructure

Micrographs of NS samples are shown in Figure 5 as representative of the microstructure of all the investigated samples. No relevant differences between the shell and lattice part of the samples are found, as well as between the S and NS samples, due to the use of the same process parameters. In general, the microstructure of Ti6Al4V

alloy is composed of a α + β lamellar microstructure within the previous β columnar grains oriented along the building direction. The α lamellae are arranged in Widmanstätten structure characterized by different sizes and orientations. The mentioned microstructural features are widely reported in the literature for Ti6Al4V alloy [39,40]. More specifically, the microstructural features due to the EB-PBF process are discussed in [35,38].

The microstructure normal to the building direction is shown in Figure 5a. The colony pattern of α + β lamellar structure arranged in the equiaxed microstructure can be observed. In fact, along this direction, the cross sections of the columnar grains can be observed.

The microstructure parallel to the building direction, characterized by a columnar structure, is shown in Figure 5b. The colony pattern of α + β lamellar structure can be observed.

Moreover, the light and dark phases identify the α and β phases respectively, as shown in Figure 5c. In particular, the grain boundary α layer was found around the prior β grain (Figure 5d) [41].

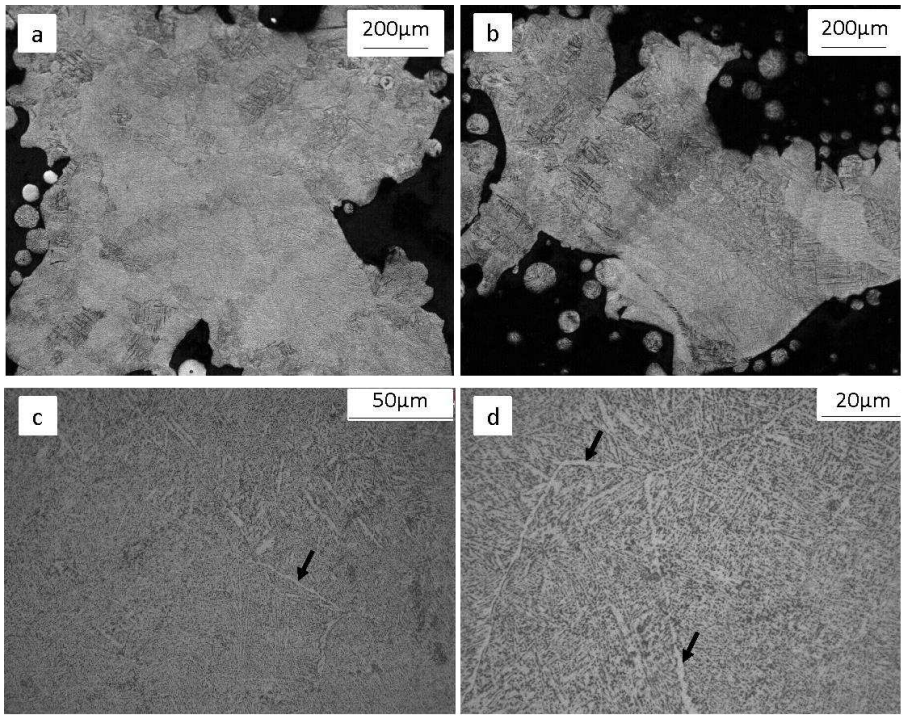

Figure 5: Optical micrographs normal (a) and parallel (b) to the building directions of cross sections of NS90 sample. Optical micrographs parallel to the building direction (c,d). Colony pattern α + β lamellar structure divided by α phase layer (marked by black arrows) within the prior β grain boundaries.

3.1.3.3 Mechanical characterization

Representative stress-strain curves resulting from the compression tests of S and NS samples are reported in Figure 6a.

The curves are reported until 20 % strain, since for higher values of strain the curves exhibited a flat plateau due to the densification of the structures. In addition, for strain above 20 %, the samples with and without shell show the same behavior.

During compression tests, for both the considered designs, the stress initially increases with increasing deformation up to a maximum value (45 MPa and 155 MPa for NS and S samples, respectively). This maximum load represents the ultimate strength (σM). This peak in stress is related to strain values of 5-6 % for both the investigated designs, even though the values of the maximum stress reached are significantly different. In fact, as reported in Table 5, the ultimate strength of NS lattices is 45 ± 2 MPa, which is approximately three times lower than 155 ± 5 MPa, demonstrated for the solid shell (S). The yield stress (σY) follows the same trend and is 35 ± 2 MPa and 119 ± 5 MPa for the NS and S samples, respectively.

After the peak, a marked drop in stress is observed for S samples, while for NS samples a smoother decrease of the stress that progressively reaches a plateau is recorded.

For NS samples, after the peak of stress, both plastic deformation and densification of the structure are noted. A stress plateau (from 8 % strain) continued until the end of the test (20 % strain). For S samples, the first evident drop-in stress is due to the failure of the shell structure. Afterward, for S samples, a plateau in stress between 8 % and 17 % strain was noted due to the densification of the structure. At 17 % strain S samples showed another drop in stress. After this, the stress-strain curves recorded for S and NS samples are comparable, indicating that in both cases only the lattice structure is supporting the load. This is demonstrated by the observation of samples after testing, as reported in Figure 6b-c-d. The S sample exhibits two different fracture modes. The first one shows a vertical fracture of the solid shell revealing the inner lattice (Fig. 6b). Moreover, a detachment of the solid shell from the lattice part along the edge and a densification of the lattice structure occurs. Specifically, the solid shell under compression is detached from the inner lattice due to the lattice expansion causing the collapse of the solid shell along the vertical direction. The second type of collapse mechanism for the S samples exhibits a fracture of the shell in the central part, and the detachment of the solid shell from the lattice part due to the lattice expansion (Fig. 6c). When the shell is detached from the lattice, it no longer contributes to support the structure and this explains the severe decrease in stress recorded, as visible in Figure 6a. The specimens tested under these conditions reached a remarkably high level of stress starting from the inner part. Therefore, the second load drop indicated the shell failure.

In addition, the orientation of the struts is crucial to understand how the lattice influences the mechanical response of the structure because they can work in compression or tensile mode giving different results. The BCC unit cell is characterized by struts inclined at 45° to the load direction. The compression load applied along the samples is divided into bending and compression components on each strut of the lattice. The lateral expansion of the lattice is due to the compression of the lattice contributing to the fracture and the detachment of the solid shell.

On the other hand, the NS samples present a 45° fracture mode (Fig. 6d) as expected for this lattice structure [41–43]. The struts, oriented along a diagonal axis, are subjected mainly to a bending load and the fracture occurs in that direction (45°) due to the geometry of the BCC unit cell. Contrarily to the S samples, the NS lattices bore the load entirely and the bending component on the struts caused the main fracture.

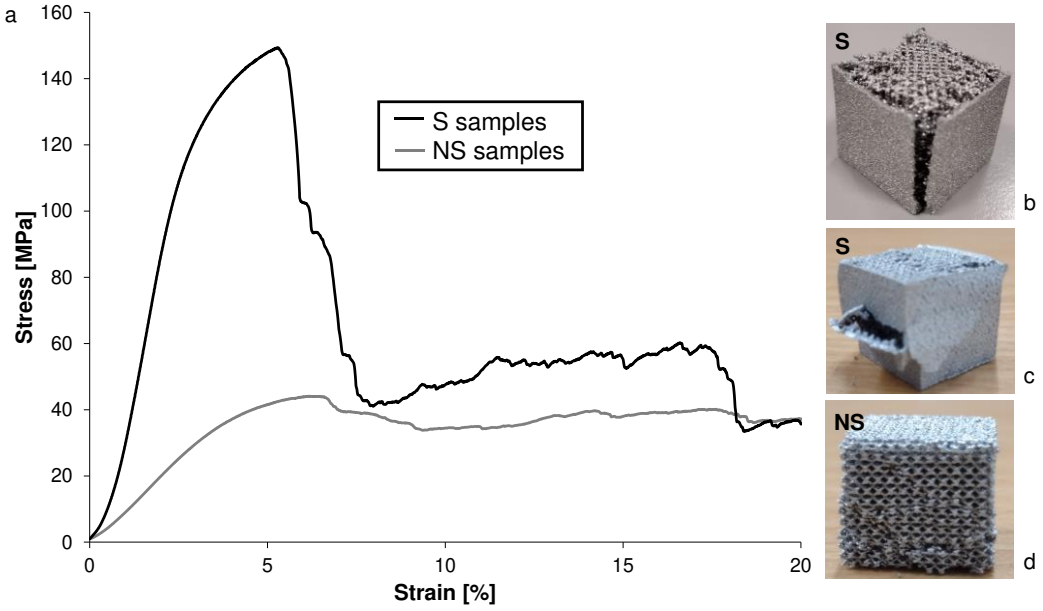

Figure 6: Stress-strain curves of: AB samples with and without solid shell. Main failure modes after compression test on the S samples with solid shell, and NS sample without solid shell.

The elastic modulus is calculated in the elastic region of curves shown in Figure 6 and it is reported in Table 5. The elastic modulus of the S and NS samples is 6.34 ± 0.34 GPa and 1.10 ± 0.03 GPa, respectively. Probably, the already mentioned porosities of these structures are relevant for the elastic properties, influencing the mechanical behavior.

Moreover, the energy absorption until σM and until the end of the test (20 % strain) was calculated and reported in Table 5. As expected, the lattices with solid shell absorb more energy when stressed, and exhibit a perfect elastoplastic behavior, able to reach higher deformations. The energy absorption (We) of the lattice with the solid shell is two times higher than the one without the solid part. In fact, the presence of an external solid shell is effective in increasing the general stiffness and the energy absorption of the structure.

Moreover, the mechanical results of S samples demonstrated to bear a high load suggesting aerospace applications in addition to biomedical ones. In particular, the reduced number of defects at the interface induced high stiffness and strength in the structures, bearing the load until the lattice core expanded in lateral directions making the contribution of the shell negligible.

Table 5: Results of the compression tests of S and NS samples.

Properties	S	NS
σM [MPa]	155 ± 5	45 ± 2
σY [MPa]	119 ± 5	35 ± 2
E [GPa]	6.34 ± 0.34	1.10 ± 0.03
WM [MJ/m³]	5.27 ± 1.03	1.83 ± 0.31
We [MJ/m³]	9.77 ± 0.65	4.93 0.15

Considering the mechanical behavior of S samples, a detachment of the shell from the lattice part was observed, indicating that fracture is taking place at the interface. This can be enhanced from the presence of localized

defects. From the microstructural analysis previously discussed (see paragraph 3.1 and 3.2), at the interface, the microstructure was not altered. In fact, the microstructure was homogeneous along the entire samples because the process parameters used were the same for both parts of the specimens. Moreover, the abrupt change in density did not affect the formation of α + β lamellar structure.

Therefore, to better understand the failure mechanism, especially the role played by the geometrical discontinuity at the interface between shell and lattice for S samples, FEM analysis was performed on S and NS specimens.

3.1.3.4 Finite Element Method Analysis

A first point that emerged from FEM analysis, as it can be seen from Table 6, is relative to the nominal lattice stiffness. In fact, the calculated value is much higher than the experimental measure. Specifically, the nominal lattice model predicts that ideal specimens should exhibit a stiffness more than twice that observed experimentally (a stiffness ratio of 2.25) for the NS design, and over three times for the S design (a stiffness ratio of 3.42). The S design showed a larger reduction across all models, most likely due to the shell being the dominant stiffness element and being less ideal than the other lattice elements (struts and nodes). This is evident when transitioning from the nominal to the average, and further to the worst-case scenario. In fact, the average model demonstrated considerably lower stiffness, with stiffness ratios of 1.77 and 1.85 for the NS and S designs, respectively. Interestingly, the worst-case scenario values closely aligned with experimental results, underscoring the importance of Young's modulus correction and the actual dimensions of struts and shell. The resulting Finite Element Method (FEM) moduli also closely match the values reported in [8].

Overall, the current model accounts primarily for average and homogenous effects, as it corrects the geometry in size but still represents an ideal shape of shells, struts, and nodes. Therefore, the remaining discrepancy between FEM and experimental values can be attributed to local defects, both in terms of porosities and other deviations from ideal geometry. These local defects can significantly affect the bending and shear stiffness of struts and the axial stiffness of the shell, playing a crucial role not only in lattice damage but also in the macroscopic linear-elastic behavior of the lattice. This behavior can be viewed as a complex interplay of elastic elements in series and parallel, where a local increase in elastic compliance can markedly alter the macroscopic elastic response. Therefore, adjusting the model geometry and material parameters below average values can be considered a method to account for this local stiffness deficit.

Table 6: Young modulus of the lattice calculated from FEM analyses of S and NS samples. Red values indicate the difference against the experimental measure.

Lattice type	Young modulus of the lattice structures [GPa]			
	FEM nominal	FEM average	FEM worst case	Experimental
NS	2.48 (+125%)	1.95 (+77%)	1.32 (+20%)	1.10±0.03
S	21.68 (+242%)	11.71 (+85%)	7.41 (+17%)	6.34±0.38

The associated stress state of the lattice structures is also shown in Figure 7 for a total applied displacement of 0.15 mm (corresponding to 0.005 mm over the modeled thickness). As expected, the geometrical discontinuity

at the interface between struts and the solid shell, known as the notch effect, served as a local stress raiser. This phenomenon is a primary factor contributing to the observed fracture behavior in NS samples, where detachment of the shell from the core lattice structure was observed.

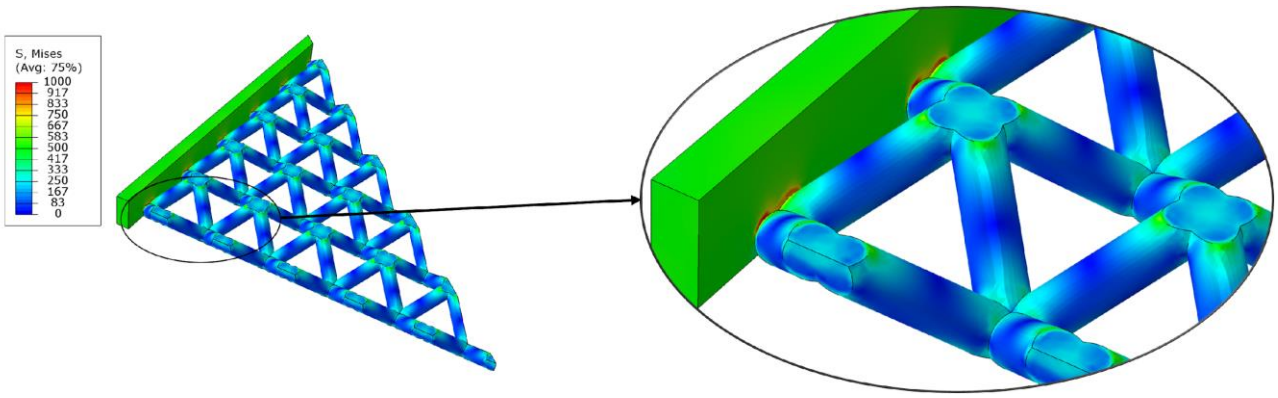

Figure 7: Von Mises stress maps for the worst-case variants. The model was mirrored to represent 1/8 of the total lattice cross-section and a complete layer (corresponding to a thickness of 2 mm).

3.1.3.5 Surface fracture Analysis

Representative SEM images of the fracture surface for the investigated samples are reported in Figure 8 for the strut (Fig. 8a-b) and shell (Fig. 8c-d). No evident differences were observed when comparing the fracture surfaces at the shell or the strut. In both cases, the fracture mechanism shown in Figure 8 clearly reports the ductile fracture of the samples, demonstrated by the presence of dimple-like structures.

The connection between the lattice part and the solid shell was crucial because of the important variation in size and geometry. As previously shown in Figure 6b, coarse defects were not detected on the interface due to the same process parameters set. Moreover, the fracture mechanism showed the same features on the lattice and solid shell. The detachment of the solid shell from the lattice part was due to the lattice expansion and to the geometry variation from the lattice (porous structure) to the solid part (shell).

The FEM analysis confirmed the mechanical behavior of the printed samples. The porosity was the main feature that influenced the stiffness of the samples, especially for the S samples. The high percentage (5 %) of porosity localized into the solid shell, especially in the center part, made the structure less stiff than the designed one (in accordance with the stiffness of Ti6Al4V) [2,44]. The lattice part exhibited porosity level in a range between 0.4 % and 0.6 %, not as influential as in the solid part.

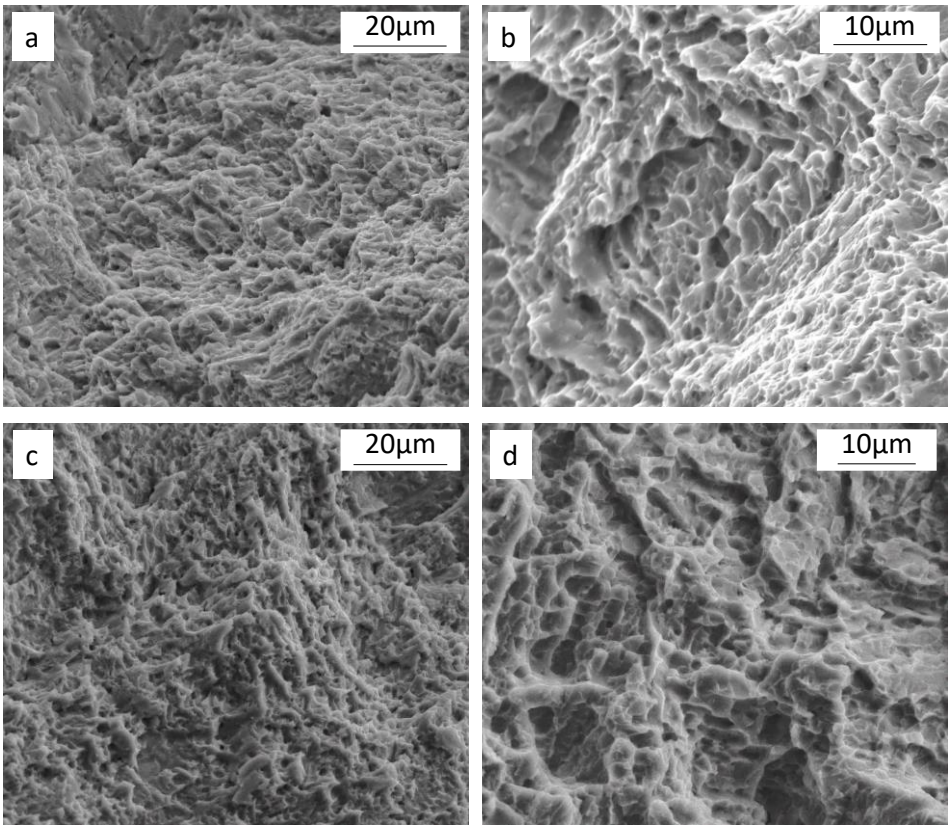

Figure 8: Representative SEM images of fracture mechanism of S samples on (a,b) the strut and (c,d) shell.

Conclusions

The present work provides a combined experimental and numerical analysis to investigate the compressive response of additively fabricated Ti6Al4V lattice structures with BCC unit cell, with (S) and without (NS) solid shell. The S and NS samples were manufactured at 90° build angle to the EB-PBF printing plate.

The main results presented in this work lead to the following conclusions:

- The process affects the morphology of the samples. In particular, the parameters of the electron beam made the solid shell irregular, probably due to a combination of the hatch spacing, the current, and the scan speed values. In fact, a relatively high porosity level of 5 % was detected in the shell, while a porosity level of 0,6 % of the struts and nodes cross-section was measured for both sets of samples.

- The ultimate strength of NS lattices is three times lower than that of the samples with the solid shell. The S samples absorb more energy than the NS lattice due to the presence of the solid shell. In fact, until the end of the compression test, the S samples absorb twice as much energy as the NS specimens. The presence of the solid shell results also in a higher stiffness of the samples (the S samples are 20 % stiffer than the NS ones).

- The yield stress is also influenced by the solid shell. The σY of S samples is 30 % higher than that of the NS samples. In general, the S samples exhibit perfect elastoplastic behavior, able to reach higher

deformations. The presence of an external solid shell is effective in increasing the general stiffness and the energy absorption of the structure.

- At the beginning of the tests, the solid shell of S samples mainly supports the load, and the lattice structure gives a minor contribution. After the detachment of the shell, the mechanical behavior of the S samples is the same as NS lattices, because the shell is separated from the lattice core, and it is no longer able to carry the load. In fact, from the 20 % of deformation, the curves become perfectly overlapped because the shell contribution becomes negligible.
- The FEM analysis reveals that the nominal lattice stiffness should be more than twice and three times that experimentally observed for the NS and S samples, respectively. This is mainly attributed to significant porosities and deviations from ideal geometry. The material parameters and geometry dimensions adjustments carried out for the worst-case scenario model led to a much better reproduction of the experimental stiffness. The FEM analysis for S samples also confirms that the connection between the struts and the solid shell is a critical point where high stresses are reached, leading to the detachment of the shell.
- Ductile fracture occurs for S and NS samples. In particular, S lattices exhibit first the fracture of the shell, due to the lateral expansion of the lattice and the detachment of the external shell from the lattice part. The NS lattice shows a 45° fracture as widely shown in literature. When the shell has been detached from the lattice core, the S and NS samples show the same mechanical behavior

To summarize, it emerged that the shell provides a positive contribution needed to better support the load in terms of maximum strength and energy absorption, especially for small deformations. On the other hand, more significant deformations of the structure lead to a concentration of stresses at the interface between the struts and the solid shell, resulting in the detachment of the shell itself. This has to be taken into account to design lattice structures properly and to exploit their potential, making it useful for many industrial applications. Considering the biomedical field, the structure of S samples can provide interconnected pores that facilitate tissue growth and development in the inner part and a solid shell that can support the whole structure. However, observing the results of the compression tests, the detachment of the shell must be analyzed for the validation of load-bearing application [45]. The results obtained in the present study can help to better understand the behavior of these structures as a function of the applied load.

Considering the results obtained for the S samples from the compression tests, the studied structures could be also used as space fillers or conformal parts for lightweight engineering, shock absorption, or heat exchangers in aerospace [46].

The key point is to find the best compromise between lightweight and reliability based on the application.

References

[1] Sepe R, De Luca A, Giannella V, Borrelli R, Franchitti S, Di Caprio F, et al. Influence of dimension, building position, and orientation on mechanical properties of EBM lattice Ti6Al4V trusses. International Journal of Advanced Manufacturing Technology 2022;122:3183–98. https://doi.org/10.1007/s00170-022-10051-3.

[2] Grazia Guerra M, Lafirenza M, Errico V, Angelastro A. In-process dimensional and geometrical characterization of laser-powder bed fusion lattice structures through high-resolution optical tomography. Opt Laser Technol 2023;162:109252. https://doi.org/10.1016/j.optlastec.2023.109252.

[3] Lin Y, Shi W, Li J, Liu Y, Liu S, Li J. Evaluation of mechanical properties of Ti–6Al–4V BCC lattice structure with different density gradient variations prepared by L-PBF. Materials Science and Engineering A 2023;872:144986. https://doi.org/10.1016/j.msea.2023.144986.

[4] Sajjad R, Chauhdary ST, Anwar MT, Zahid A, Khosa AA, Imran M, et al. A review of 4D printing – Technologies, shape shifting, smart polymer based materials, and biomedical applications. Advanced Industrial and Engineering Polymer Research 2023. https://doi.org/10.1016/j.aiepr.2023.08.002.

[5] Masood Arif Bukhari S, Husnain N, Arsalan Siddiqui F, Tuoqeer Anwar M, Abbas Khosa A, Imran M, et al. Effect of laser surface remelting on Microstructure, mechanical properties and tribological properties of metals and alloys: A review. Opt Laser Technol 2023;165. https://doi.org/10.1016/j.optlastec.2023.109588.

[6] Liu S, Shin YC. Additive manufacturing of Ti6Al4V alloy: A review. Mater Des 2019;164:107552. https://doi.org/10.1016/j.matdes.2018.107552.

[7] Lazar PJL, Subramanian J, Manickam M, Selvaraj VK. Imperfections and computational modeling of lattice structures developed through powder bed fusion - A short review. Mater Today Proc 2023:2–7. https://doi.org/10.1016/j.matpr.2023.02.269.

[8] Cheng XY, Li SJ, Murr LE, Zhang ZB, Hao YL, Yang R, et al. Compression deformation behavior of Ti-6Al-4V alloy with cellular structures fabricated by electron beam melting. J Mech Behav Biomed Mater 2012;16:153–62. https://doi.org/10.1016/j.jmbbm.2012.10.005.

[9] Onuike B, Bandyopadhyay A. Additive manufacturing of Inconel 718 – Ti6Al4V bimetallic structures. Addit Manuf 2018;22:844–51. https://doi.org/10.1016/j.addma.2018.06.025.

[10] Sidambe AT. Biocompatibility of advanced manufactured titanium implants-A review. Materials 2014;7:8168–88. https://doi.org/10.3390/ma7128168.

[11] Sajjad U, Rehman T ur, Ali M, Park CW, Yan WM. Manufacturing and potential applications of lattice structures in thermal systems: A comprehensive review of recent advances. Int J Heat Mass Transf 2022;198:123352. https://doi.org/10.1016/j.ijheatmasstransfer.2022.123352.

[12] Pathania A, Subramaniyan AK, Nagesha BK. Influence of post-heat treatments on microstructural and mechanical properties of L-PBF-processed Ti6Al4V alloy. Progress in Additive Manufacturing 2022;7:1323–43. https://doi.org/10.1007/s40964-022-00306-6.

[13] Popov V V., Muller-Kamskii G, Kovalevsky A, Dzhenzhera G, Strokin E, Kolomiets A, et al. Design and 3D-printing of titanium bone implants: brief review of approach and clinical cases. Biomed Eng Lett 2018;8:337–44. https://doi.org/10.1007/s13534-018-0080-5.

[14] Zhang XZ, Tang HP, Wang J, Jia L, Fan YX, Leary M, et al. Additive manufacturing of intricate lattice materials: Ensuring robust strut additive continuity to realize the design potential. Addit Manuf 2022;58:103022. https://doi.org/10.1016/j.addma.2022.103022.

[15] Hernández-Nava E, Smith CJ, Derguti F, Tammas-Williams S, Leonard F, Withers PJ, et al. The effect of defects on the mechanical response of Ti-6Al-4V cubic lattice structures fabricated by electron beam melting. Acta Mater 2016;108:279–92. https://doi.org/10.1016/j.actamat.2016.02.029.

[16] Suard M, Martin G, Lhuissier P, Dendievel R, Vignat F, Blandin JJ, et al. Mechanical equivalent diameter of single struts for the stiffness prediction of lattice structures produced by Electron Beam Melting. Addit Manuf 2015;8:124–31. https://doi.org/10.1016/j.addma.2015.10.002.

[17] Huang Y, Wan ARO, Schmidt K, Sefont P, Singamneni S, Chen ZW. Effects of cell orientation on compressive behaviour of electron beam powder bed fusion Ti6Al4V lattice structures. Mater Today Proc 2023:0–4. https://doi.org/10.1016/j.matpr.2023.04.522.

[18] Güden M, Alpkaya AT, Hamat BA, Hızlı B, Taşdemirci A, Tanrıkulu AA, et al. The quasi-static crush response of electron-beam-melt Ti6Al4V body-centred-cubic lattices: The effect of the number of cells, strut diameter and face sheet. Strain 2022;58:1–20. https://doi.org/10.1111/str.12411.

[19] Novak N, Kytyr D, Rada V, Doktor T, Al-Ketan O, Rowshan R, et al. Compression behaviour of TPMS-filled stainless steel tubes. Materials Science and Engineering A 2022;852:143680. https://doi.org/10.1016/j.msea.2022.143680.

[20] Xiong Y, Wang W, Gao R, Zhang H, Dong L, Qin J, et al. Fatigue behavior and osseointegration of porous Ti-6Al-4V scaffolds with dense core for dental application. Mater Des 2020;195:108994. https://doi.org/10.1016/j.matdes.2020.108994.

[21] Fu J, Ding J, Qu S, Zhang L, Wang MY, Fu MW, et al. Improved light-weighting potential of SS316L triply periodic minimal surface shell lattices by micro laser powder bed fusion. Mater Des 2022;222. https://doi.org/10.1016/j.matdes.2022.111018.

[22] Dong G, Tang Y, Li D, Zhao YF. Design and optimization of solid lattice hybrid structures fabricated by additive manufacturing. Addit Manuf 2020;33:101116. https://doi.org/10.1016/j.addma.2020.101116.

[23] Bertol LS, Júnior WK, Silva FP da, Aumund-Kopp C. Medical design: Direct metal laser sintering of Ti-6Al-4V. Mater Des 2010;31:3982–8. https://doi.org/10.1016/j.matdes.2010.02.050.

[24] WANG C, ZHU J, WU M, HOU J, ZHOU H, MENG L, et al. Multi-scale design and optimization for solid-lattice hybrid structures and their application to aerospace vehicle components. Chinese Journal of Aeronautics 2021;34:386–98. https://doi.org/10.1016/j.cja.2020.08.015.

[25] Cantaboni F, Ginestra PS, Tocci M, Avanzini A, Ceretti E, Pola A. Compressive behavior of Co-Cr-Mo radially graded porous structures under as-built and heat-treated conditions. Frattura Ed Integrita Strutturale 2022;16:490–504. https://doi.org/10.3221/IGF-ESIS.62.33.

[26] Parthasarathy J, Starly B, Raman S, Christensen A. Mechanical evaluation of porous titanium (Ti6Al4V) structures with electron beam melting (EBM). J Mech Behav Biomed Mater 2010;3:249–59. https://doi.org/10.1016/j.jmbbm.2009.10.006.

[27] Ginestra P, Ferraro RM, Zohar-Hauber K, Abeni A, Giliani S, Ceretti E. Selective laser melting and electron beam melting of Ti6Al4V for orthopedic applications: A comparative study on the applied building direction. Materials 2020;13:1–23. https://doi.org/10.3390/ma13235584.

[28] Roberts AP, Garboczi EJ. Elastic properties of model porous ceramics. Journal of the American Ceramic Society 2000;83:3041–8. https://doi.org/10.1111/j.1151-2916.2000.tb01680.x.

[29] Morrissey LS, Nakhla S. A Finite Element Model to Predict the Effect of Porosity on Elastic Modulus in Low-Porosity Materials. Metall Mater Trans A Phys Metall Mater Sci 2018;49:2622–30. https://doi.org/10.1007/s11661-018-4623-2.

[30] Kan WH, Gao M, Zhang X, Liang E, Chiu NSL, Lim CVS, et al. The influence of porosity on Ti-6Al-4V parts fabricated by laser powder bed fusion in the pursuit of process efficiency. International Journal of Advanced Manufacturing Technology 2022;119:5417–38. https://doi.org/10.1007/s00170-021-08374-8.

[31] Montalbano T, Briggs BN, Waterman JL, Nimer S, Peitsch C, Sopcisak J, et al. Uncovering the coupled impact of defect morphology and microstructure on the tensile behavior of Ti-6Al-4V fabricated via laser powder bed fusion. J Mater Process Technol 2021;294:117113. https://doi.org/10.1016/j.jmatprotec.2021.117113.

[32] Persenot T, Burr A, Martin G, Buffiere JY, Dendievel R, Maire E. Effect of build orientation on the fatigue properties of as-built Electron Beam Melted Ti-6Al-4V alloy. Int J Fatigue 2019;118:65–76. https://doi.org/10.1016/j.ijfatigue.2018.08.006.

[33] Bellini C, Borrelli R, Di Caprio F, Di Cocco V, Franchitti S, Iacoviello F, et al. An Innovative Method to Analyse the Geometrical Accuracy of Ti6Al4V Octet-Truss Lattice Structures. Materials 2023;16:2372. https://doi.org/10.3390/ma16062372.

[34] Kirchner A, Klöden B, Weißgärber T, Kieback B. Powders for Additive Manufacturing. n.d.

[35] Rafi HK, Karthik N V., Gong H, Starr TL, Stucker BE. Microstructures and mechanical properties of Ti6Al4V parts fabricated by selective laser melting and electron beam melting. J Mater Eng Perform 2013;22:3872–83. https://doi.org/10.1007/s11665-013-0658-0.

[36] Neils A, Dong L, Wadley H. The small-scale limits of electron beam melt additive manufactured Ti-6Al-4V octet-truss lattices. AIP Adv 2022;12. https://doi.org/10.1063/5.0094155.

[37] Cao X, Carter LN, Villapún VM, Cantaboni F, De Sio G, Lowther M, et al. Optimisation of single contour strategy in selective laser melting of Ti-6Al-4V lattices. Rapid Prototyp J 2022;28:907–15. https://doi.org/10.1108/RPJ-04-2021-0103.

[38] Everhart W, Dinardo J, Barr C. The Effect of Scan Length on the Structure and Mechanical Properties of Electron Beam-Melted Ti-6Al-4V. Metall Mater Trans A Phys Metall Mater Sci 2017;48:697–705. https://doi.org/10.1007/s11661-016-3866-z.

[39] Collins PC, Welk B, Searles T, Tiley J, Russ JC, Fraser HL. Development of methods for the quantification of microstructural features in α + β-processed α/β titanium alloys. Materials Science and Engineering A 2009;508:174–82. https://doi.org/10.1016/j.msea.2008.12.038.

[40] Tiley J, Searles T, Lee E, Kar S, Banerjee R, Russ JC, et al. Quantification of microstructural features in α/β titanium alloys. Materials Science and Engineering A 2004;372:191–8. https://doi.org/10.1016/j.msea.2003.12.008.

[41] Cantaboni F, Ginestra PS, Tocci M, Avanzini A, Ceretti E, Pola A. Compressive behavior of Co-Cr-Mo radially graded porous structures under as-built and heat-treated conditions. Frattura Ed Integrita Strutturale 2022;16:490–504. https://doi.org/10.3221/IGF-ESIS.62.33.

[42] Distefano F, Guglielmino E, Mineo R, Epasto G. Mechanical and morphological characterization of BCC - Derived unit cells for biomedical devices. Procedia Structural Integrity 2022;41:470–85. https://doi.org/10.1016/j.prostr.2022.05.053.

[43] Sokollu B, Gulcan O, Konukseven EI. Mechanical properties comparison of strut-based and triply periodic minimal surface lattice structures produced by electron beam melting. Addit Manuf 2022;60:103199. https://doi.org/10.1016/j.addma.2022.103199.

[44] Hrabe N, Quinn T. Effects of processing on microstructure and mechanical properties of a titanium alloy (Ti-6Al-4V) fabricated using electron beam melting (EBM), part 1: Distance from build plate and part size. Materials Science and Engineering A 2013;573:264–70. https://doi.org/10.1016/j.msea.2013.02.064.

[45] Kladovasilakis N, Tsongas K, Tzetzis D. Finite element analysis of orthopedic hip implant with functionally graded bioinspired lattice structures. Biomimetics 2020;5. https://doi.org/10.3390/BIOMIMETICS5030044.

[46] Bici M, Brischetto S, Campana F, Ferro CG, Seclì C, Varetti S, et al. Development of a multifunctional panel for aerospace use through SLM additive manufacturing. Procedia CIRP, vol. 67, Elsevier B.V.; 2018, p. 215–20. https://doi.org/10.1016/j.procir.2017.12.202.

3.2 Optimisation of Single Contour Strategy in Selective Laser Melting of Ti-6Al-4V Lattices

3.2.1 INTRODUCTION

Demand for orthopaedic implant surgery is predicted to exceed 5 million worldwide by 2021 with up to $65 billion in revenues estimated by 2025 (Murr, 2020). The freedom in design inherent to metal Additive Manufacturing (AM) and the expected rise in demand is stimulating research to add further functional properties to implantable devices boosting their application in medicine. In load-bearing implants, latticed structures have the potential to mimic the mechanical response of bone, reducing the stress shielding effect and limiting implant loosening (Hedayati *et al.*, 2018). These porous structures also have the potential to improve cell adhesion and osseointegration, thus strengthening the mechanical bond between patient and implant (Deing *et al.*, 2014, Maietta *et al.*, 2019). Consequently, when applied correctly to bone and tissue scaffolds, titanium AM lattice structures have the potential to meet their fundamental requirements, namely: biocompatibility; surfaces suitable for cell attachment; interconnected porosity enabling cell ingrowth, transport of nutrients, and release of waste; and mechanical properties matching surrounding tissue (Wang *et al.*, 2016). It has been demonstrated that unit cell design and pore size influence cell proliferation during in-vivo studies (Markhoff *et al.*, 2015, Li *et al.*, 2020) with research by Van Bael et al. concluding that graded pore sizes in tissue scaffolds may promote initial cell attachment within fine pores developing in to tissue growth without occlusion as pore size coarsens (Van Bael *et al.*, 2012). Significant interest in this topic has prompted comprehensive reviews (Wang *et al.*, 2016, Wang *et al.*, 2017b) and the creation of design libraries to aid unit cell selection in tissue scaffolds(Chantarapanich *et al.*, 2012). Finally, potential novel applications include the use of lattices as reservoirs to deliver antibiotics, growth factors, or other treatments directly to the implant site and MRI artefact mitigation (Burton *et al.*, 2019, Carter *et al.*, 2020). Nevertheless, in order to exploit these benefits, accuracy, predictability, and consistency of lattice production must be ensured.

Selective Laser Melting (SLM) is an AM technology whereby fully dense components are produced via layer-by-layer laser melting of metallic powder (Shipley *et al.*, 2018, Mullen *et al.*, 2009, Koptyug *et al.*, 2013). With a relatively high resolution and without traditional machining constraints, SLM presents a suitable method for production of components with integrated lattices. Part performance depends on the physicochemical properties of the powder feedstock and the SLM processing parameters. Powder quality is typically determined by supplier specification, however, process parameters may be directly assigned by the SLM operator, heavily influencing the final part (Trevisan *et al.*, 2017). Laser power and scan speed represent two key process inputs (Song *et al.*, 2012, Nguyen *et al.*, 2020, Maamoun *et al.*, 2018) which control both melt pool size and shape further determining dimensional accuracy, microstructure, mechanical properties, and surface quality (Großmann *et al.*, 2019, Kusuma *et al.*, 2017). Energy density, E (J/mm) as defined in Equation 1, combines these inputs to provide a simplified variable which may be useful in understanding certain behaviours (Yusuf and Gao, 2017, Kusuma *et al.*, 2017):

$$\boldsymbol{E} = \frac{\boldsymbol{P}}{\boldsymbol{V}} \text{ J/mm,} \qquad \text{Equation 1}$$

Where P is laser power (W) and v represents scan speed (mm/s).

The effect of E, P, and v on surface roughness, porosity, and accuracy have been widely reported and trends linking process parameters to part quality identified (Hong *et al.*, 2016, Wang *et al.*, 2017a, Khorasania *et al.*, 2019). Researchers have previously shown that increasing laser energy density and build angle induces greater surface roughness (Wang *et al.*, 2017a, Qin and Chen, 2013, Villapún *et al.*, 2020), however, special care has been taken to understand the role of these inputs in internal porosity and defect type (Salem *et al.*, 2019). Porosity from trapped or evaporated gas in powder feedstock occurred at low scanning speed around 800 mm/s, while keyhole porosity is reportedly dominant at higher energy density conditions corresponding to a deep melt pool. Other reported defects include irregular and spherical shapes at high scan speed (2400-4000 mm/s) and lower laser power (100-300 W) due to melt track balling and lack of fusion. These results have been further supported by the work of Qiu et al. (Qiu *et al.*, 2015), although discrepancies on the optimal processing window can be found in the literature. This is highlighted by Gu et al. who showed internal porosity variations from 0% to 5.4% under a fixed "optimal" energy density (61 J/mm3) by changing laser power and scan speed, suggesting that whilst energy density may be useful in some cases, the influence of individual parameters should not be overlooked (Gu *et al.*, 2013).

When processing fine lattice structures, strut thickness has been shown to significantly deviate from the initial CAD design. Yan et al. revealed up to 90 μm discrepancies with lattice strut design diameters between 420 μm and 610 μm (Yan *et al.*, 2014). This was confirmed by bulk analysis showing printed lattices being denser (10.66% and 13.12%) than the design (10% and 12%), which would lead to inconsistencies in mechanical properties between design and final part. A similar study found a linear relationship between lattice strut thickness and energy density with limited to no influence caused by scan strategy, build angle, or material, resulting in an increase in Young's modulus (Ghouse *et al.*, 2017). On the other hand, the work of Onal et al. suggests that these discrepancies in design rise with exposure time and laser power that subsequently stabilised for energy inputs above 0.5 J for produced lattices via a single point exposure scan strategy (Onal *et al.*, 2019). The reported mismatch between design and manufactured geometry in these intricate structures is further complicated by the pre-processing software logic used to generate the laser path for each strut slice (Figure 1). The typical laser path for 250 μm strut slices shown in Figure 1b and 1f illustrates a 12% difference in energy input of neighbouring 'design identical' struts due to infill path planning. Additionally, scan spot placement between 'design identical' struts for both 150 μm and 350 μm show differences (Figure 1c and 1d). These inconsistencies between identically designed struts are likely to result in manufacturing inhomogeneities within a uniform lattice design. In contrast, the unfilled scan, figure 1a, shows consistent scan spots and path between adjacent struts (Figure 1e) for all diameters presenting a potentially more reliable method for lattice manufacture.

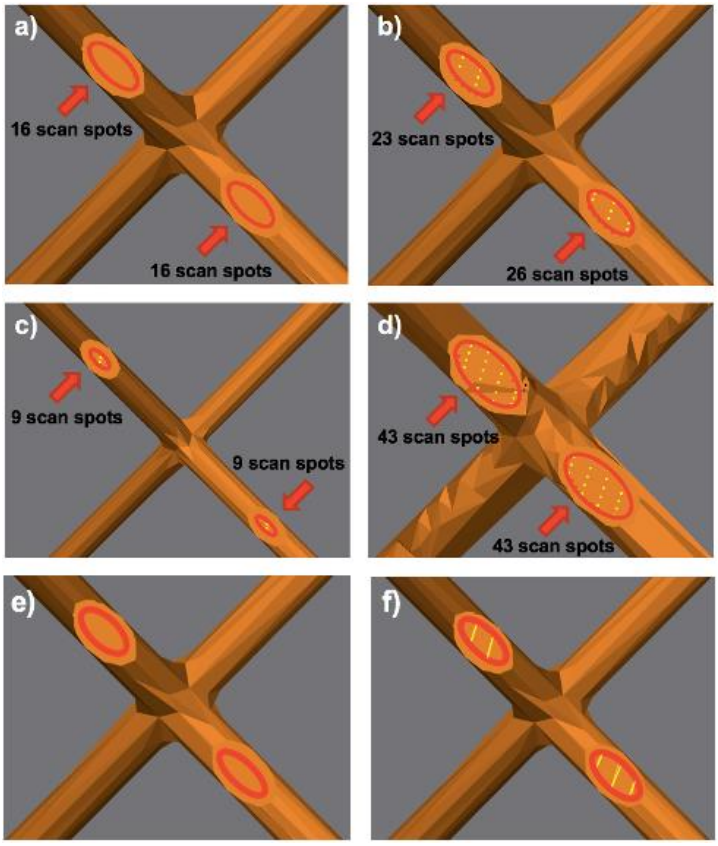

Figure 1. Images showing different number of scan spots in (a) SC and (b) SC+F strategies for designed struts size of 250 µm; (c) and (d) number of SC+F scan spots for 150 µm and 350 µm strut sizes; (e) scan path for SC scan; (f) scan path for SC+F. Red ellipsis represent border contours while yellow lines represent hatch (filling) scan.

In this paper, the accuracy of two scanning strategies, Single Contour (SC) (Figure 1e) and Single Contour plus Fill (SC+F) (Figure 1f), to manufacture SLM Ti-6Al-4V metal lattices was compared. during the manufacturing. Critical parameters, laser power and scan speed, were varied and lattice reproducibility, and integrity evaluated to determine an optimal processing window. Herein SC is revealed as a novel processing method with the potential to improve lattice accuracy of AM medical devices.

3.2.2 Materials and methods

3.2.2.1 Materials and Specimen manufacturing

Diamond unit cell lattices were selected for their adaptability in the biomedical field and manufacturability by SLM as shown in multiple studies (Ahmadi *et al.*, 2014, Li *et al.*, 2020, Derby, 2012, Heinl *et al.*, 2008). All cuboidal designs measured 20 x 20 x 20 mm with 1 mm unit cell (Figure 2a). CAD geometry was generated using nTopology Element (nTopology Inc., 1.25.0) design software, and exported as standard tessellation files (*.stl). (Nickels, 2020).

All specimens were fabricated using plasma atomised, Grade 23 Ti-6Al-4V powder (15 – 53 µm particle diameter) (LPW Technology Ltd., UK) via a RenAM 500 M (Renishaw, UK) SLM system. The RenAM 500 M utilizes a modulated laser system whereby the laser operates point-wise for a fixed exposure time and point

distance. Thus, scanning speed is defined as point distance/exposure time. Point distance was set at a constant 45 µm with scan speed varied using exposure time. All samples were produced under argon atmosphere using a pre-heated substrate at 170°C and 30 µm layer thickness.

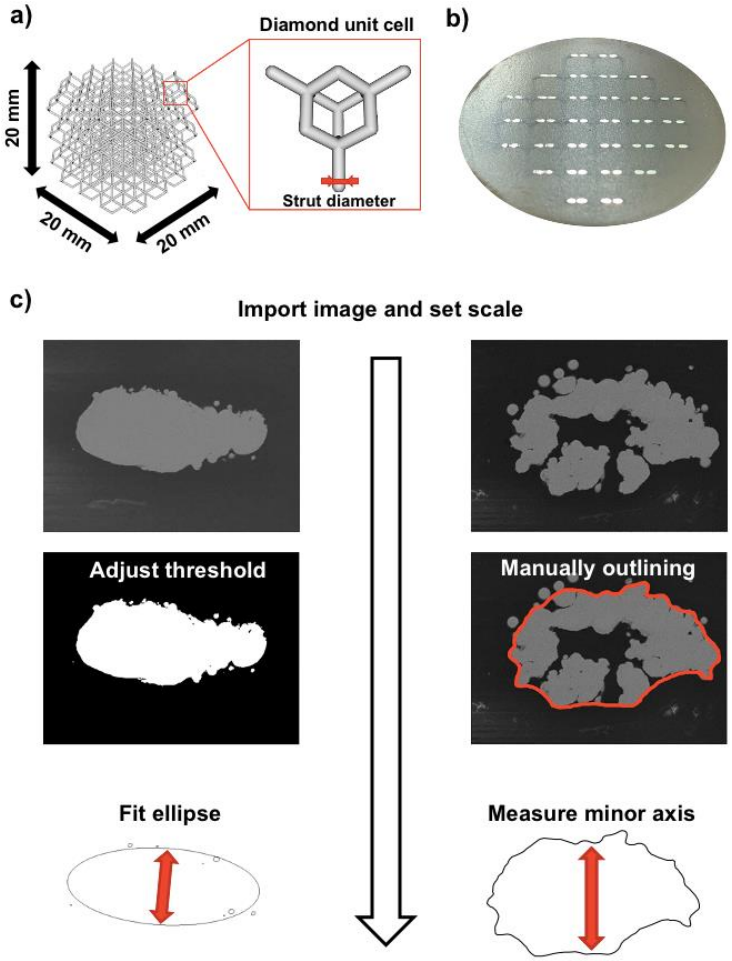

Figure 2. Images showing (a) the cuboidal and diamond unit cell design selected, (b) an example of cold-mounted and polished lattice and (c) a flow chart illustrating the contouring strategies used to measure strut diameter.

3.2.2.2 Design of Experiment

Two studies were performed. Within the first (Table I), SC specimens were produced with varying laser powers (50-150 W), scanning speeds (750-2250 mm/s) and strut diameters (150 µm, 250 µm and 350 µm). SC+F specimens were manufactured for the midpoint conditions, using 100 W and 1125 mm/s.

Table 1 DoE for the Comparison of SC and SC 1 F scan strategy

Scan speed	Scan speed (mm/s)	Exposure time (ms)	Energy density (J/mm)	Scan strategy
100	1125	40	0.089	SC+F
50	2250	20	0.022	SC
	1125	40	0.044	
	750	60	0.067	
100	2250	20	0.044	SC
	1125	40	0.089	
	750	60	0.133	
150	2250	20	0.067	SC
	1125	40	0.133	
	750	60	0.200	

The result of the first parametric analysis were used to develop a second study to better characterise the occurrence of porosity and dimensional accuracy (Table II). These parameters were selected to improve the resolution of the process window near the boundary between porous/fully dense lattices and successful/failed lattices of 250 μm strut diameter structures.

Table 2 Combination of parameters selected to evaluate the parametric effects on internal porosity of 250mm lattice manufactured by SC

Laser Power (W)	Scan speed (mm/s)	Exposure time (μs)	Energy density (J/mm)
50	1,250	36	0.040
	1,000	45	0.050
	750	60	0.067
70	1,750	26	0.040
	1,500	30	0.047
	1,250	36	0.056
	1,000	45	0.070
90	2,250	20	0.040
	2,100	21	0.043
	1,750	26	0.051
	1,500	30	0.060
	1,250	36	0.072
	1,000	45	0.090
100	2,250	20	0.044
	1,125	40	0.089
105	2,250	20	0.047
	2,100	21	0.050
	1,750	26	0.060
	1,500	30	0.070
	1250	36	0.084
115	2,250	20	0.051
	2,100	21	0.055
	1,750	26	0.066
150	2,250	20	0.067

3.2.2.3 Specimen Preparation

Fabricated specimens were cut from the build substrate by Wire EDM, cleaned in a water bath to remove excess powder, air dried, and cold-mounted in resin (VersoCit-2 Powder, Struers Aps, Denmark). Samples were ground progressively from 220 to 4000 grit (Struers Aps, Denmark) With a final polishing performed using an activated Op-s suspension (Struers Aps, Denmark). Micrographs of 20 strut cross sections (Figure 2b) for each sample were captured using a Scanning Electronic Microscope (SEM, Hitachi TM3000, Japan) in backscattered (BSE) mode.

3.2.2.4 Image Analysis and Process Mapping

Micrographs were analysed with ImageJ (NIH, USA., 1.53a) (Schneider *et al.*, 2012). As shown in Figure 2c, strut contour was initially defined by an appropriate global threshold or via manual outline for fragmented sections. For both methods, the boundary included any internal pore areas. Individual struts within the lattice built at an angle of 54° resulting in an elliptical cross-section, thus, strut diameter was determined as the minor axis of a fit ellipse. Internal porosity was calculated as the total hollow area within struts divided by the total cross section area for all 20 struts in each sample. Process contour maps were plotted using MATLAB R2018b 9.5.0.944444 (MathWorks Inc. USA).

3.2.3 Results and discussions

3.2.3.1 SC and SC+F comparison

Figure 3a compares mean strut thickness between SC and SC+F strategies for identical processing parameters (100 W, 1125 mm/s). SC+F strut diameter are on average 7% greater than those of SC for all sizes. Both SC and SC+F show a fully dense core for 150 μm and 250 μm struts, however greater diameters reveal the inability of the SC strategy to produce fully dense struts (Figure 3b) . This comparison demonstrates the feasibility of using SC as a method for producing fully dense thin lattice struts below a certain diameter. Nevertheless, the obtained geometric accuracy is relatively low with errors of 3.5%, -12.6% and -7.4% for 150 μm, 250 μm and 350 μm, respectively.

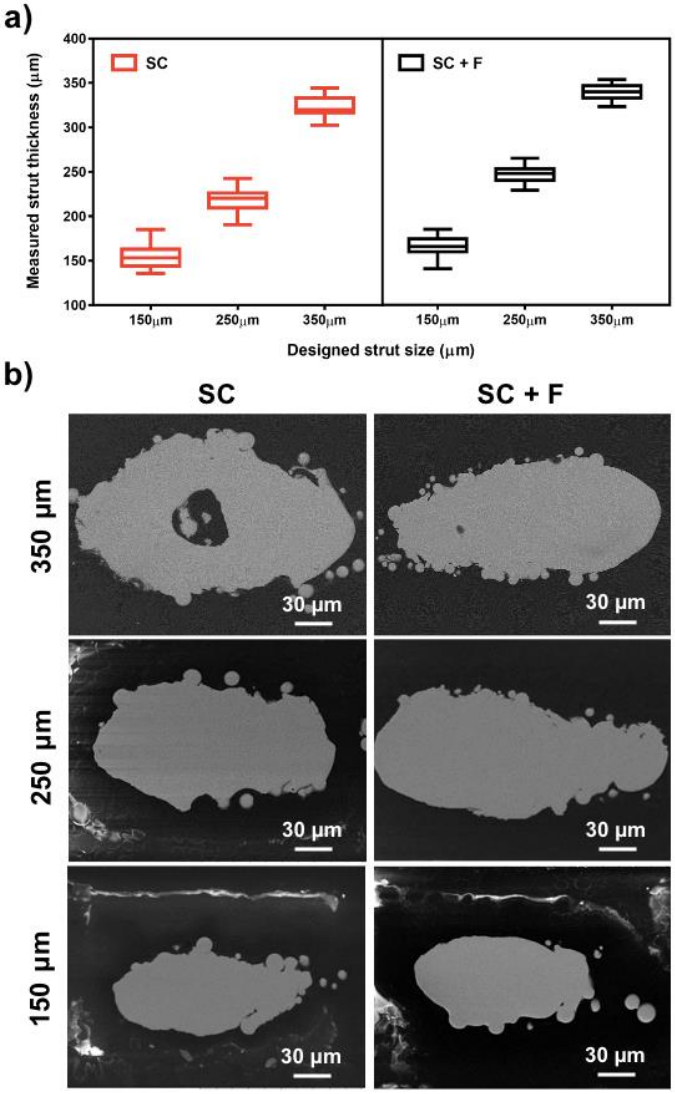

Figure 3. Comparison between SC and SC+F scan strategy under same processing parameters (laser power 100 W, scan speed 1125 mm/s): (a) strut thickness range for designed value of 150 μm, 250 μm and 350 μm; (b) SEM images showing different internal morphology under three designed strut thickness.

Previous studies have demonstrated that energy input influences melt pool width, directly relating it to strut thickness regardless of scan strategy used (Ghouse *et al.*, 2017, Onal *et al.*, 2019). SC+F produces greater energy input per strut than SC, even showing different energy input for adjacent struts; as illustrated in Figure 1b,1c, and 1d. The relatively limited conductive heat flow afforded by thin lattice struts results in a local thermal build-up during laser exposure whereby surplus energy simply drives up the melt pool width. In this scenario, final strut diameter is disproportionately driven by energy input as illustrated in the 150 μm struts where mean strut thicknesses are 155.2 μm and 165.7 μm for SC and SC+F respectively. Additionally, the previously highlighted differences in energy input between adjacent struts for the SC+F scan strategy are likely to induce further geometric inconsistencies. A similar phenomena was reported by Rashid et al. comparing single and double hatch scan (Rashida *et al.*, 2017) with thicker struts manufactured by double hatch scan due to the increase in energy input on each layer compared to single hatch scan. It should be noted however that the potential advantages of SC lattice production are limited by strut diameter. Above a threshold diameter, energy input and

corresponding melt pool width become insufficient to produce a fully dense strut and internal porosity remains following processing as highlighted in the 350 μm SC sample in Figure 3b. Thus, it is clear that it is necessary to analyse the processing window of this scan strategy.

Processing maps indicating strut condition of lattices produced using SC are shown in Figure 4a-c. For the 150 μm strut diameter lattices, most parameters produced a fully dense material, nevertheless, manufacturing failed for 50 W, 1125 mm/s and 2250 mm/s due to insufficient energy input to form a stable structure (Figure 4a). Occurrence of internal porosity increased with strut diameter as revealed by the shift in solid core areas observed in 250 μm samples (Figure 4b) and 350 μm samples (Figure 4c). Corresponding pore fraction by cross-section area also increased with strut diameter from ~1.6% to ~27.3% for 250 μm and 350 μm lattice respectively (Figure 4b and 4c insets). Likewise the occurrence of porosity decreases with increasing energy density as demonstrated in the 350 μm specimens (Figure 4c) where the only fully dense struts occurred under greatest energy density (150 W and 750 mm/s – 1125 mm/s). This highlights that internal morphology of SC manufactured lattices is highly dependent on both strut thickness and processing parameters.

A strong linear relationship ($R2 \geq 0.97$) between the energy density and resulting lattice strut diameter for each design strut thickness is shown in Figure 4d. This further confirms that, at these scales, process parameters as much as laser path govern the resulting geometry and careful control is essential for accurate lattice production. Single point exposure investigations have previously yielded positive results for lattice production showing the link between energy input and strut diameter (Mullen *et al.*, 2009, Onal *et al.*, 2019, Yan *et al.*, 2012). The SC strategy builds on this combining the control of both laser path and melt pool size via process parameter optimisation but eliminating the inconsistencies brought by hatch-filling.

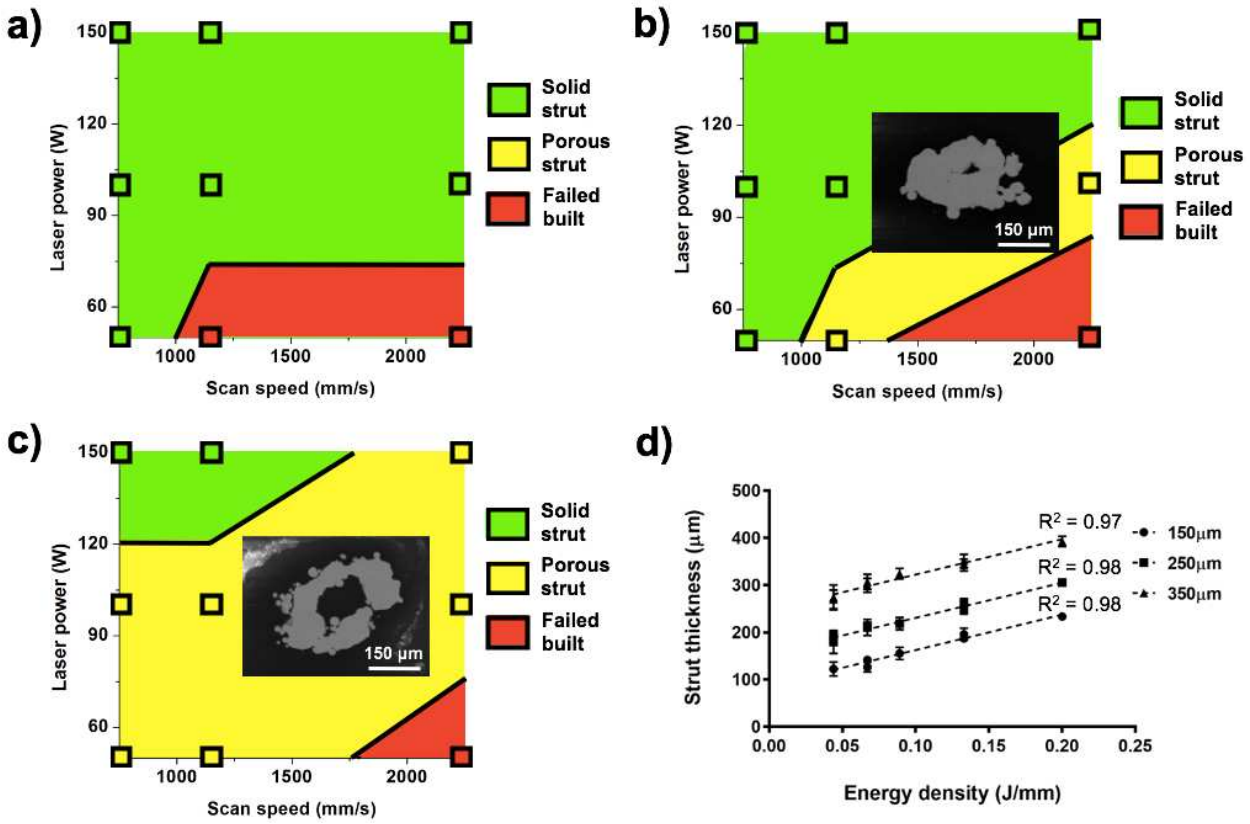

Figure 4. Parametric maps for strut thickness of (a) 150 µm, (b) 250 µm and (c) 350 µm, (a)-(c), where green areas represent struts built with solid core, yellow areas struts built with hollow structures and red areas unsuccessful built with SEM details showing the variation of hole area; and (d) correlation between energy density and strut thickness.

Other research has confirmed that increasing energy density raises melt pool width (Qiu *et al.*, 2015) which can be used to control the final strut diameter for a given SC laser path. To produce fully dense struts however, the melt pool width, and in turn the energy density, should be sufficient to melt the centre of each strut for a given laser path. A simplified geometric interpretation suggests that the smallest melt pool diameter needed to produce a fully dense strut is equal to the diameter of the laser path. This would produce a strut of diameter equal to approximately twice that of the melt pool. This relationship combined with process mapping may allow the input parameters themselves to act as the fine control for predictable geometric accuracy and strut integrity of SC processed lattices.

3.2.3.2 Processing window of SC manufactured samples

To improve and investigate the accuracy of this process mapping method, a further study was carried out using 250 µm strut diameter SC lattices. Process parameters near the solid/porous boundary were selected to accurately map this interface (Figure 5a). Internal porosity was revealed to be highly dependent on the energy density (Figure 5b), with hollow regions occupying 1.18% to 2.51% of the total area for values below 0.056 J/mm. As energy density increased from 0.056 J/mm to 0.089 J/mm, the corresponding porosity decreased, with fully dense struts obtained where energy density was greater than 0.089 J/mm. Significant porosity was observed under low laser powers and high scan speeds (Figure 5c). This results from the limited energy transferred, either due to low input energy overall or the brief laser/bed interaction time, reducing melt pool diameter. Nevertheless,

there was no direct correlation between porosity and either laser power or scanning speed, suggesting a combination of both parameters as the main driver of the observed trends (Figure 5c).

This expanded study reveals that the relationship between energy density and accuracy follows a convex unimodal trend with the minimum located at ~0.1 J/mm, resulting in standard error below 0.1% and fully dense struts (figure 5d). Furthermore, discrepancy between design and actual strut diameter is minimised at 0.1 J/mm (150 W, 1500 mm/s). It is worth mentioning the fully dense struts were produced up to the maximum energy density, 0.2 J/mm (Figure 4b), indicating that careful selection and control of energy density, via scan speed and laser power, can be used to effectively manufacture lattices with SC strategy.

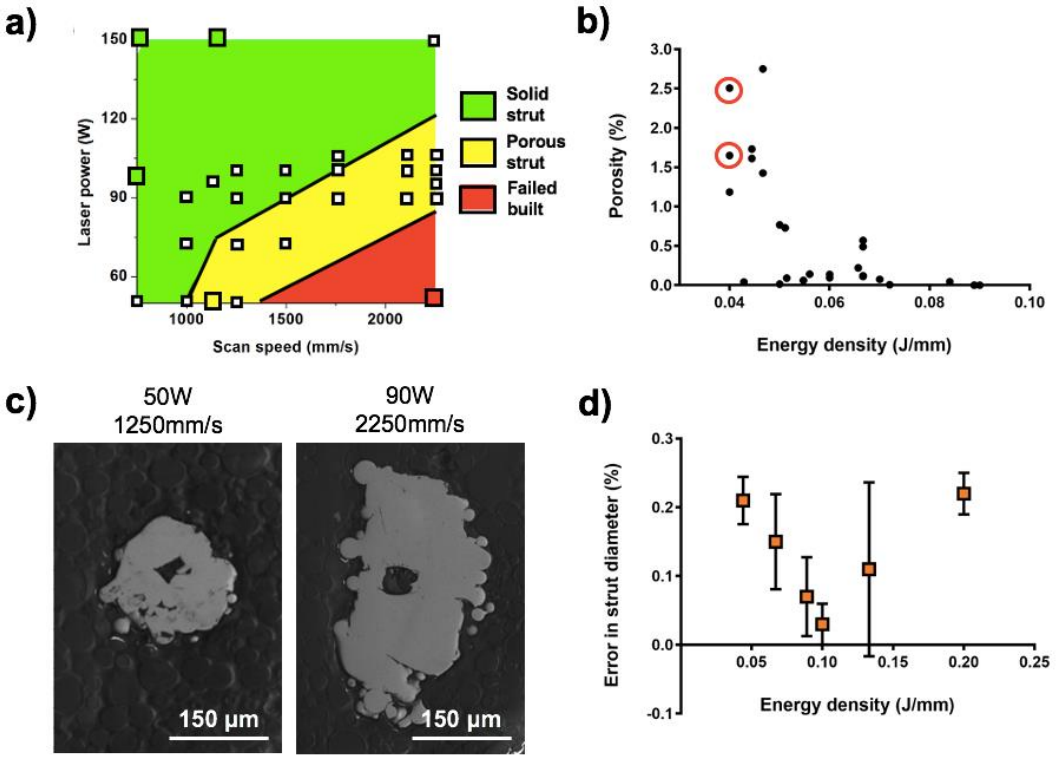

Figure 5. Images showing (a) parameters selection (white cubic dots), (b) influence of energy density on internal porosity; (c) SEM micrographs presenting the internal porosity of the two red circled parameters in (a) and (b), respectively and (d) plot demonstrating the strut size error (%) as a result of energy density variations.

Data from both studies can be combined to form a 250 µm process map of both strut diameter and porosity (Figure 6). The relationship between strut diameter and laser power (W) and scan speed (mm/s) can be fitted to a plane (Figure 6a) with a standard error of estimate, σest, of 13.8 µm (R2 = 0.77) which is reasonable given the method of measurement and irregularity of strut cross section in some cases. The plane has the equation:

$$\text{Strut Diameter } (\mu m) = 0.8423 * \text{Power (W)} - 0.0326 \text{ Speed (mm/s)} + 190.4728 \qquad \text{Equation 2}$$

Isolines derived from this planar fit are shown super-imposed over the contour plot of porosity in Figure 6b to form a process map. Fully dense (yellow) regions can easily be seen alongside the corresponding expected strut

diameter for the 250 µm design condition. Maps of this form could be produced to parametrically adjust strut geometry when using the SC strategy.

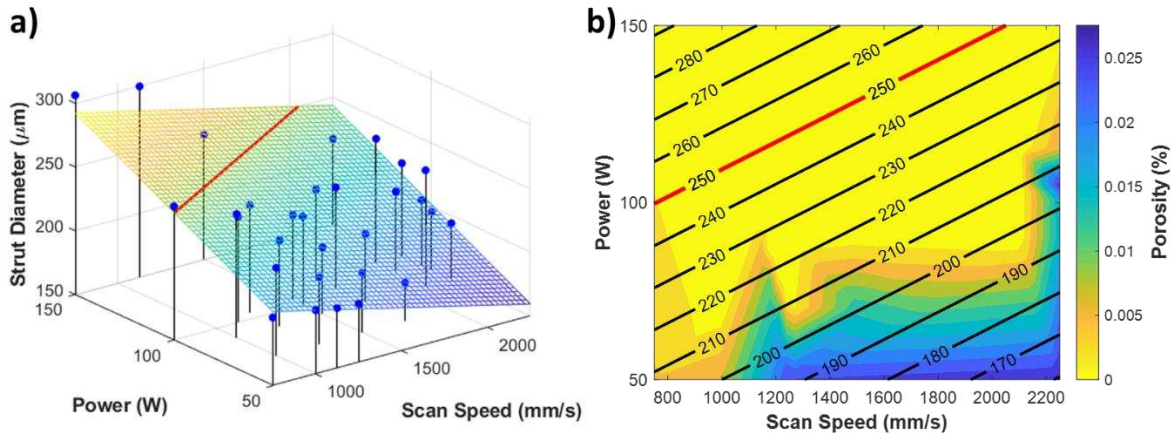

Figure 6. Process map for the combined data of both studies. (a) 3D scatter plot showing strut diameter vs laser power (W) and scan speed (mm/s) with target 250 µm condition shown by red line. (b) Process map displaying both strut diameter (labelled contour lines) and porosity (colour map) with laser power (W) and scan speed (mm/s) with target 250 µm strut diameter highlighted in red.

3.2.3.3 Wider Biomedical Implications

This study has highlighted how process parameters and laser scan strategy combine with the design to form the manufactured geometry for fine lattice structures. Understanding and control of these inputs will be critical in the translation of devices incorporating lattices from research to clinical use. Previous studies have shown how lattice density (Tobias Maconachie, 2019, Soro *et al.*, 2019) and strut diameter (Chunlei Qiu, 2015) influence mechanical properties; how pore size influences cell proliferation (Markhoff *et al.*, 2015, Li *et al.*, 2020); and how relative density can govern MRI artefacts (Luke N. Carter, 2020), or novel drug delivery (Burton *et al.*, 2019). All of these novel functionalities rely on accurate, reproducible, and robust methods of lattice manufacture to ensure the closest possible alignment of design and manufactured geometry.

By constructing process maps similar to those presented, it is possible to gain confidence that lattices will be produced 'first-time-right' when integrated in to larger implants. Likewise the SC scanning strategy aims to reduce uncontrolled variability introduced at the slicing stage. Both of these aspects will be critical, from both a patient welfare and regulatory perspective, to ensure that devices perform as intended when implanted.

3.2.4 Conclusion

In this work, the capability of SC to manufacture lattice structures with thin struts of diameter less than 350 µm has been demonstrated. Two studies have highlighted relationships between strut density and geometric accuracy showing the potential for fine control of lattice manufacture via parametric adjustment alongside the limit of such approach. Linear energy density is suggested as a practical indicator of the process, from which both the accuracy and internal morphology of lattice struts could be predicted and optimised. The process maps generated may be used in future lattice production as a practical method for structural control. It is hoped that the use of

SC processes lattice will improve geometric consistency critical for the full exploitation of AM lattices in medical devices.

References

AHMADI, S. M., CAMPOLI, G., YAVARI, S. A., SAJADIA, B., WAUTHLE, R., SCHROOTEND, J., WEINANS, H. & ZADPOOR, A. A. 2014. Mechanical behavior of regular open-cell porous biomaterials made of diamond lattice unit cells. *J. Mech. Behav. Biomed. Mater.,* 34**,** 106-115.

BURTON, H. E., EISENSTEIN, N. M., LAWLESS, B. M., JAMSHIDI, P., SEGARRA, M. A., ADDISON, O., SHEPHERD, D. E. T., ATTALLAH, M. M., GROVER, L. M. & COX, S. C. 2019. The design of additively manufactured lattices to increase the functionality of medical implants. *Mater. Sci. Eng., C,* 94**,** 901-908.

CARTER, L. N., ADDISON, O., NAJI, N., SERES, P., WILMAN, A. H., SHEPHERD, D. E. T., GROVER, L. M. & COX, S. C. 2020. Reducing MRI susceptibility artefacts in implants using additively manufactured porous Ti-6Al-4V structures. *Acta Biomater.,* 107**,** 338-348.

CHANTARAPANICH, N., PUTTAWIBUL, P., SUCHARITPWATSKUL, S., JEAMWATTHANACHAI, P., INGLAM, S. & SITTHISERIPRATIP, K. 2012. Scaffold Library for Tissue Engineering: A Geometric Evaluation. *Computational and Mathematical Methods in Medicine,* 2012**,** 407805.

CHUNLEI QIU, S. Y., NICHOLAS J.E. ADKINS, MARK WARD, HANY HASSANIN, PETER D. LEE, PHILIP J. WITHERS, MOATAZ M. ATTALLAH 2015. Influence of processing conditions on strut structure and compressive properties of cellular lattice structures fabricated by selective laser melting. *Materials Science & Engineering A,* 628**,** 188-197.

DEING, A., LUTHRINGER, B. L., LAIPPLE, D., EBEL, T. & WILLUMEIT, R. 2014. A Porous TiAl6V4 Implant Material for Medical Application. *Int. J. Biomater.,* 2014**,** 8.

DERBY, B. 2012. Printing and Prototyping of Tissues and Scaffolds. *Science,* 338**,** 921-926.

GHOUSE, S., BABU, S., VAN ARKEL, R. J., NAI, K., HOOPER, P. A. & JEFFERS, J. R. T. 2017. The influence of laser parameters and scanning strategies on the mechanical properties of a stochastic porous material. *Mater. Des.,* 131**,** 498-508.

GROßMANN, A., FELGER, J., FRÖLICH, T., GOSMANN, J. & MITTELSTEDT, C. 2019. Melt pool controlled laser powder bed fusion for customised low-density lattice structures. *Mater. Des.,* 181**,** 108054.

GU, H., GONG, H., PAL, D., RAFI, K., STARR, T. & STUCKER, B. 2013. Influences of Energy Density on Porosity and Microstructure of Selective Laser Melted 17- 4PH Stainless Steel. *Solid Freeform Fabr. Symp.,* 474**,** 474-489.

HEDAYATI, R., SADIGHI, M., MOHAMMADI-AGHDAM, M. & HOSSEINI-TOUDESHKY, H. 2018. Comparison of elastic properties of open-cell metallic biomaterials with different unit cell types. *J. Biomed. Mater. Res. B Appl. Biomater.,* 106**,** 386-398.

HEINL, P., MÜLLER, L., KÖRNER, C., SINGER, R. F. & MÜLLER, F. A. 2008. Cellular Ti–6Al–4V structures with interconnected macro porosity for bone implants fabricated by selective electron beam melting. *Acta Biomaterialia,* 4**,** 1536-1544.

HONG, M. H., MIN, B. K. & KWON, T.-Y. 2016. The Influence of Process Parameters on the Surface Roughness of a 3D-Printed Co–Cr Dental Alloy Produced via Selective Laser Melting. *Appl. Sci.,* 6**,** 401.

KHORASANIA, A., GIBSOND, I., AWANA, U. S. & GHADERI, A. 2019. The effect of SLM process parameters on density, hardness, tensile strength and surface quality of Ti-6Al-4V. *Addit. Manuf.,* 25**,** 176-186.

KOPTYUG, A., RÄNNAR, L. E., BÄCKSTRÖM, M., FAGER FRANZÉN, S. F. & DÉRAND, P. 2013. Additive Manufacturing Technology Applications Targeting Practical Surgery. *Int. J. Life Sci. Med. Res.,* 3**,** 15-24.

KUSUMA, C., AHMED, S. H., MIAN, A. & SRINIVASAN, R. 2017. Effect of Laser Power and Scan Speed on Melt Pool Characteristics of Commercially Pure Titanium (CP-Ti). *J. Mater. Eng. Perform.,* 26**,** 3560-3568.

LI, B., HESAR, B. D., ZHAO, Y. & DING, L. 2020. Design and additive manufacturing of porous titanium scaffolds for optimum cell viability in bone tissue engineering. *Proceedings of the Institution of Mechanical Engineers. Part B, Journal of engineering manufacture***,** 95440542093756.

LUKE N. CARTER, O. A., NASHWAN NAJI, PETER SERES, ALAN H. WILMAN, DUNCAN E.T. SHEPHERD, LIAM GROVER, SOPHIE COX 2020. Reducing MRI susceptibility artefacts in implants using additively manufactured porous Ti-6Al-4V structures. *Acta Biomaterialia,* 107**,** 338-348.

MAAMOUN, A. H., XUE, Y. F., ELBESTAWI, M. A. & VELDHUIS, S. C. 2018. Effect of Selective Laser Melting Process Parameters on the Quality of Al Alloy Parts: Powder Characterization, Density, Surface Roughness,and Dimensional Accuracy. *Materials,* 11**,** 2343.

MAIETTA, S., GLORIA, A., IMPROTA, G., RICHETTA, M., DE SANTIS, R. & MARTORELLI, M. 2019. A Further Analysis on Ti6Al4V Lattice Structures Manufactured by Selective Laser Melting. *J. Healthc. Eng.,* 2019**,** 9.

MARKHOFF, J., WIEDING, J., WEISSMANN, V., PASOLD, J., JONITZ-HEINCKE, A. & BADER, R. 2015. Influence of Different Three-Dimensional Open Porous Titanium Scaffold Designs on Human Osteoblasts Behavior in Static and Dynamic Cell Investigations. *Materials,* 8**,** 5490-5507.

MULLEN, L., STAMP, R. C., BROOKS, W. K., JONES, E. & SUTCLIFFE, C. J. 2009. Selective Laser Melting: A Regular Unit Cell Approach for the Manufacture of Porous, Titanium, Bone In-Growth Constructs, Suitable for Orthopedic Applications. *Wiley,* 89B**,** 325-334.

MURR, L. E. 2020. Metallurgy principles applied to powder bed fusion 3D printing/additive manufacturing of personalized and optimized metal and alloy biomedical implants: an overview. *J. Mater. Res. Technol.,* 9**,** 1087–1103.

NGUYEN, D. S., PARK, H. S. & LEE, C. M. 2020. Optimization of selective laser melting process parameters for Ti-6Al-4V alloy manufacturing using deep learning. *J. Manuf. Process,* 55**,** 230-235.

NICKELS, L. 2020. Software toolkits for architected materials, lightweighting, and more. *Met. Powder Rep.*

ONAL, E., MEDVEDEV, A. E., LEEFLANG, M. A., MOLOTNIKOV, A. & ZADPOOR, A. A. 2019. Novel microstructural features of selective laser melted lattice struts fabricated with single point exposure scanning. *Addit. Manuf.,* 29**,** 100785.

QIN, Q. & CHEN, G. X. 2013. Effects of Parameters on Surface Roughness of Metal Parts by Selective Laser Melting. *Adv. Mater. Res.,* 834**,** 872-875.

QIU, C., YUE, S., ADKINS, N. J. E., WARD, M., HASSANIN, H., LEE, P. D., WITHERS, P. J. & ATTALLAH, M. M. 2015. Influence of processing conditions on strut structure and compressive properties of cellular lattice structures fabricated by selective laser melting. *Mater. Sci. Eng., A,* 628**,** 188-197.

RASHIDA, R., MASOODA, S. H., RUANA, D., PALANISAMY, S., RASHID, R. A. R. & BRANDT, M. 2017. Effect of scan strategy on density and metallurgical properties of 17-4PH parts printed by Selective Laser Melting (SLM). *J. Mater. Process. Technol.,* 249**,** 502-511.

SALEM, H., CARTER, L. N., ATTALLAH, M. M. & SALEM, H. G. 2019. Influence of processing parameters on internal porosity and types of defects formed in Ti6Al4V lattice structure fabricated by selective laser melting. *Mater. Sci. Eng., A,* 767**,** 138387.

SCHNEIDER, C. A., RASBAND, W. S. & ELICEIRI, K. W. 2012. NIH Image to ImageJ: 25 years of image analysis. *Nat. Methods,* 9**,** 671-675.

SHIPLEY, H., MCDONNELL, D., CULLETON, M., COULL, R., LUPOI, R., O'DONNELL, G. & TRIMBLE, D. 2018. Optimisation of process parameters to address fundamental challenges during selective laser melting of Ti-6Al-4V: A review. *Int. J. Mach. Tools Manuf.,* 128**,** 1-20.

SONG, B., DONG, S., ZHANG, B., LIAO, H. & CODDET, C. 2012. Effects of processing parameters on microstructure and mechanical property of selective laser melted Ti6Al4V. *Mater. Des.,* 35**,** 120-125.

SORO, N., ATTAR, H., WU, X. & DARGUSCH, M. S. 2019. Investigation of the structure and mechanical properties of additively manufactured Ti-6Al-4V biomedical scaffolds designed with a Schwartz primitive unit-cell. *Materials Science and Engineering: A,* 745**,** 195-202.

TOBIAS MACONACHIE, M. L., BILL LOZANOVSKI, XUEZHE ZHANG, MA QIAN, OMAR FARUQUE, MILAN BRANDT 2019. SLM lattice structures: Properties, performance, applications and challenges. *Materials and Design,* 183.

TREVISAN, F., CALIGNANO, F., LORUSSO, M., PAKKANEN, J., AVERSA, A., AMBROSIO, E. P., LOMBARDI, M., FINO, P. & MANFREDI, D. 2017. On the Selective Laser Melting (SLM) of the AlSi10Mg Alloy: Process, Microstructure, and Mechanical Properties. *Materials,* 10**,** 76.

VAN BAEL, S., CHAI, Y. C., TRUSCELLO, S., MOESEN, M., KERCKHOFS, G., VAN OOSTERWYCK, H., KRUTH, J. P. & SCHROOTEN, J. 2012. The effect of pore geometry on the in vitro biological behavior of human periosteum-derived cells seeded on selective laser-melted Ti6Al4V bone scaffolds. *Acta Biomaterialia,* 8**,** 2824-2834.

VILLAPÚN, V. M., CARTER, L. N., GAO, N., ADDISON, O., WEBBER, M. A., SHEPHERD, D. E. T., ANDREWS, J. W., LOWTHER, M., AVERY, S., GLANVILL, S. J., GROVER, L. M. & COX, S. C. 2020. A design approach to facilitate selective attachment of bacteria and T mammalian cells to additively manufactured implants. *Addit. Manuf.,* 36**,** 101528.

WANG, L. Z., WANG, S. & WU, J.-J. 2017a. Experimental investigation on densification behavior and surface roughness of AlSi10Mg powders produced by selective laser melting. *Opt. Laser Technol.,* 96**,** 88-96.

WANG, X., XU, S., ZHOU, S., XU, W., LEARY, M., CHOONG, P., QIAN, M., BRANDT, M. & XIE, Y. M. 2016. Topological design and additive manufacturing of porous metals for bone scaffolds and orthopaedic implants: A review. *Biomaterials,* 83**,** 127-141.

WANG, Z., WANG, C., LI, C., QIN, Y., ZHONG, L., CHEN, B., LI, Z., LIU, H., CHANG, F. & WANG, J. 2017b. Analysis of factors influencing bone ingrowth into three-dimensional printed porous metal scaffolds: A review. *Journal of Alloys and Compounds,* 717**,** 271-285.

YAN, C., HAO, L., HUSSEIN, A. & RAYMONT, D. 2012. Evaluations of cellular lattice structures manufactured using selective laser melting. *Int. J. Mach. Tools Manuf.,* 62**,** 32-38.

YAN, C., HAO, L., HUSSEIN, A., YOUNG, P. & RAYMONT, D. 2014. Advanced lightweight 316L stainless steel cellular lattice structures fabricated via selective laser melting. *Mater. Des.,* 55**,** 533-541.

YUSUF, S. M. & GAO, N. 2017. Influence of energy density on metallurgy and properties in metal additive manufacturing. *Mater. Sci. Technol.,* 33**,** 1269-1289.

3.3 Selective laser melting of Ti-6Al-4V lattices: case study on a spinal cage prosthesis

3.3.1 Introduction

Research on orthopedic implants is in constant growth since the increase in average life spanned globally. In particular, an increasing sport life style of older people required a solution to maintain an optimal mechanical function of the human body at an advanced age [1,2]. 3D printing is a perfect technology to produce customized devices due to its flexibility. In fact, products are built layer by layer, ensuring a high freedom of design [3]. For the metallic materials, Powder Bed Fusion (PBF) technologies can be used, classified in two sub-categories, according to the source of energy used: laser or electron beam. Both these technologies are based on the same working principle: the selective melting of a powder bed followed by a rapid solidification [4]. Various alloys can be processed using Laser Powder Bed Fusion (L-PBF), such as stainless steel, Al, Cu, Co and Ti alloy. Ti-6Al-4V alloy, which is most used for the fabrication of orthopedic prostheses, is of particular interest for its mechanical properties [5,6].

Thanks to this innovative technology, it is possible to produce components with very complex geometries and porous structures, such as lattice. These parts can be integrated with a prosthesis in such a way to promote osteointegration without the application of bone cement, needed to fix the bone to the external host [7,8].

L-PBF is controlled by several parameters, and the physical phenomena taking place are particularly complex. In addition, during the process, various defects can form in the product which directly affect the final density of the structure, such as gas porosity, lack of fusion porosities, and oxide layers. Several studies focused on the improvement of quality of AM components, and a design of experiment analysis is often needed to identify the proper printing parameters to have negligible defects [4].

Due to the possibility to build complex geometry we decided to print a customized prosthesis by L-PBF composed by a full dense part, where the load is focused, and a lattice part where the load is absent. Thanks to statistically relevant tests, it is possible to optimize the printing parameters to achieve the best results.

3.3.2 Materials and methods

3.3.2.1 Fabrication and methodology

In this work, Ti-6Al-4V powder was chosen to produce cubic lattice structures. The dimensions of the samples were 20 mm3, characterized by diamond unit cells of 1 mm3, with the strut dimension set to 250 μm, because it is a suitable diameter to have a reasonable relative density of the lattice.

The RenAM 500M (Renishaw, UK) was used to print the lattices, designed using nTopology Element (nTopology Inc., 1.25.0). The main printing parameters are laser power and scanning speed, which were varied respectively in a range of values of 50W – 150W and 750mm/s – 2250mm/s. The hatching space was set to 45 μm. Once printed, the samples were detached from the substrate using Wire EDM (electro-discharge machining, CUT 20, Switzerland) and then cold mounted in acrylic resin. Furthermore, the samples were grinded on MD-

Piano 220, with 1200 and 4000 grinding discs and subsequently polished with MD-Piano Chem on both flat sides, to obtain a mirror finish surface. The samples were observed using a scanning electron microscope (SEM, Hitachi TM3000, Japan), to acquire images of the strut sections. In principle, a preliminary study was conducted, where twenty images (Figure 9) were analyzed per sample and the size of the struts and the pores was then measured using ImageJ software. Due to the building angle, the strut cross-section appeared as an ellipse. It was assumed that the minor axis of an ellipse fitted to the area would provide the strut diameter. Thus, the "fit ellipse" function was utilized for the area quantification. This allowed to classify the struts in three categories, as shown in Figure 9. This analysis allowed to obtain the best printing parameters, which combined negligible porosity.

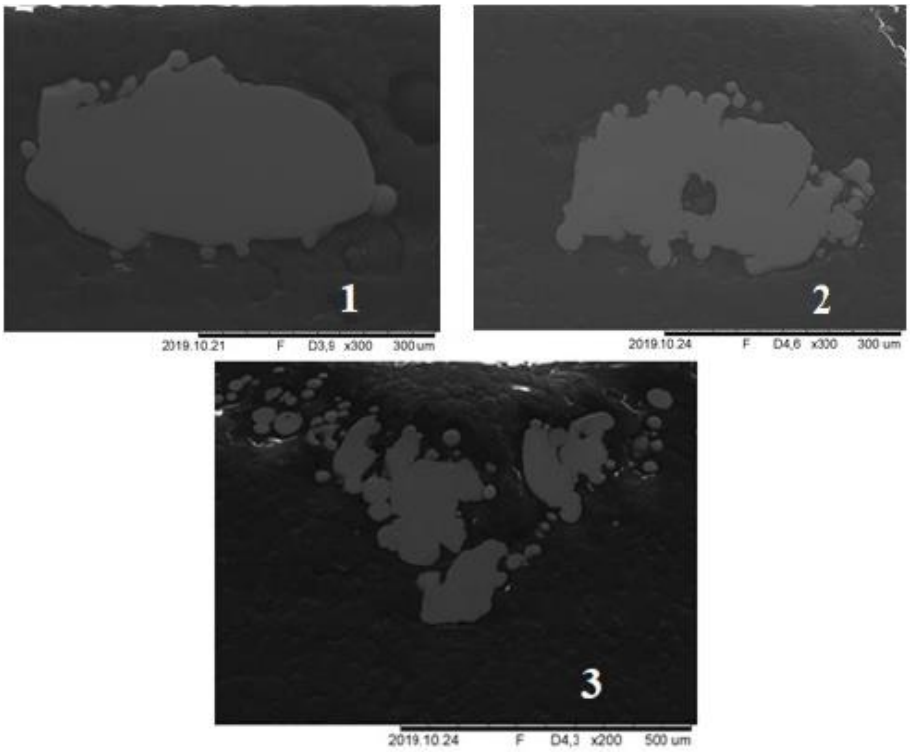

Figure 9:SEM image Strut with: 1- solid core and 2- hole in the center (porosity), 3- Damaged strut.

Furthermore, a design of experiment analysis was carried out, where the struts accuracy and the porosity level were investigated to define the best parameters to print the case study.

3.3.2.2 Preliminary study

After the analysis of the images, the porosity percentage was calculated as the ratio of the total area of the porous section and the total area of the struts present in the lattice. A porosity level of 0.25% was set as the reasonable limit for each lattice section. Thus, if the lattice section exhibited a porosity value above that limit, the sample was classified as porous. On the other hand, if the porosity value was below that limit, it was considered as non-porous. This study was carried out to validate the manufacturing process and to understand the influence of process parameters on the porosity level, with the final aim of identifying the optimal values of power and scan speed of the laser to minimize porosity.

3.3.2.3 Design of Experiment

A further study, related to the previous one, will be discussed in this section, in order to investigate the optimal parameters to print the struts with optimal size accuracy.

It was necessary to reduce the parameters studied previously to get as close as possible the value of 250 μm.

Power and scan speed were varied on three levels respectively, as represented in Table 3.

Table 3: DOE data.

Factors	Levels	Values
Power	3	50 W 100 W 150 W
Scan speed	3	750 mm/s 1125 mm/s 1500 mm/s

For each of these nine combinations, three repetitions were performed: in total, therefore, 27 specimens were printed.

3.3.3 Results

3.3.3.1 Preliminary study results

The name of the samples was defined by two numbers, where the first one was referred to the power value, while the second one corresponded to the scanning speed. The results obtained were divided in 50 W, 70 W and 90 W as shown respectively in Table 4, Table 5 and Table 6.

Table 4: Measured diameter and porosity at 50W.

Sample	Diameter [μm]	Porosity %
50-750	204±20	0,57%
50-1000	200±16	0,77%
50-1250	196±27	2,51%

Table 5: Measured diameter and porosity at 70W.

Sample	Diameter [μm]	Porosity %
70-1000	219±12	0,07%
70-1250	202±12	0,14%
70-1500	197±12	1,43%
70-1750	180±18	1,18%

Table 6: Measured diameter and porosity at 90W.

Sample	Diameter [μm]	Porosity %
90-1000	247±24	0,00%
90-1250	217±11	0,01%
90-1500	202±11	0,14%
90-1750	204±12	0,09%
90-2250	194±20	1,65%

For each considered value of laser power, different levels of scanning speed were used, to understand which was the most influencing process parameter. Firstly, a power of 50 W, was combined with three values of speed as shown in Table 4. It can be noted an increasing trend of porosity [9]. Due to these results, it was decided to do a deeper investigation with a higher value of power, but this time with higher values of velocity too, to understand what was changed in that area, as shown in Table 5. Also here, an increasing trend was identified, but which stabilized above 1500 mm/s. Therefore, it was decided to increase the power value to 90 W, and keep the four speed values used before with one more value of 2250 mm/s, to check the trend above 1500 mm/s. As shown in Table 6, the same trend as before was found, but this time with a lower value of porosity, except for 2250 mm/s, where the porosity was drastically increased for the high value of speed. Probably this speed value was too high for 90 W and it resulted in the formation of more porosities [9].

Once defined the trend with the first three values of power, other two values of power were tested, as shown in Table 7 and Table 8.

Table 7: Measured diameter and porosity at 105W.

Sample	Diameter [μm]	Porosity %
105-1250	234±13	0,05%
105-1500	217±12	0,08%
105-1750	230±24	0,09%
105-2250	201±15	2,75%

Table 8: Measured diameter and porosity at 150W.

Sample	Diameter [μm]	Porosity %
150-2250a	219±11	0,11%
150-2250b	215±9	0,12%

The lowest speed value used with 90 W was discharged because 1000 mm/s is too low for these higher power values. Also here, an increasing trend of porosity was seen, but once again, the speed of 2250 mm/s has resulted in a really high porosity.

Finally, to understand what happened with a speed of 2250 mm/s, the power value was increased to 150 W and tested only with that speed value, but this time with one repetition. As shown in Table 8, the porosity became

negligible thanks to the combination of high scan speed and a higher power value. This speed value was too high to build the samples, because it required very high value of power.

The results of the porosity percentage were reported in Figure 10 which indicates that 60% of the lattice produced for this preliminary study presented full core struts.

In particular, samples showed negligible porosity when the power value was in a range between 90 W and 105 W and the speed was between 1000 mm/s and 1750 mm/s.

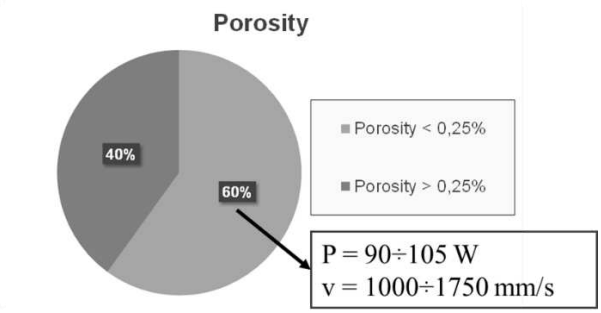

Figure 10: Porosity percentage evaluation.

For a better understanding, experimental tests were carried out to focus the study on a smaller window of parameters.

3.3.3.2 DOE results

In this second step the diameter of the struts was evaluated, because the porosity has been already investigated during the preliminary study.

27 lattices were built and analyzed under SEM, which was useful to verify the process stability to carry out the DOE study.

The poor surface finishing of products manufactured using L-PBF is a well-known limitation of this technology [9,10]. As visible in Figure 3, the surface of the struts is very irregular due to the presence of several unmelted particles, partially melted particles, or spatters. This makes difficult to properly assess the size of the struts.

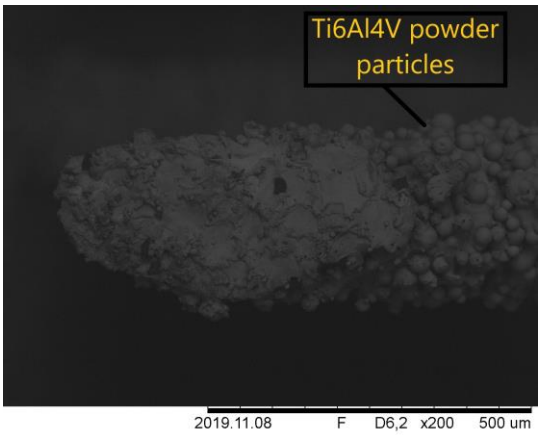

Figure 11: Image 25x magnification lattice structure with surface defects.

In the present study, it was decided to measure the struts diameter including the defects (unmelted powders, partially melted powders, spatters) eventually present, as shown in Figure 12.

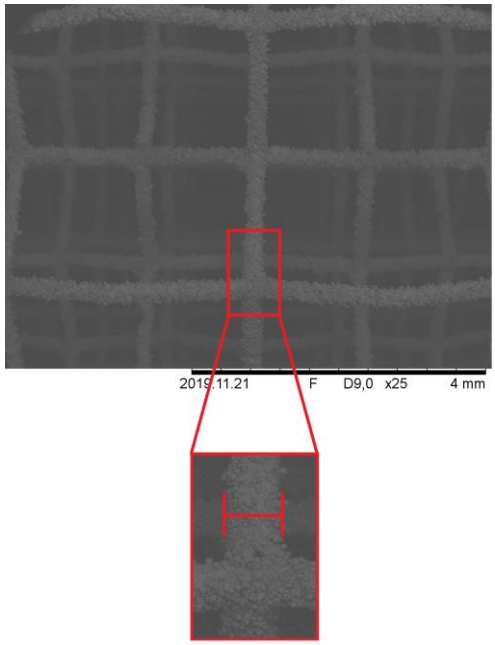

Figure 12: image 200x magnification lattice structure and strut diameter calculation.

The obtained results are reported in Table 9. The variability of the measurements is shown in Figure 13.

Table 9: Diameter size of As built samples.

Sample	Diameter [µm]
50-750	317±22
100-750	367±59
150-750	376±50
50-1125	312±23
100-1125	327±23
150-1125	381±53
50-1500	*failed*
100-1500	348±109
150-1500	336±22

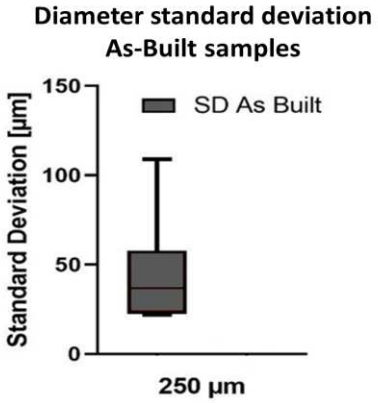

Figure 13: Diameter standard deviation of as built samples.

It can be noticed that in Table 9 the standard deviation for the sample built with 100 W and 1500 mm/s is extremely high, this could be explained by the presence of un-melted powder on the structure which can affect

the size of the strut diameter, such as for the other samples. In addition, with a scanning speed of 1500 mm/s, and a power of 50 W and 100 W, the struts are not properly built [9].

Once the values of the diameters and relative standard deviations of the as-built specimens were collected, samples were cold mounted, grinded and polished to study the cross section. The diameter of the struts was measured using the same procedure applied before.

The results are reported in Table 10. In this way between these two measurement methods the differences were marked. The standard deviation (Figure 14), as expected, is significantly lower than in the previous study. This is because the dimensional measurement of the cross section of the struts is more accurate.

The standard deviation of these latter measurements was represented graphically in Figure 14 to highlight the low variability of the output diameter. It was immediately appreciable that the standard deviation related to this kind of specimens was more uniform, and it was decided to proceed with a DOE analysis focused on them.

Table 10: Diameter size of struts section.

Sample	Diameter [μm]
50-750	205±21
100-750	254±8
150-750	307±8
50-1125	195±9
100-1125	232±14
150-1125	291±34
50-1500	*failed*
100-1500	221±14
150-1500	246±12

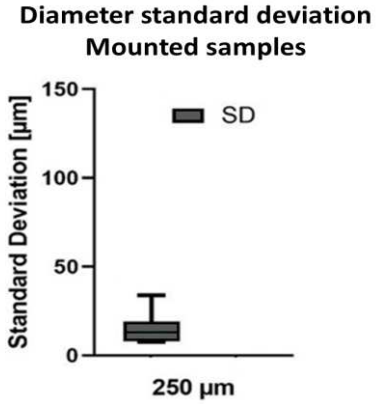

Figure 14: Diameter standard deviation of struts section.

Once the DOE study was performed, the 3D scatterplot and the contour plot respectively showed in

Figure 15 and

Figure 16, were plotted to understand the trend of the optimal parameters.

In the scatterplot there are two bands of points, considering the following main restrictions:

$$|D - D_0| > 10\mu m, Red$$
$$|D - D_0| < 10\mu m, Green$$

where D represents the average diameter calculated in DOE analysis, while D0 represents the nominal value of 250 µm that is aimed to be obtained. This distribution showed two couples of points in the optimum range at the ends of the graph with power respectively of 100 W and 150 W and speed of 750 mm/s and 1500 mm/s. In addition, in the center of the scatterplot a single optimum point appears, with a power of 100 W and scan speed of 1150 mm/s, and in one of the ends of the graph another single point in the optimum range is identified, with process parameters of 150 W and 1150 mm/s, but these two values were in the limit of range, because the difference between D and D0 was really close to 10 µm.

In

Figure 16, it was plotted the accuracy by calculating a maximum deviation of 10 µm given by D-D0 in order to highlight the different areas of struts size.

From the graph shown in

Figure 16 an optimal central band can be noticed: in particular, at the ends of it, there was a greater precision because the distribution of the optimum points had a greater concentration. It was important to underline that the general optimum trend follows an increasing behavior. In fact, the highest precision has been achieved when power and scan speed increase proportionally. Moreover, it was possible to work according to the limits of the printer (under 2000 mm/s of scan speed) varying the scan speed between 750 mm/s and 1500 mm/s, while it was always possible to get the optimal strut diameter just varying the power value between 75 W and 150 W. This was a confirmation of the greater influence of power on the results in relation to the scan speed.

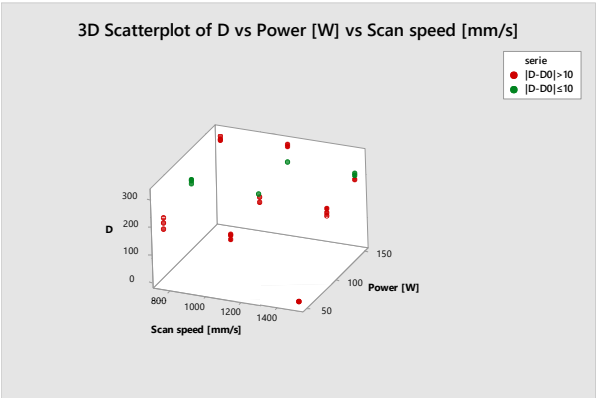

Figure 15: 3D Scatterplot of D vs Power vs Scan speed.

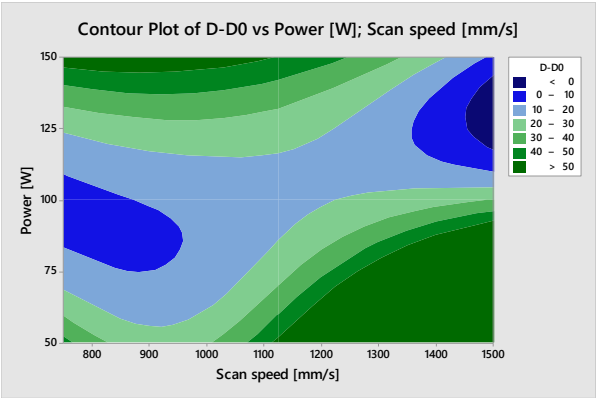

Figure 16: Contour plot of D-D0 vs Power vs Scan speed.

Moreover, the porosity and the accuracy were put in comparison by plotting them into two different graphs, as shown in Figure 17a-b.

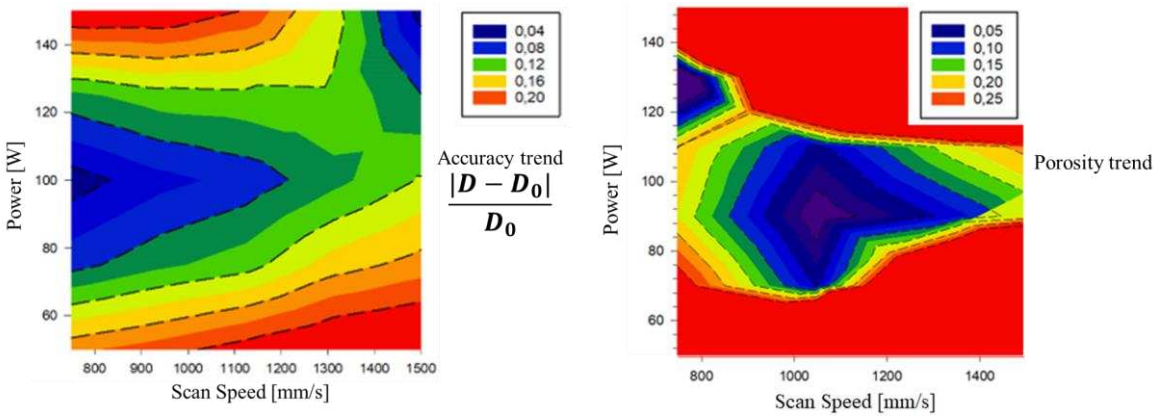

Figure 17: Contour plot of (a) accuracy and (b) porosity.

The limit for the accuracy was set at 0,04 as a reference since it is the ratio between 10 µm and 250 µm and thus it represented the minimum acceptable deviation from the aimed diameter result.

From the two graphs, it can be noticed that, although two areas of optimum have been obtained, only one of these has a porosity lower than 0,25% (as discussed in the previous chapter). The power value of 100 W was identified as optimal for its good combination of low porosity and good accuracy, which is possible to see in Figure 17 and **Errore. L'origine riferimento non è stata trovata.**. The scan speed value of 750 mm/s was identified as most adequate for the same reasons, and also because with a lower speed level it is easier to control the printing process.

3.3.4 Case study – Spinal cage

3.3.4.1 Design, accuracy, and porosity analysis

An application case of spinal implants, which are a clear example of implant where a lattice structure may be applied, was studied. The cage CAD file was designed as shown in Figure 18.

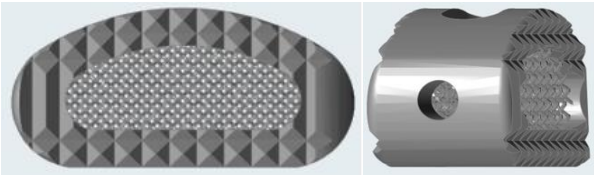

Figure 18: Designed 3D spinal cage.

The considerable advantage of using a lattice is that implants with microrough surface topographies and porosity have been shown to promote direct bone on growth, in growth and vascularization [1].

The aim was to extend the study of a lattice structure to a case of actual application where it can be integrated, evaluating the feasibility of the study from a practical and concrete point of view.

The purpose was to focus on the analysis of the porosity and the precision of the printed strut diameter. However, the case study was focused on obtaining further confirmation of the results obtained previously and it was assessed how much effectively a change in the three-dimensional shape affected the previous conclusions. The full part was printed using power of 200 W and a scan speed of 1500 mm/s to have a solid structure, while the reticulated part had as input the pair of optimal parameters previously detected, i.e. power of 100 W and scan speed of 750 mm/s. The size of the unit cell was changed to verify if the optimal parameters were still valid modifying the degree of structural porosity of the lattice.

The print was started forcing the process limits of the machine in morphological terms, since the strut and the cell were dimensionally comparable. In this case, in the preliminary phase a deviation from the optimal diameter of 10 μm was set.

An average diameter of the struts of 224±15 μm with a porosity lower than 0.25%, was recorded. Considering the very small cell dimensions (2x2x2 mm3), the results achieved could be considered optimal. In fact, the strut did not have the opportunity to expand as much as before due to the geometric constraints.

Regarding the evaluation of porosity, some demonstrative images are shown in Figure 19.

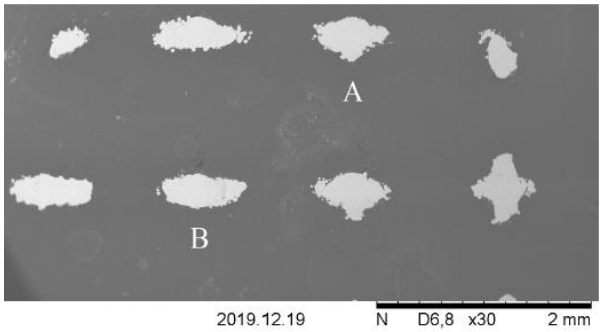

Figure 19: SEM demonstrative image of the struts.

Thanks to the set process parameters, a porosity of almost zero was recorded, as can be seen from Figure 20.

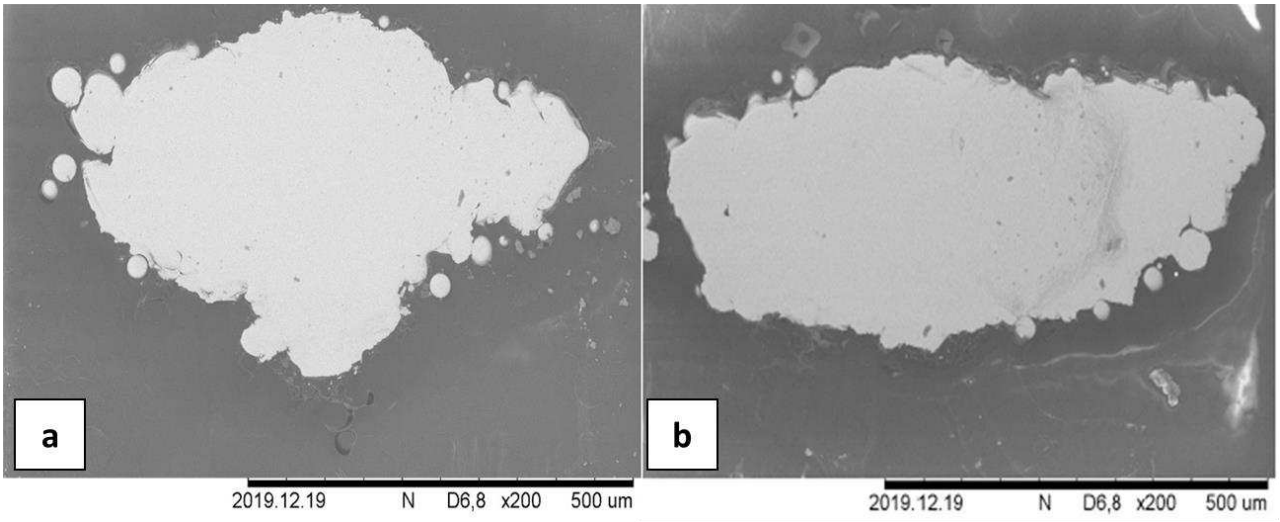

Figure 20: Struts detail A and B of Figure 19.

3.3.4.2 Microstructural characterization

To have a better evaluation of reliability and efficiency of the process, the microstructure of the product was also analyzed, which is strongly influenced by the process parameters used. In fact, the typical high cooling rates of the process influence the phase transformations during the solidification by determining specific microstructural features.

A cross section of the produced spinal cage was observed after polishing to mirror finishing and etching with Kroll's reagent to identify the main microstructural features.

Figure 21 shows the alloy microstructure. It is composed by a fine lamellar (Widmänstatten) α+β microstructure. This microstructure is consistent with the combination of high scanning speed and high thermal gradient with fast cooling rate typical of the process and it is widely reported in the literature for the same alloys processed with similar parameters [1], indicating the stability of the process, not only in terms of porosity level and geometrical accuracy.

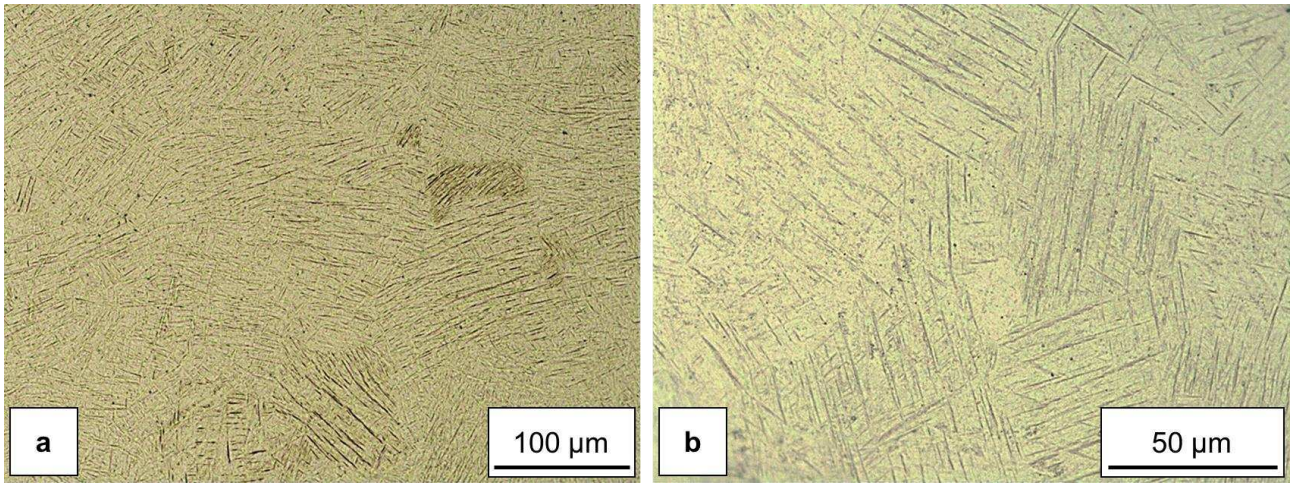

Figure 21: a) Ti-6Al-4V alloy microstructure and b) microstructure at higher magnification.

3.3.4 Conclusions

The main aim of this work was to analyze the porosity and the reliability of the results achieved of lattice structure of Ti-6V-4Al alloy manufactured by L-PBF. The process parameters were varied to reach negligible porosity and designed diameter of the struts, finally used to produce a spinal cage case study.

The first analyses were focused on narrowing the window of parameters, in order to be able to estimate in a fast way the optimal parameters necessary to achieve the diameter corresponding to 250 μm. It was necessary to change the scan speed and the power of laser to understand which one of them was more influent to reach the stability of the process. In particular, the preliminary study was carried out to the evolution of porosity varying these two parameters. Moreover, due to the DOE analysis, the highest precision has been achieved. Laser scan speed of 750 mm/s and laser power of 100W allowed to achieve a good combination

n of low porosity and good accuracy. In fact, the designed strut diameter, needed to produce the case study, was manufactured.

Finally, the porosity and the struts diameter of the spinal cage were measured and the Ti-6V-4Al microstructure was investigated. It was found the designed diameter size with negligible porosity and the typical microstructure, indicating the stability of the process.

References

[1] T. Majumdar, N. Eisenstein, J. E. Frith, S. C. Cox, and N. Birbilis, "Additive Manufacturing of Titanium Alloys for Orthopedic Applications: A Materials Science Viewpoint," Adv. Eng. Mater., vol. 20, no. 9, 2018, doi: 10.1002/adem.201800172.

[2] G. Allegri, A. Colpani, P. S. Ginestra, and A. Attanasio, "An experimental study on micro-milling of a medical grade Co-Cr-Mo alloy produced by selective laser melting," Materials (Basel)., vol. 12, no. 13, 2019, doi: 10.3390/ma12132208.

[3] M. Vignesh et al., "Development of Biomedical Implants through Additive Manufacturing: A Review," J. Mater. Eng. Perform., vol. 30, no. 7, pp. 4735–4744, 2021, doi: 10.1007/s11665-021-05578-7.

[4] H. Salem, L. N. Carter, M. M. Attallah, and H. G. Salem, "Influence of processing parameters on internal porosity and types of defects formed in Ti6Al4V lattice structure fabricated by selective laser melting," Mater. Sci. Eng. A, vol. 767, no. May, p. 138387, 2019, doi: 10.1016/j.msea.2019.138387.

[5] S. K. Gupta et al., "Enhanced biomechanical performance of additively manufactured Ti-6Al-4V bone plates," J. Mech. Behav. Biomed. Mater., vol. 119, no. March, p. 104552, 2021, doi: 10.1016/j.jmbbm.2021.104552.

[6] P. Ginestra et al., "Post processing of 3D printed metal scaffolds: A preliminary study of antimicrobial efficiency," Procedia Manuf., vol. 47, no. 2019, pp. 1106–1112, 2020, doi: 10.1016/j.promfg.2020.04.126.

[7] L. Riva, P. S. Ginestra, and E. Ceretti, “Mechanical characterization and properties of laser-based powder bed–fused lattice structures: a review,” Int. J. Adv. Manuf. Technol., vol. 113, no. 3–4, pp. 649–671, 2021, doi: 10.1007/s00170-021-06631-4.

[8] P. Ginestra et al., “Surface ace finish of A Additi dditiv vel ely y Manuf Manufactur actured ed Metals : biofilm f formation ormation and cellular attachment 1 Intr Introduction oduction 2 Manuf Manufacturing acturing and post pr processing ocessing treatment,” vol. 13, pp. 1–12, 2021.

[9] T. Majumdar, T. Bazin, E. M. C. Ribeiro, J. E. Frith, and N. Birbilis, “Understanding the effects of PBF process parameter interplay on Ti-6Al-4V surface properties,” PLoS One, vol. 14, no. 8, pp. 1–24, 2019, doi: 10.1371/journal.pone.0221198.

[10] M. Nakatani, H. Masuo, Y. Tanaka, and Y. Murakami, “Effect of Surface Roughness on Fatigue Strength of Ti-6Al-4V Alloy Manufactured by Additive Manufacturing,” Procedia Struct. Integr., vol. 19, pp. 294–301, 2019, doi: 10.1016/j.prostr.2019.12.032.

Chapter 4
17-4 PH SS

In this work, 17-4 PH stainless steel square-based lattice structures with solid shell were manufactured by Laser Powder Bed Fusion. Face Centered Cubic unit cell was chosen as lattice cell geometry. The main aim of this work was to study the role of the shell in the mechanical behavior under compression load and to identify eventual critical issues due to the connection of the shell with lattice part. This is a relevant topic since often lattice structure are integrated with solid walls and the study of the relative behavior can support the understating of the performance of complex components. The manufactured samples were tested in as-built and heat-treated condition.

The published paper and industrial project related to the 17-4 PH SS are listed below:

- Cantaboni F, Tocci M, Ginestra PS, Pola A, Ceretti E. Production and characterization of lattice samples with solid shell in 17-4 PH stainless steel by Laser Powder Bed Fusion technology. Procedia Structural Integrity 2024;53:65–73. https://doi.org/10.1016/j.prostr.2024.01.009.
- Cantaboni, F., Viscardi C., Ginestra, P., Tocci, M., Pola, A., & Ceretti, E. (2024). Laser Powder Bed Fusion process simulation and Residual stresses analysis with Deform 3D. In collaboration with “ECOTRE VALENTE” and “DUEFFE ENGINEERING” Companies, report on case study.

4.1 Production and characterization of lattice samples with solid shell in 17-4 PH stainless steel by Laser Powder Bed Fusion technology

4.1.1 Introduction

Laser powder bed fusion (L-PBF) is the most common Additive Manufacturing (AM) process for the production of metallic components. Various alloys can be used, such as stainless steel, titanium, copper, aluminum, and cobalt alloys Bayat et al. (2019); Ginestra et al. (2020); Razavi et al. (2021). In particular 17-4 PH is usually used for the fabrication of stainless-steel parts due to its excellent weldability, corrosion resistance, high strength and hardness Cantaboni et al. (2022); Kareem et al. (2023); Leo et al. (2021). AM is used for the production of components with complex geometry with desirable mechanical properties, such as stochastic foams and lattice structures Bai et al. (2021); Bertocco et al. (2022). In particular, the lattice structures are widely used in aerospace, automotive and medical industry due to their excellent properties including lightweight, high strength and stiffness, heat dissipation and shock absorption Xiao et al. (2018).

The lattice structures are commonly used combined with fully dense structures and supports, as shown in the literature. For instance, the solid-lattice hybrid structures composed by solid and lattice part were already studied Dong et al. (2020a). In this work, a designed model of solid hybrid lattice structure, with optimized strut thickness connected to the solid part with Boolean operation, was proposed and compared with pure solid structure and a pure lattice structure. The authors demonstrated that the solid lattice hybrid structure shows the best mechanical performance. Moreover, the lattice structures are integrated in already existing components for weight reduction maintaining equivalent mechanical properties Bertol et al. (2010).

There are some studies where solid-lattice structures are tested to investigate the behavior between solid and lattice part. Jin F. et al. Fu et al. (2022) produced stainless steel 316L Triply periodic minimal surfaces (TPMS) shell lattices with different shell thicknesses. They proved that with increasing relative density, the deformation mechanism transforms from localized collapse to homogeneous bulk deformation showing the highest potential for lightweight designs. Moreover, G. Dong et al. Dong et al. (2020b) manufactured a hybrid element model defined by solid-lattice interface used to simulate the mechanical performance and optimize the material distribution of the lattice structure. The stiffness and the ultimate strength of the hybrid structure were higher than the solid and lattice structure separately.

In this work, square-based 17-4 PH samples with solid shell were produced by L-PBF technology, half of which were heat treated. The main aim of this work was to study the role of the shell in the mechanical behavior of complex structures under compression load and to identify eventual critical issues due to the connection of the shell with the lattice part.

4.1.2 Materials and methods

4.1.2.1 Samples productions and heat treatment

Six square-based lattice samples with solid shell (as shown in Figure 1a) were designed and produced. The dimension of the samples is 22 (L) x 22 (L) x 20 (H) mm, where L and H are the length and the heigh of the structure, respectively. The thickness of the shell is 1 mm. The samples are characterized by a Face Centered Cubic (FCC) unit cell reported in Fig.1b with a length of 5 mm. The cylindrical struts with diameter (Dc) of 500 μm are connected to a spherical node with a diameter (Dn) of 1.0 mm. Moreover, four bulk cubic samples with a length of 10 mm were produced for microstructural characterization and hardness measurements.

Fig. 1. (a) square-based lattice sample with solid shell; (b) design of Face Centered Cubic (FCC) unit cell.

ProX® DMP 100 printer (3D system®, Wilsonville, Oregon, USA) was used to produce the samples in a controlled nitrogen inert gas atmosphere (O_2 < 0.01 %) with the process parameters reported in Table 1. Samples were designed using 3D XPert software, (ProX® DMP 100, 3D system, Rock Hill, South Carolina, USA).

Table 1. Process parameters used to produce the investigated samples.

Process Parameters	Value
Power [W]	100
Scanning speed [mm/s]	300
Hatch spacing [μm]	50
Layer thickness [μm]	30
Spot diameter [μm]	80

The samples were manufactured using 17-4 PH powder produced by LaserForm®, whose nominal chemical composition is reported in Table 2.

Table 2. Nominal chemical composition (wt%) of 17-4 PH powders used for the production of samples.

ELEMENT	Cr	Ni	Cu	Nb+Ta	C	Mn	P	S	Si	Fe
Wt. %	15.00 – 17.50	3.00 – 5.00	3.00 – 5.00	0.15 – 0.45	<0.07	<1.00	<0.04	<0.03	<0.01	Bal.

To enhance the mechanical properties of L-PBF 17-4 PH, half of the samples and two cubes were heat treated. The solution and aging treatments were performed on three samples using a furnace for vacuum heat treatment in order to achieve homogenization and effective precipitation-hardening An et al. (2023); Mahmoudi et al. (2017).

During vacuum treatment a partial pressure of inert gas (Argon) was introduced in the furnace chamber. The samples were solution-treated at 1040 °C (T_1) for 1 h followed by cooling in argon flow with a pressure of 5 bar. The cooling rate was 80 °C/min. After solution treatment the samples were aged at 480 °C (T_2) for 4 h and cooled in air. The samples after heat treatment are named Heat Treated (HT) samples, while samples tested in as-built condition are indicated as AB.

4.1.2.2 Metallurgical, technological, and mechanical characterizations

Once manufactured, the height and length of the samples were measured with Vernier caliper and compared with the designed one. One AB sample was cut with a metallographic saw in order to observe a vertical and horizontal cross section and identify defects at the interface between lattice and shell and to perform a dimensional analysis of the structure. AB and HT (bulk) cubic samples were then mounted in acrylic resin, polished up to mirror finishing, and etched for 30 seconds with Fry's reagent to identify the main microstructural features.

The optical microscope (LEICA DMI 5000 M, Wetzlar, Germany) was used to measure strut diameter, shell thickness, porosity, and eventual defects at the connection between the lattice and solid shell. Furthermore, a deep analysis of the microstructure of samples were carried out under scanning electron microscope (SEM), LEO EVO® 40 (Carl Zeiss AG, Italy) equipped with Energy-Dispersive X-ray Spectroscopy (EDS) detector.

Moreover, Vickers microhardness measurements were performed with Mitutoyo HM-200 (Mitutoyo Corporation, Kawasaki (Kanagawa, Japan) hardness testing machine on four cubic samples (two of which treated) to evaluate the effectiveness of the heat treatment. A load of 0.5 kg was applied for 15 s. Ten repetitions for each condition were performed along the cross section.

Compressions tests were carried out with a servo-hydraulic testing machine Galdabini QUASAR 250 (Galdabini (S.P.A.), Cardano Al Campo VA, Italy) equipped with a 250 kN load cell. The tests were conducted in displacement control at a constant crosshead velocity of 2 mm/min and the displacement was measured using the crosshead movement. The stress-strain curves were obtained, and the mechanical features were calculated, such as Young's modulus, yield stress (as compressive offset stress at the plastic compressive strain of 0.2 %) and ultimate strength (as the peak of stress detected). The failure of the samples was analyzed.

4.1.3 Results and discussion

4.1.3.1 Samples characterizations

The samples length and height, the thickness (tk) of the solid shell and the diameter (Dc) of the struts were measured on the cross section of the lattice specimens and the results are reported in Table 3. It has to be mentioned that the height of samples was slightly influenced by the support removal.

The diameter of the struts resulted close to the designed one (0.5 mm), while the thickness of the shell was below the design value (1.0 mm). The calculated standard deviation is reasonable, meaning a regular geometric size. The thickness of the shell resulted slightly lower than the design and this was probably due to the instability of

the process and thermal distortion in consequence of the laser scan strategy and the use of low-energy settings Wu, Narra, and Rollett (n.d.).

Table 3. Measured dimensions of As-Built samples.

H [mm]	L [mm]	Dc [µm]	tk [µm]
19.1 ± 0.16	21.98 ± 0.05	508.1 ± 34.1	930.4 ± 18.4

The interface between lattice and solid part is known to represent a critical feature and was therefore analyzed. In Figure 2, two micrographs of the connection between lattice and shell were reported as representative examples. In particular, in Fig. 2a a critical connection is shown. In this case, lack-of-fusion porosities were detected on the connection between strut and node, sensibly reducing the load bearing area. On the other hand, as shown in Fig. 2b, often the connections were denser, with smaller porosities. In both cases the junction between node and shell was denser than the strut-node connections. The critical features were probably due to the local lack of melting and the abrupt change of geometry from thin struts to a bulk structure.

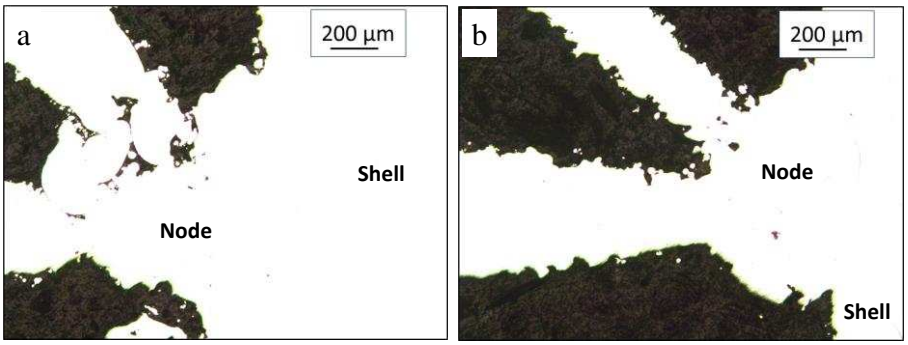

Fig. 2. Two examples of connection between lattice and shell. (a) lack-of-fusion porosities and (b) denser connection with small porosities.

4.1.3.2 Microstructure

The micrographs of the longitudinal (L) and transverse (T) cross-section of as-built 17-4 PH samples were reported in Fig. 3a and 3b, respectively.

The typical microstructure of 17-4 PH alloy produced by L-PBF is clearly visible. The presence of partially overlapped melt pools, formed due to the melting of metal powders under the laser action, is highlighted by the white arrows on the L cross section in Figure 3a. The scan tracks identifying the path of the laser during the manufacturing process are highlighted by yellow arrows on the T cross section in Fig. 3b, as in accordance with C. Garcia-Cabezon et al. (2022). Moreover, the typical sections of the columnar grains are visible in Fig. 3b.

The HT samples show a completely different microstructure, as reported in Fig. 3c and 3d. The melt pools and scan tracks disappeared due to the solution treatment An et al. (2023b). Black dots are also visible on both cross sections after heat treatment. These are likely precipitates formed during aging treatment. These appears to be present along the grain boundaries but also dispersed in the matrix.

Moreover, during the manufacturing process the presence of nitrogen as an austenite-stabilizing element likely allowed the formation of austenite which is only partially transformed into martensite during rapid solidification cooling Leo et al. (2021).

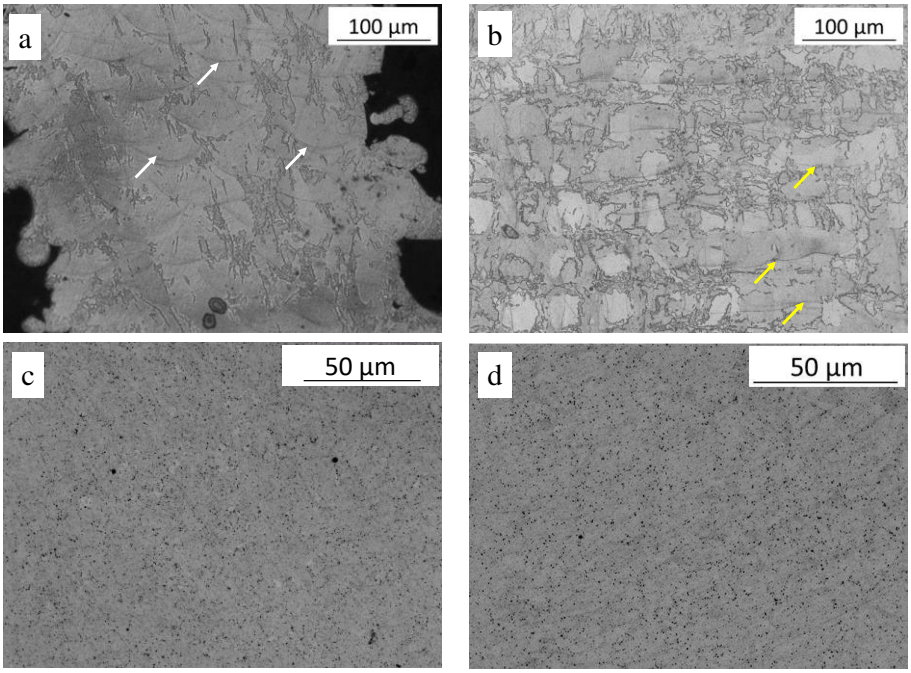

Fig. 3. Optical micrographs of longitudinal (a) and transverse (b) cross-sections of AB samples. Melt pools, scan tracks and columnar grain sections were highlighted by white, yellow, and red arrows, respectively. Optical micrographs of longitudinal (c) and transverse (d) cross-sections of HT samples.

The microstructure of AB and HT samples was further investigated under SEM. The micrographs at higher magnification of AB and HT samples were reported in Fig. 4a and 4b, respectively. In Fig. 4a, areas of different color highlight the presence of elongated grains. EDS analyses (spectrum AB1 and AB3 in Table 4) reveal a chemical composition close to the nominal composition of the alloy. Lighter particles are also visible, which resulted to be particularly rich in Cu (spectrum AB2 in Table 4). These are likely segregations rich in Cu formed during the rapid solidification as also reported in An et al. (2023a).

During the heat treatment these segregations are dissolved, and this promotes the formation of Cu-rich precipitates along the grain boundaries and within the matrix, clearly visible in Fig. 4b. The presence of Cu was demonstrated by EDS results for HT1 spectrum in Fig. 4b and Table 4.

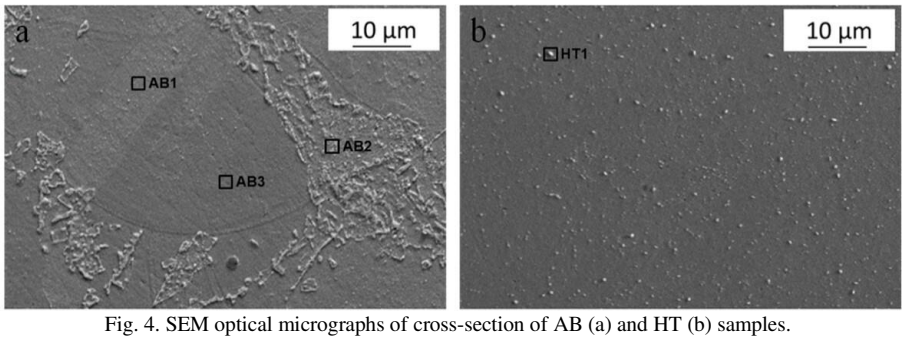

Fig. 4. SEM optical micrographs of cross-section of AB (a) and HT (b) samples.

Table 4. Chemical elements measured by EDS (all results in weight%).

Spectrum	Si	Mn	Cr	Fe	Ni	Cu
AB1	0.95	-	17.61	71.39	5.21	4.84
AB2	-	-	13.62	57.99	3.96	**24.42**
AB3	0.99	1.01	17.26	72.26	4.69	3.79
HT1	-	-	11.96	48.19	3.44	**36.41**

4.1.3.3 Micro hardness

The hardness of AB samples was 345 ± 10 HV, while for HT samples a hardness of 495 ± 11 HV was measured. The HT samples shown an increase of 45% of hardness compared to the AB samples. In accordance with Garcia-Cabezon et al. (2022) the recrystallization of the structure and the Cu-rich precipitates formed during aging treatment were responsible for the increase in hardness.

4.1.3.4 Mechanical characterizations

Compression tests were performed on the AB and HT samples. The stress-strain curves calculated from the compression test are shown in Fig. 5a.

A different behavior for the AB and HT samples was detected. In particular, the HT samples exhibited higher strength compared to the AB samples, reaching higher ultimate strength (σM). The σM of AB samples was 174.1 ± 0.4 MPa, while for the HT samples this value increased of 42% reaching 247.9 ± 3.0 MPa. Moreover, AB samples showed a plateau (typical of bending-dominated behavior, which exhibited good absorption properties, ideal for shock absorption applications Jin et al. (2021); Kotzem et al. (2023)) after reaching the maximum stress and they did not present a collapse point. The stress measured during compression tests of HT samples grew up to the ultimate strength (σM) and decreased immediately after. The higher stress corresponds to the buckling of the central "floor" of the structure as shown in Fig. 5b. After buckling phenomena, the deformation of the struts continued. The load decreased because some of the struts were deformed and broken, and the deformation of the entire structure was easier.

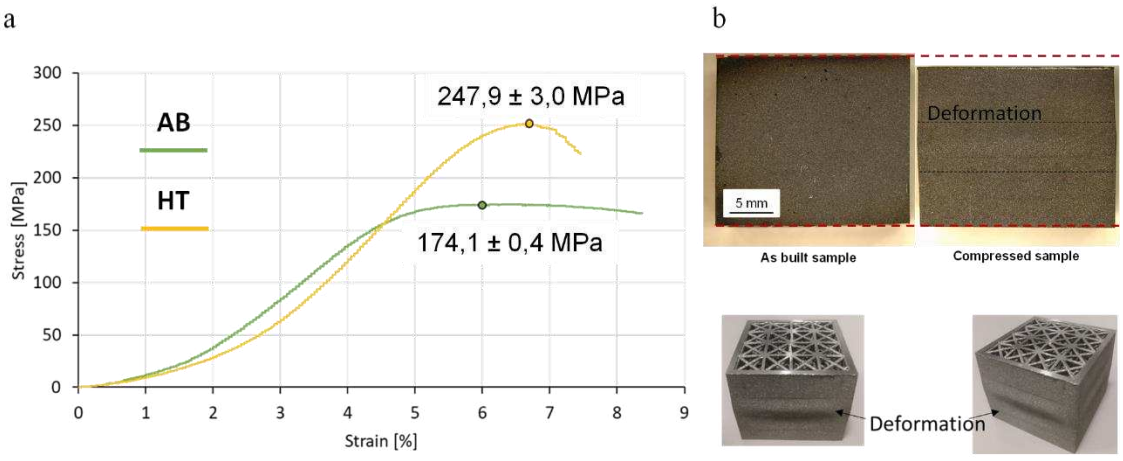

Fig. 5. (a) Stress-strain curves of AB and HT samples. (b) samples before and after compression test.

A complete overview of mechanical characteristics is reported in Table 5. The Young's modulus of HT was 64.2 ± 1.9 GPa, 30% higher than the AB samples which was 49.5 ± 0.0 GPa. The yield stress of HT was 237.7

± 6.8 MPa, 44% higher than the AB samples which was 165.3 ± 4.0 MPa. After the tests, the deformation of AB and HT samples were 0.84 mm and 0.33 mm, respectively. The stiffness, yield stress and ultimate strength increased after the heat treatment, as already discussed by Y. Si Mo et al. Yeon et al. (2022).

The HT samples exhibited higher stiffness, hardness and strength probably due to the homogenization and recrystallization of the microstructure. In particular, the formation of Cu-rich precipitates (Fig. 3c-d) gives higher isotropy and ductility Lashgari et al. (2020).

Table 5: Results of the compression tests of AB and HT samples.

	AB	**HT**
E [GPa]	49.5 ± 0.0	64.2 ± 1.9
σ_y [MPa]	165.3 ± 4.0	237.7 ± 6.8
ε_y [%]	4.9 ± 0.1	6.2 ± 0.4
σ_M [MPa]	174.1 ± 0.4	247.9 ± 3.0
ε_M [%]	6.1 ± 0.6	6.9 ± 0.4

An interesting finding of this work was the behavior of the shell. In fact, the solid part followed the deformation of the structure, as shown in Fig. 5b, and no detachment of the shell from the lattice occur under compression. This is interesting since a detachment of the shell during the compression test can be expected due to the expansion of the structure in the lateral direction. This can be encouraged by the presence of defect at the shell/lattice interface. Instead, the interface connection of 17-4PH structures was stronger and the detachment of the shell did not occur.

The struts after compression test are reported in Fig. 6. It can be noticed that the broken struts highlighted with the white arrows are in the center part of lattice, while the struts connected to the shell were not compromised. To better understand the behavior of the struts within the structure a deeper analysis is required. Based on the observed mechanical behavior, shock absorption can be considered as a possible application for these kinds of structures.

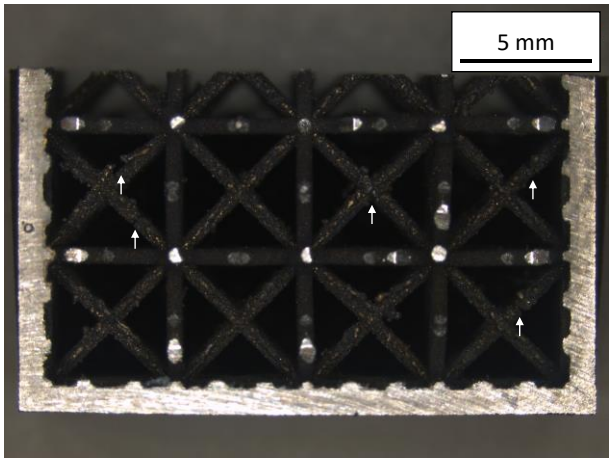

Fig. 6. Examples of strut after compression test connected to the shell and in the center part of the lattice samples.

4.1.4 Conclusions

The aim of this work was to analyze the behavior of 17-4 PH lattice samples surrounded by a solid shell, manufactured by L-PBF technology. In fact, lattices are often integrated in a solid structure in actual component and these complex structures require a proper characterization, considering in particular the critical feature represented by the lattice/shell interface. The lattice part with a cubic-based geometry was designed with FCC unit cell and a solid shell was built around the structure. Moreover, a solution treatment followed by ageing was performed. The microstructure was investigated, and compression tests were carried out to analyze the mechanical properties. It can be concluded that:

- As built and heat-treated samples exhibited different microstructure, hardness, and mechanical properties. As a consequence of the heat treatment, the results indicated that the HT samples exhibited higher stiffness and strength, better supporting the load, compared to the AB samples.
- The homogenization of the microstructure occurred due to the solution treatment, while the formation of strengthening Cu-rich precipitates was due to the aging treatment, as well as strength and hardness increase.
- Defects were detected at the interface between lattice and solid part, such as porosities. However, the shell did not detach from the internal lattice part during compression tests but followed the collapse of the internal lattice.

In this study the shell help to better support the load and follows the collapse of the internal lattice structure. Shock absorption can be considered as the possible applications of 17-4 PH lattice structure, but further studies are needed to better understand the failure mechanism under compression.

Appendix (not published)

In addition to investigating 17-4PH lattice structures with the solid shell, mechanical characterization was carried out for the lattices without the solid shell under As-Built (AB) and Heat-treated (HT) conditions. The heat treatment adopted was the same performed on the S samples (solution treatment followed by aging treatment) in order to compare both configurations under the same conditions. Compression tests were carried out on six samples, three for each AB and HT condition, and the results were reported in Figure 1a. The tests were considered completed when the samples started to collapse after reaching the ultimate strength value.

Fig. 1a shows the nominal engineering stress–strain curve. Initially, the stress rises to a peak, representing the maximum load-bearing capacity. The peak is followed by a drop as the displacement increases. In the initial phase of the graph, when the stress increases, the samples deformed uniformly without obvious fracture or collapse of lattice struts. However, after the peak, stress decreases due to the collapse of one lattice plane, indicated with the yellow dotted line (Fig. 1b). The struts of the cells within the collapsed plane deformed and broke, as highlighted by the red arrows shown in Fig. 1c. In contrast, the adjacent struts undergo significantly

less deformation. Contrary to the S samples, the NS lattices bore the load entirely and the bending component on the struts caused the main fracture.

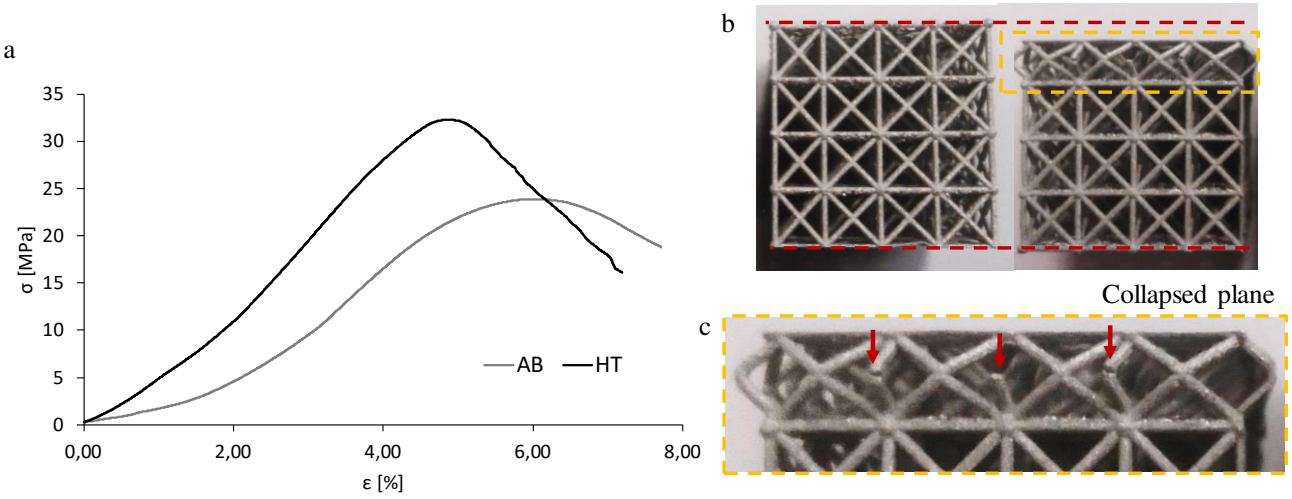

Figure. 1: (a) Stress-strain curve of AB and HT samples. (b) sample before and after the compression test, and (c) details of the collapsed plane.

During compression tests, for both the considered conditions, the stress initially increases with deformation up to a maximum value (24 ± 0.3 MPa and 32 ± 2 MPa for AB and HT samples, respectively). This maximum load represents the ultimate strength (σ_M). The peak of stress is related to strain values of 5.7 % and 4.9 % for AB and HT conditions, respectively. The Yield stress (σ_Y) follows the same trend and is 22 ± 1 MPa and 31 ± 2 MPa for the AB and HT samples, respectively.

The elastic modulus of the AB and HT samples is 5 ± 2 GPa and 9 ± 0.5 GPa, respectively. Probably, the micro strut surface quality, dimensional precision, microstructure complexity, and potential residual stresses are factors contributing to the low values of material properties [1].

The presence of the shell significantly improved the stiffness, strength, and load-bearing capacity of the structure as evident in Table 1. The samples with the solid shell (S) exhibited an elastic modulus seven times higher than the samples without the solid shell (NS) under the AB condition, and ten times higher under the HT condition. The same behavior is consistent in the stress results. In fact, the σ_M and σ_Y of the S samples resulted in seven/eight times higher than the NS samples under both AB and HT conditions.

To better illustrate the substantial differences between the S and NS samples, stress-strain graphs were plotted together and reported in Figure 2, where the effect of the solid shell is most clear. Notably, the S samples reached higher mechanical features.

a

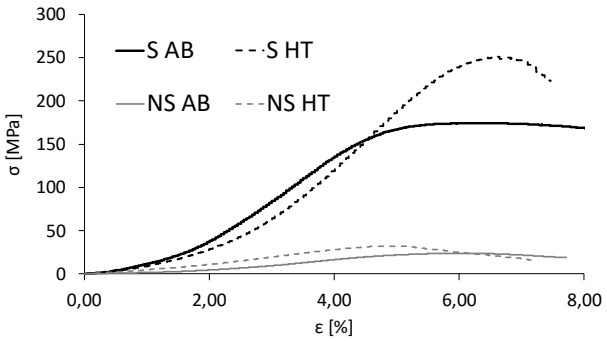

b

	No Shell (NS)		Shell (S)	
	AB	HT	AB	HT
E [GPa]	5.4 ± 1.8	8.7 ± 0.5	49.5 ± 0.0	64.2 ± 1.9
σ_y [MPa]	21.3 ± 0.9	31.4 ± 1.8	165.3 ± 4.0	237.7 ± 6.8
ε_y [%]	4.7 ± 0.6	4.7 ± 0.2	4.9 ± 0.1	6.2 ± 0.4
σ_M [MPa]	23.6 ± 0.3	31.9 ± 1.7	174.1 ± 0.4	247.9 ± 3.0
ε_M [%]	5.7 ± 1.1	4.9 ± 0.1	6.1 ± 0.6	6.9 ± 0.4

Figure. 2: (a) Stress-strain curve of S and NS samples. (b) Results of the compression tests of S and NS samples.

References

An, Sohee, Du Rim Eo, Il Sohn, and Kyunsuk Choi. 2023a. “Homogenization on Solution Treatment and Its Effects on the Precipitation-Hardening of Selective Laser Melted 17-4PH Stainless Steel.” Journal of Materials Science and Technology 166:47–57. doi: 10.1016/j.jmst.2023.04.055.

An, Sohee, Du Rim Eo, Il Sohn, and Kyunsuk Choi. 2023b. “Homogenization on Solution Treatment and Its Effects on the Precipitation-Hardening of Selective Laser Melted 17-4PH Stainless Steel.” Journal of Materials Science and Technology 166:47–57. doi: 10.1016/j.jmst.2023.04.055.

Bai, Long, Cheng Gong, Xiaohong Chen, Jia Zheng, Liming Xin, Yan Xiong, Xiaoying Wu, Mingjin Hu, Kun Li, and Yuanxi Sun. 2021. “Quasi-Static Compressive Responses and Fatigue Behaviour of Ti-6Al-4 V Graded Lattice Structures Fabricated by Laser Powder Bed Fusion.” Materials and Design 210:110110. doi: 10.1016/j.matdes.2021.110110.

Bayat, Mohamad, Aditi Thanki, Sankhya Mohanty, Ann Witvrouw, Shoufeng Yang, Jesper Thorborg, Niels Skat Tiedje, and Jesper Henri Hattel. 2019. “Keyhole-Induced Porosities in Laser-Based Powder Bed Fusion (L-PBF) of Ti6Al4V: High-Fidelity Modelling and Experimental Validation.” Additive Manufacturing 30(July):100835. doi: 10.1016/j.addma.2019.100835.

Bertocco, Alcide, Gianluca Iannitti, Antonio Caraviello, and Luca Esposito. 2022. “Lattice Structures in Stainless Steel 17-4PH Manufactured via Selective Laser Melting (SLM) Process: Dimensional Accuracy, Satellites Formation, Compressive Response and Printing Parameters Optimization.” International Journal of Advanced Manufacturing Technology 120(7–8):4935–49. doi: 10.1007/s00170-022-08946-2.

Bertol, Liciane Sabadin, Wilson Kindlein Júnior, Fabio Pinto da Silva, and Claus Aumund-Kopp. 2010. “Medical Design: Direct Metal Laser Sintering of Ti-6Al-4V.” Materials and Design 31(8):3982–88. doi: 10.1016/j.matdes.2010.02.050.

Cantaboni, Francesco, Paola S. Ginestra, Marialaura Tocci, Andrea Avanzini, Elisabetta Ceretti, and Annalisa Pola. 2022. “Compressive Behavior of Co-Cr-Mo Radially Graded Porous Structures under as-Built and Heat-Treated Conditions.” Frattura Ed Integrita Strutturale 16(62):490–504. doi: 10.3221/IGF-ESIS.62.33.

Dong, Guoying, Yunlong Tang, Dawei Li, and Yaoyao Fiona Zhao. 2020a. “Design and Optimization of Solid Lattice Hybrid Structures Fabricated by Additive Manufacturing.” Additive Manufacturing 33(February):101116. doi: 10.1016/j.addma.2020.101116.

Dong, Guoying, Yunlong Tang, Dawei Li, and Yaoyao Fiona Zhao. 2020b. “Design and Optimization of Solid Lattice Hybrid Structures Fabricated by Additive Manufacturing.” Additive Manufacturing 33(February):101116. doi: 10.1016/j.addma.2020.101116.

Fu, Jin, Junhao Ding, Shuo Qu, Lei Zhang, Michael Yu Wang, M. W. Fu, and Xu Song. 2022. “Improved Light-Weighting Potential of SS316L Triply Periodic Minimal Surface Shell Lattices by Micro Laser Powder Bed Fusion.” Materials and Design 222. doi: 10.1016/j.matdes.2022.111018.

Garcia-Cabezon, C., M. A. Castro-Sastre, A. I. Fernandez-Abia, M. L. Rodriguez-Mendez, and F. Martin-Pedrosa. 2022. “Microstructure–Hardness–Corrosion Performance of 17–4 Precipitation Hardening Stainless Steels Processed by Selective Laser Melting in Comparison with Commercial Alloy.” Metals and Materials International 28(11):2652–67. doi: 10.1007/s12540-021-01155-8.

Ginestra, P. S., L. Riva, G. Allegri, L. Giorleo, A. Attanasio, and E. Ceretti. 2020. “Analysis of 3D Printed 17-4 PH Stainless Steel Lattice Structures with Radially Oriented Cells.” Industry 4.0 – Shaping The Future of The Digital World 136–41. doi: 10.1201/9780367823085-25.

Jin, Nan, Zhenyu Yan, Yangwei Wang, Huanwu Cheng, and Hongmei Zhang. 2021. “Effects of Heat Treatment on Microstructure and Mechanical Properties of Selective Laser Melted Ti-6Al-4V Lattice Materials.” International Journal of Mechanical Sciences 190(July 2020):106042. doi: 10.1016/j.ijmecsci.2020.106042.

Kareem, Mohammed Qasim, Tamás Mikó, Gréta Gergely, and Zoltán Gácsi. 2023. “A Review on the Production of 17-4PH Parts Using Press and Sinter Technology.” Science Progress 106(1):1–31. doi: 10.1177/00368504221146060.

Kotzem, Daniel, Tizian Arold, Kevin Bleicher, Rajevan Raveendran, Thomas Niendorf, and Frank Walther. 2023. “Ti6Al4V Lattice Structures Manufactured by Electron Beam Powder Bed Fusion - Microstructural and Mechanical Characterization Based on Advanced in Situ Techniques.” Journal of Materials Research and Technology 22(January 2023):2111–30. doi: 10.1016/j.jmrt.2022.12.075.

Lashgari, H. R., C. Kong, E. Adabifiroozjaei, and S. Li. 2020. “Microstructure, Post Thermal Treatment Response, and Tribological Properties of 3D Printed 17-4 PH Stainless Steel.” Wear 456–457. doi: 10.1016/j.wear.2020.203367.

Leo, Paola, Marcello Cabibbo, Antonio Del Prete, Sara Giganto, Susana Martínez-Pellitero, and Joaquin Barreiro. 2021. “Laser Defocusing Effect on the Microstructure and Defects of 17-4ph Parts Additively Manufactured by Slm at a Low Energy Input.” Metals 11(4). doi: 10.3390/met11040588.

Mahmoudi, Mohamad, Alaa Elwany, Aref Yadollahi, Scott M. Thompson, Linkan Bian, and Nima Shamsaei. 2017. “Mechanical Properties and Microstructural Characterization of Selective Laser Melted 17-4 PH Stainless Steel.” Rapid Prototyping Journal 23(2):280–94. doi: 10.1108/RPJ-12-2015-0192.

Razavi, Seyed Mohammad Javad, Andrea Avanzini, Giovanna Cornacchia, Luca Giorleo, and Filippo Berto. 2021. “Effect of Heat Treatment on Fatigue Behavior of As-Built Notched Co-Cr-Mo Parts Produced by Selective Laser Melting.” International Journal of Fatigue 142(August 2020):105926. doi: 10.1016/j.ijfatigue.2020.105926.

Wu, Ziheng, Sneha Prabha Narra, and Anthony Rollett. n.d. “Exploring the Fabrication Limits of Thin-Wall Structures in a Laser Powder Bed Fusion Process.” doi: 10.1007/s00170-020-05827-4/Published.

Xiao, Zefeng, Yongqiang Yang, Ran Xiao, Yuchao Bai, Changhui Song, and Di Wang. 2018. “Evaluation of Topology-Optimized Lattice Structures Manufactured via Selective Laser Melting.” Materials and Design 143:27–37. doi: 10.1016/j.matdes.2018.01.023.

[1] R. A. W. Mines, S. Tsopanos, Y. Shen, R. Hasan, and S. T. McKown, “Drop weight impact behaviour of sandwich panels with metallic micro lattice cores,” *Int J Impact Eng*, vol. 60, pp. 120–132, 2013, doi: 10.1016/j.ijimpeng.2013.04.007.

Preliminary study on Laser Powder Bed Fusion process simulation and Residual stresses analysis with Deform 3D and X-ray diffraction

Introduction

Laser powder bed fusion (L-PBF) stands out as one of the most promising additive manufacturing technologies for metals. Residual stress is typical in Additive Manufacturing (AM) process mainly caused by high temperature gradient and rapid cooling [1]. These are critical since can lead to part distorsions, cracking….

For these reasons, the residual stress distribution is widely studied in literature using experimental and numerical simulation approaches. For instance, Mercelis et al. [2] explained the generation of residual stress by employing a model based on the temperature gradient mechanism (TGM) and a cool-down phase model. The TGM model delineates the development of residual stress during the additive manufacturing (AM) process, encompassing distinctive thermal cycles of melting, solidification, and remelting. Xu Song et al. [3] employed a finite element modeling methodology to simulate L-PBF processes. The objective of the researchers was to optimize AM process parameters through the finite element approach, aiming to mitigate the typically encountered issues of residual stresses and distortions in AM processes.

In this preliminary study, the discrete element method (DEM) was employed to closely replicate an L-PBF process. The main aim of this preliminary study was to forecast the distribution of residual stresses on a cube made of 17-4PH steel using the laser powder bed fusion process. To validate the simulation output, residual stresses were experimentally measured using X-Ray Diffraction (XRD) on 17-4 PH printed cubes with the same geometry of those used in the numerical simulation and a comparison of the simulated and experimental results was discussed. Simulations were conducted for 17-4PH stainless steel using the commercial software DEFORM®. The input parameters used to virtually reproduce the process are key process parameters such as scanning speed, laser power, and layer thickness actually used for sample production. Additionally, physical characteristics such as the nominal flow stress of the material and the chemical composition of the powder were considered.

Materials and methods

4.2.1.1 Samples production and XRD analysis

Twelve cubic samples with 10x10x10 mm dimensions were manufactured using 17-4 PH stainless steel powder produced by LaserForm®. The nominal chemical composition is reported in Table 1.

Table 1: Nominal chemical composition (wt%) of 17-4 PH powders used for the production of samples.

ELEMENT	Cr	Ni	Cu	Nb+Ta	C	Mn	P	S	Si	Fe
Wt. %	15.00 – 17.50	3.00 – 5.00	3.00 – 5.00	0.15 – 0.45	<0.07	<1.00	<0.04	<0.03	<0.01	Bal.

The ProX® DMP 100 printer (3D system®, Wilsonville, Oregon, USA) was used for manufacturing the cubic samples in a controlled nitrogen inert gas atmosphere (O2<0.01%). The manufacturing process parameters are reported in Table 2.

Table 2: Process parameters used for the production of samples.

Process Parameter	Value
Laser power [W]	100
Spot diameter [µm]	80
Scan speed [mm/s]	300
Hatch spacing [µm]	50
Layer thickness [µm]	30

Once manufactured, eight samples were detached from the printing plate by mechanical cutting. The residual stresses measurements were performed using a residual stress meter XRD Enixè® SN 2010-01. The samples detached from the building platform were etched to reduce the surface roughness without inducing alterations in the stress distribution associated with mechanical material removal. The measurements after chemical etching were performed at about 0.05 mm under skin.

The measures were conducted according to the standard UNI EN 15305 – 2008, with test conditions listed in Table 3.

Table 3: Test conditions used for the production of samples.

incident radiation	Cr Kα	*Oscillation Range*		±40°
Filter	Vanadium	*Number of angle Ψ used*		9
Diffractometer configuration	ω	*Angle selection Ψ*		Automatic
detector type	Strip	*Measure method*		Static
Detector angular window	40°	*Material*		17-4PH SS
Unit cell	Body-centered cubic	*Angle 2 θ expected*		156.32°
Miller indices of the plane used (hkl)	211	*Difractometric elastic constants*	*S1*	$-1.25\ 10^{-6}Mpa^{-1}$
Multi-regression	Si		*½ S2*	$5.76\ 10^{-6}Mpa^{-1}$
Background subtraction	Polynomial	*Supply voltage of the pipe*		30 kV
Position 2θ	Free	*Current of the pipe*		88 µA
Time of acquisition per angle Ψ	45s	*Diameter of the collimator*		1 mm

4.2.1.1 Finite Element Analysis

DEFORM® 3D software (Scientific Forming Technologies Corporation, Columbus, Ohio 43235) was used to simulate the 3D printing process and to calculate the residual stresses. It is important to assign the desired material properties during the design phase of the mathematical model.

The main mechanical properties adopted for the simulation of manufactured 17-4 PH samples, in accordance with the indicated standard, are reported in Table 4.

Table 4: Mechanical properties of 17-4 PH powders.

	Standard	**Value**
Ultimate strength [MPa]	ASTM E8M	1100 ± 90
Yield Strength Rp0.2% [MPa]	ASTM E8M	830 ± 110
Elongation at break [%]	ASTM E8M	19 ± 4
Hardness, Rockwell C	ASTM E18	32 ± 4
Impact roughness [J]	ASTM E23	71 ± 20

In addition, flow stress curves for 17-4PH stainless steel were used as proposed by the software (Figure 1). Flow stress curves represent the behavior of the flow stress as a function of the strain for different values of strain rate. This input data is necessary to estimate the residual stresses involved in the printing process.

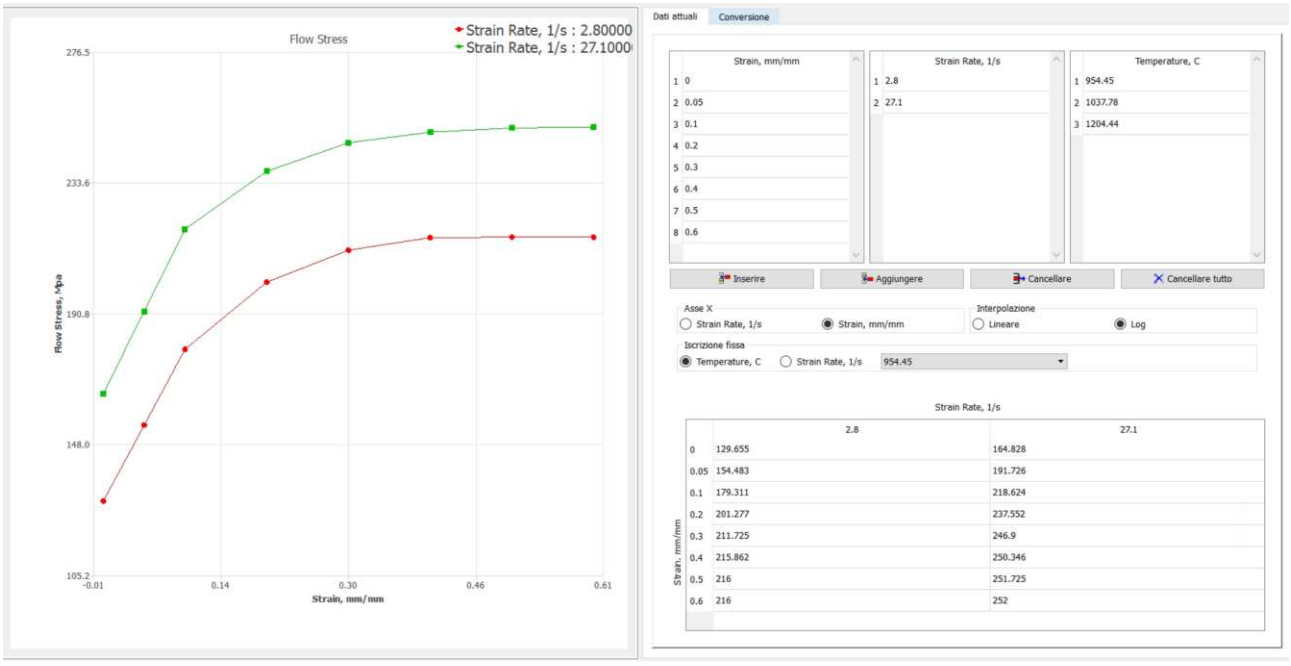

Figure 1. Flow stress of 17-4PH material proposed by Deform after the choice of material

Furthermore, the simulation was set by defining the properties of the objects to be printed (a) and the printing plate (b) as shown in Figure 2.

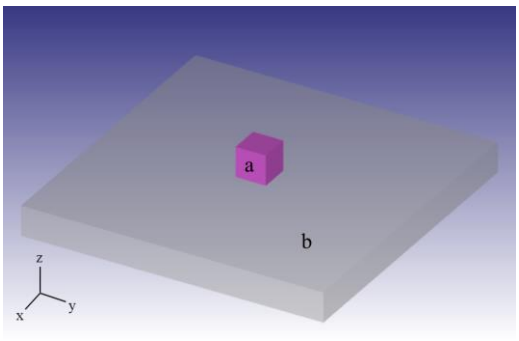

Object	**a**	**b**
*Materials**	17-4 PH	DIN C15
Temperature	20°C	50°C
Type of object	Elasto-plastic	Rigid
Process conditions	Thermal exchange with the environment	
Contact	Stick condition; Friction coefficient_cut = 1 Heat transfer condition = 0.5	

Figure 2. Designed objects and their features. *The materials were setting from DEFORM Library.

To simulate the L-PBF printing process, various parameters, including the number of layers, process parameters, supports, and simulation controls, must be defined. The assessment involved three distinct phases: production, cooling, and cutting.

In the production phase, the number of layers was set to ten using the Boolean - slice layers function, as illustrated in Figure 3. Subsequently, process parameters and supports were input into the appropriate text files, namely "DEF_ADDMPARM.DAT" for the process type and "ADDM_SUPPORT.DAT" for support stiffness, tailored to the cube's geometry. Key settings included activating layer-by-layer scanning, using the same scan speed (300 mm/s) and laser power (100 W) as in the experimental setup.

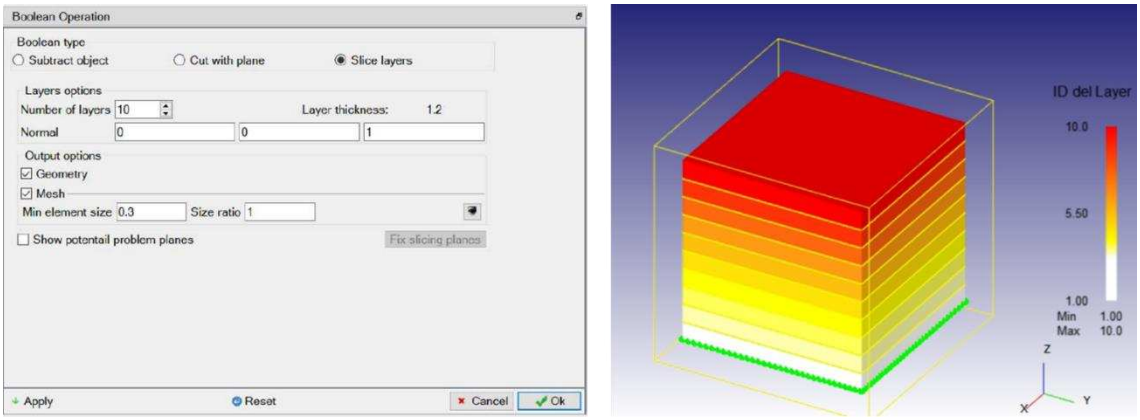

Figure 3. Number of layers set to 10 by the Boolean - slice layers function and graphical representation.

Finally, the simulation controls were defined and the same layer thickness of 50 µm was set as used for the sample production, as exhibited in Figure 4. This phase is the key step for the setting of the AM simulation according to powder bed technology.

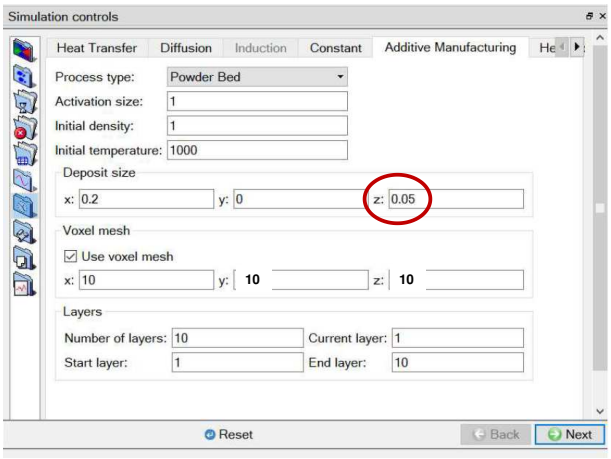

Figure 4. Simulation controls and layer thickness setting.

The model applied describes not only the melting phase but also includes the cooling and solidification steps. Therefore, the calculations stop when the temperature of the sample decreases to the initial condition (50 °C). Finally, the mechanical cutting was simulated to remove the sample from the printing plate. The shear force applied influenced the residual stresses distribution. Thus, it was necessary to calculate the final results on the sample before and after the mechanical cutting. Once all the phases were simulated and the residual stresses were calculated, the numerical results were compared with the experimental ones.

Results and discussions

4.2.1.2 Experimental results

The residual stress distribution of AB samples on the cubes removed from the printing plate was measured. Two measurements were made along the lateral side of the sample, on the edge and on the centerline of the cube (Pt.1, Pt.2) as illustrated in Fig. 5a. It is evident from Figure 5b that the two localized points exhibit very similar values. The results are deemed reliable, as the impact of the surface roughness on the cube has been mitigated.

a

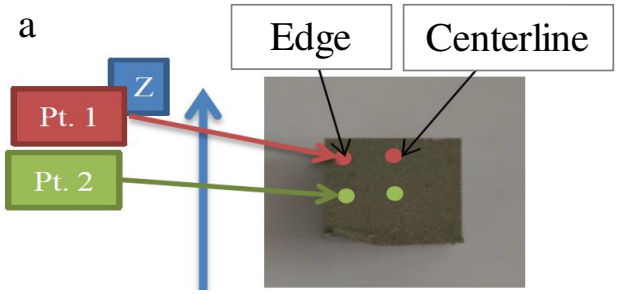

b

ZX plane	Z direction [MPa]	
	Edge	*Centerline*
Pt. 1	465	445
Pt. 2	489	502

Figure 5. (a) Measurements of AB samples removed from the printing plate at localized points along the lateral side on the edge and the centerline (Pt.1, Pt.2) of the cube. (b) Residual stresses measured on the samples removed from the printing plate by XRD analysis.

4.2.1.3 Numerical results

After conducting experimental measurements, it was decided to simulate and analyze the trend of residual stresses on the cubic samples attached to the printing plate. The residual stress distribution of the cube of finite

element model was calculated along the X (Fig. 6a), Y (Fig. 6b), and Z directions (Fig. 6c). Moreover, the maximum (σ_M) and minimum (σ_m) stress were identified and reported in Table 5.

Table 5. Maximum and minimum residual stresses calculated from FEM analyses on the cubic sample attached to the printing plate.

	X	Y	Z
σ_M [MPa]	379	362	595
σ_m [MPa]	-173	-173	-295

The trend of residual stresses, as presented in Fig. 6a and 6b, was nearly identical along the X and Y directions and both the maximum and minimum values were very similar. It emerges that at the bottom of the cube, where it is welded to the building platform, high tensile residual stresses are calculated, while the value of residual stress reduces moving upwards, where areas with compressive residual stresses can be identified (Fig. 6a-b).

Notably, the highest stress in the Z direction is recorded along the base of the cubic sample, as illustrated in Figure 6c. In fact, a peak of stress of 595 MPa was observed in Z direction on a surface between the printing plate and the cube. This elevated value can be attributed to the shrinkage of the printed metal welded onto the base plate. Furthermore, a lowest stress of -295 MPa was observed along the corner of the cube in the Z direction.

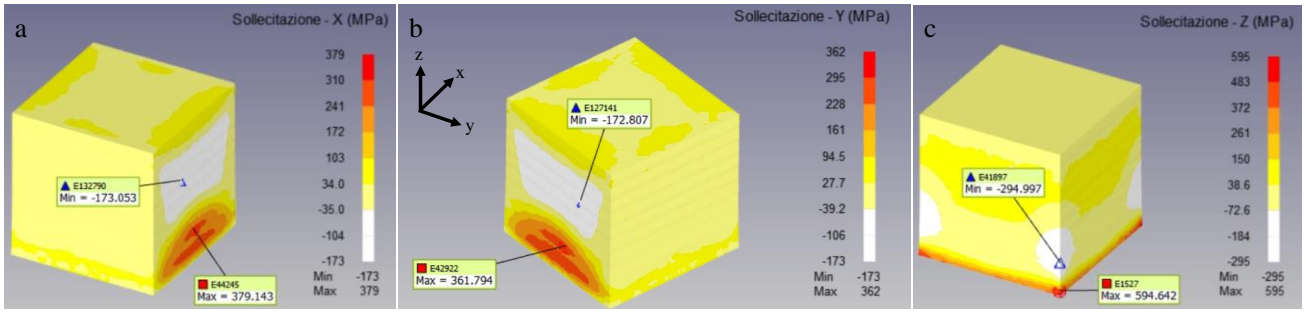

Figure 6. Residual stress distribution along the (a) X (b) Y and (c) Z directions

To compare experimental and simulated results, it was necessary to consider the residual stress distribution after the cube removal from the printing plate. Therefore, the mechanical cutting of the sample to remove it from the building platform was simulated and evaluation of residual stresses was repeated. In this case, the residual stress distribution was analyzed in Z direction, which is the one analyzed during the experimental measurements, as reported in Figure 7.

A different distribution of residual stress is evident after the removal of the sample from the platform comparing Fig. 6c and 7. In particular, at the base of the cube tensile stresses are no longer present, while compressive residual stresses are obtained.

In addition, slightly lower stresses (range 40-75 MPa) were revealed in the middle of the simulated specimen compared to those calculated for the samples adhered to the printing plate (range 40-150 MPa).

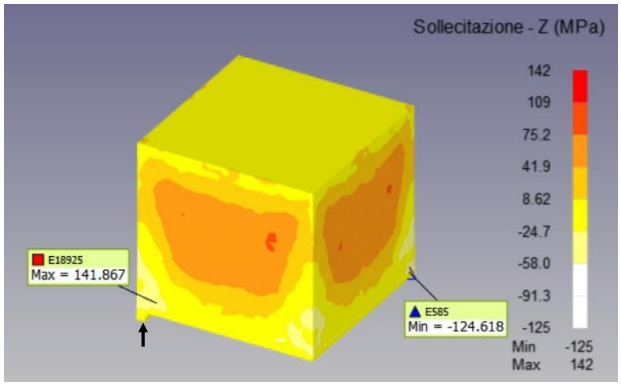

Figure 7. Residual stress distribution along the Z direction.

A comparison between experimental and numerical results were carried out as reported in Fig. 8a and 8b.

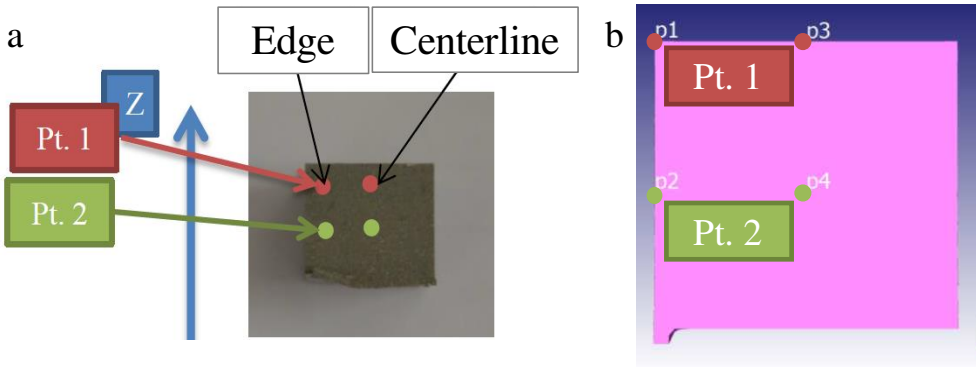

Figure 8. (a) Experimental measurements of AB samples removed from the printing plate at localized points along the lateral side on the edge and the centerline (Pt.1, Pt.2) of the cube. (b) Numerical measurement at localized points along the lateral side on the edge and the centerline (Pt.1, Pt.2) of the simulated sample.

The results are shown in Table 6. Both the experimental and the numerical results show the presence of compressive residual stresses, which are less detrimental than the tensile ones, indicating the good quality of the obtained specimens. However, the numerical model significantly underestimates the values of such residual stresses. This indicated the need to further detail the input parameters used in this preliminary study, especially introducing more information about the process parameters or other factors that may influence the process and the product, such as temperature, humidity, powder conditions, laser spot beam, etc.

Table 6. Maximum and minimum residual stresses calculated from FEM analyses on the cubic sample attached to the printing plate.

	ZX plane	Z direction [MPa]	
		Edge	*Centerline*
Experimental	Pt. 1	465	445
	Pt. 2	489	502
Numerical	Pt. 1	90 (p1)	43 (p3)
	Pt. 2	70 (p2)	102 (p4)

Conclusions

In this study, the L-PBF process was simulated using a commercial software (DEFORM®). The results from simulation in terms of residual stresses were compared with the experimental measurements obtained using XRD technology on 17-4PH steel cubic samples. A notable discrepancy existed between the experimental and numerical results. This variance was likely attributed to process conditions that were not included in the simulation. Therefore, additional simulation tests should be carried out, including simulations that incorporate flow stress data obtained from the mechanical characterization of own L-PBF printed samples.

Material Suite proves to be a valuable tool for converting experimental data (load-stroke curves or stress-strain curves) into tabular flow-stress data in DEFORM. The program can account for adiabatic correction in experimental data, providing fitted material parameters in the flow stress model and enabling graphic comparisons between original experimental data and model data. Finally, users can easily save the fitted flow stress data in a specific file for FEM simulation.

In conclusion, the input parameters used in this preliminary study should likely be increased and better detailed, especially introducing more information about the process parameters or other factors that may influence the process and the product, such as temperature, humidity, powder conditions, laser spot beam, etc.

Acknowledgements

The candidate deeply thanks for the support of DueEffe Engineering n conducting experimental XRD measurements, and acknowledges EcoTre Valente for their contribution to numerical simulations using the Deform 3D software.

References

[1] C. Li, Z. Y. Liu, X. Y. Fang, and Y. B. Guo, “Residual Stress in Metal Additive Manufacturing,” in *Procedia CIRP*, Elsevier B.V., 2018, pp. 348–353. doi: 10.1016/j.procir.2018.05.039.

[2] P. Mercelis and J. P. Kruth, “Residual stresses in selective laser sintering and selective laser melting,” *Rapid Prototyp J*, vol. 12, no. 5, pp. 254–265, 2006, doi: 10.1108/13552540610707013.

[3] X. Song *et al.*, “Advances in additive manufacturing process simulation: Residual stresses and distortion predictions in complex metallic components,” *Mater Des*, vol. 193, Aug. 2020, doi: 10.1016/j.matdes.2020.108779.

Conclusions

In this thesis, Laser Powder Bed Fusion (L-PBF) and Electron Beam Powder Bed Fusion (EB-PBF) technologies were used for the study and production of lattice samples with different cells geometries, building orientation in relation to the printing plate and different orientation of unit cell within the whole structure (radially graded and linear distribution). Lattice samples with an external solid shell were also designed and produced to understand the effects of the interface between lattice and solid parts on the final properties of the structure. Co-Cr-Mo, Ti-6Al-4V and 17-4 PH SS were used due to their mechanical properties and potential for biomedical and industrial applications.

The research activities carried out were organized in the present thesis into three main sections, depending on the type of material. Each section included contents on production, microstructural and mechanical characterization and FEM analysis.

The study on Co-Cr-Mo radially graded lattice structures, manufactured through L-PBF, showed that the building orientation in relation to the printing plate emerged as a relevant factor, impacting the mechanical responses. In fact, for the AB samples, the ultimate stress of 90° samples was higher than for the 0° ones. The results of this research demonstrated the feasibility of producing radially graded lattice structures and revealed how mechanical properties were influenced by cell geometry, and heat treatment. The radial distribution did not affect significantly the mechanical properties of the samples. However, the findings provide insights for tailoring lattice structures to specific applications, offering potential solutions for bone repair and tissue regeneration in biomedical contexts. The treated samples exhibited a more ductile behavior since a decrease in stiffness and hardness of the samples was recorded. This was consistent with the microstructural analysis and the study of fracture surfaces. In fact, as built samples showed the typical overlapped melt pools induced by L-PBF process, while the treated samples show a completely different microstructure. The melt pools disappeared and the presence of equiaxed grains highlighted by the presence of precipitates along the grain boundaries were shown. Finally, in the analysis of lattice structures characterized by a diamond radially oriented unit cell, manufactured using Co-Cr-Mo alloy and L-PBF, the mechanical properties were successfully compared to Finite Element Analysis (FEA), affirming the homogenization of stiffness along radial orientations.

In the context of Ti-6V-4Al lattice samples manufactured by L-PBF, the optimization of process parameters allowed to obtain the desired strut diameter with minimal porosity. Linear energy density was suggested as a practical indicator of the process, from which both the accuracy and internal morphology of lattice struts could be predicted and optimized. The process maps generated may be used in future lattice production as a practical method for structural control. This process stability was confirmed by measuring porosity, strut diameter, and analyzing the microstructure of a spinal cage. The study contributed to the understanding of the influence of process parameters on obtaining thin lattice structures.

In addition, Ti-6Al-4V lattice samples were manufactured through EB-PBF, with and without a solid shell (S and NS samples, respectively). It emerged that the shell provides a positive contribution needed to better support

the load in terms of maximum strength and energy absorption, especially for small deformations. On the other hand, more significant deformations of the structure lead to a concentration of stresses at the interface between the struts and the solid shell, resulting in the detachment of the shell itself. The FEM analysis for S samples also confirms that the connection between the struts and the solid shell is a critical point where high stresses are reached, leading to the detachment of the shell. The microstructure was homogeneous along the entire samples. In fact, no alteration of the microstructure was identified at the interface between lattice and shell for S samples because the process parameters used for both parts of the specimens were the same.

Finally, 17-4 PH lattice samples with and without a solid shell were manufactured by L-PBF. Furthermore, a solution treatment followed by aging was performed. The role of the shell and critical issues due to the connection with the lattice inner part were investigated. The defects were detected at the interface between lattice and solid part, such as porosities. The critical features were probably due to the local lack of melting and the abrupt change of geometry from thin struts to a bulk structure. However, the shell did not detach from the internal lattice part during compression tests but followed the collapse of the internal lattice. Moreover, to validate the results, the lattice samples without the solid shell were realized and analyzed. The presence of the solid part significantly improved the stiffness, strength, and load-bearing capacity of the structure.

Furthermore, as built (AB) and heat-treated (HT) samples exhibited different microstructure, hardness, and mechanical properties. As a consequence of the heat treatment, the results indicated that the HT samples exhibited higher stiffness and strength, better supporting the load, compared to the AB samples.

The homogenization of the microstructure occurred due to the solution treatment, while the formation of strengthening Cu-rich precipitates was due to the aging treatment, as well as strength and hardness increase.

Finally, the L-PBF process was simulated, comparing the residual stress distribution results obtained through numerical modeling, with experimental data measured using XRD technology on 17-4PH cubic samples. The main process parameters, such as laser power and scanning speed, have been used to simulate properly the process. The simulation does not take into account that the process may be influenced by the presence of humidity, non-sphericity of the powder, temperature, laser spot diameter, etc. In fact, a notable discrepancy between the experimental and numerical results was detected. This study is still ongoing and further research is needed. In particular, the flow stress data experimentally detected should be included in the simulations. The experimental results are needed for effective implementation in additive manufacturing applications.

To conclude, this thesis involved different metallic materials with different characteristics and applications. These topics are linked and contributed to valuable insights into the mechanical behavior, process optimization, and potential applications of lattice structures across diverse materials and manufacturing techniques.

The results obtained can help to better understand the behavior of these structures as a function of the applied load. Considering the results obtained from the compression tests, the studied structures could be used for biomedical applications and as space fillers or conformal parts for lightweight engineering, shock absorption, or

heat exchangers in aerospace. The key point is to find the best compromise between lightweight and reliability based on the application.